POLITECNICO DI TORINO

POLITECNICO DI TORINO

Master Degree course in Sustainable nuclear energy

Master Degree Thesis

Benchmarking ECCO calculations of LFR fuel assemblies by Monte Carlo calculations.

Supervisors
Prof. Sandra Dulla
Dr. Nicolo' Abrate
Dr. Daniele Tomatis
Dr. Matteo Falabino

Candidate
Salvatore Scarpati

Academic Year 2024-2025

Acknowledgements

Ringrazio con sincero affetto e stima tutte le persone che hanno collaborato con me per la realizzazione di questo lavoro.
In particolare tengo a ringrazio il dottore Nicolo' Abrate, la professoressa Sandra Dulla, il dottore Matteo Falabino, il dottore Vincenzo Giuseppe Peluso, e il dottore Daniele Tomatis non solo per le nozioni che mi hanno insegnato lungo questo percorso, ma anche per avermi trasmesso la passione e la professionalita' con cui svolgono la loro professione: spero un domani di poter riconoscere in me le stesse qualita'.
Ai miei genitori, fratelli, nonni e nipitini: grazie per tutto. Ogni altra parola sarebbe superflua.Ringrazio tutti gli amici che mi hanno regalato, durante questo lungo viaggio, leggerezza, sorrisi, ma anche il loro tempo nel momento del bisogno. Avervi al mio finaco e' un dono che spero di non aver mai sprecato.
E ringrazio Te, che mi accompagni ogni giorno.

Abstract

This thesis presents a preliminary analysis of the accuracy of ECCO deterministic calculations applied to LFR (Lead-cooled Fast Reactor) fuel assemblies, by comparing them with reference Monte Carlo simulations. The primary objective is to quantify and understand the discrepancies introduced by deterministic modeling when applied to fast reactor systems, particularly in view of ECCO's computational efficiency compared to Monte Carlo methods.

Verification was carried out using the OpenMC Monte Carlo code, which is widely accepted as a reliable and validated tool in the nuclear community. Experimental data were not available at this stage, so the comparison is limited to numerical benchmarks. The deterministic calculations were performed using the ECCO module from the ERANOS 2.3 code system.

The comparison focused on key neutronic parameters including the effective multiplication factor (k-eff), neutron flux distributions, reaction rates, and microscopic cross sections. The study modeled a representative LFR fuel assembly with hexagonal geometry, consistent with typical fast reactor core configurations.

This code-to-code comparison effort highlights the strengths and weaknesses of ECCO for fast reactor applications and sets the groundwork for further studies. The absence of experimental data limits the scope of the conclusions, but future work will include sensitivity analyses and, where possible, comparisons against critical benchmark experiments to enhance the reliability of the validation process.

Contents

Organization of the thesis

This thesis will show the first step needed for the validation of ECCO. In the first chapter it will introduce the general context and the concepts of verification and validation and what it will use in this thesis. Then the second and third chapter focus on the theory at the basis of the approximations that ECCO does. In the fourth chapter the codes will introduced, end wards the problem will be discussed. The results will be shown from the easiest model to most complex. In the end the conclusions will be drawn, as well as some future perspective.

Chapter 1

Introduction

1.1 General context

A nuclear reactor is a complex system where multiple physical phenomena interact. Among the engineering disciplines involved, reactor physics is central,since it determines the reaction rates that drive power generation. These rates result from neutron interactions with matter, which depend on both the material properties (like density, temperature, and composition) and the neutron population.

To describe these interactions, reactor physics uses a statistical mechanics framework rooted in Boltzmann' s transport theory. Since neutrons are neutral and present at relatively low densities, neutron-neutron interactions are negligible, simplifying the transport equation into a linear form.

Nuclear reactors operate through a self-sustained chain reaction, where neutrons from fission events cause further fissions. A reactor is said to be critical when this process maintains itself over time. Modeling this process requires solving the neutron transport equation, which becomes especially challenging due to the heterogeneous structure of the reactor and the variability in nuclear material properties.

With modern high-performance computing, it is now possible to perform detailed full-core 3D simulations. However, such simulations are computationally expensive and impractical for routine design work. Therefore, approximate models, validated against high-fidelity simulations, are often used. These models account for multi-physics phenomena such as delayed neutrons, thermal feedback, and material expansion, leading to non-linear and time-dependent behavior.

There are two main approaches to solving transport problems:

1. *Deterministic* Methods: These involve discretization the problem' s phase space and solving a simplified version of the transport equation. However, this can require an impractically fine energy discretization (due to resonant behavior of nuclides), so further approximations like resonance self-shielding models are introduced;

2. *Stochastic* (Monte Carlo) Methods: These simulate particle histories to estimate desired quantities with high fidelity and no geometric approximations. While highly

accurate and used as reference solutions, they are computationally intensive and not always feasible for full-core reactor simulations.

To manage this complexity, engineers use a calculation scheme,i.e. a sequence of steps with controlled approximations. While fast and practical, such schemes need expert judgment to stay within valid ranges and are often validated against detailed models and experimental data.

The standard deterministic method for core analysis uses a two-step approach:

Step 1: Perform detailed transport calculations on reactor substructures (e.g., fuel assemblies) to generate homogenized data libraries.

Step 2: Use these libraries in a coarse-mesh core calculation (often with a 3D diffusion model) to model the entire reactor efficiently.

While this method introduces approximations, it significantly reduces computation time. For this reason, deterministic codes can be highly valuable in the early stages of reactor design, where rapid estimates are needed to guide development.

This thesis was the report of my internship at *newcleo S.P.A.*, where I focused my attention on the deterministic code ECCO. The aim of this internship was to initiate the validation and verification (V&V) process of the ECCO code for calculations related to new reactor technologies, specifically Lead-cooled Fast Reactors (LFR). The main strength of ECCO lay in its ability to provide homogenized and condensed cross sections at both the pin and assembly levels, a feature that was essential for directly employing the processed data in full-core calculations, including within stochastic codes, thereby significantly reducing computational times. The ALFRED reactor was chosen as the reference case since it was based on the same technology as the reactor that was being designed by newcleo.

1.2 Verification&Validation

The definition of verification &validation(V&V) is not unique, one of them is: "*Verification is determining that a simulation computer program performs as intended*".

Validation is concerned with determining whether the conceptual simulation model is an accurate representation of the system under study" [1] . In other words, the verification focuses on the software, script and their errors while the validation is the study and comparison of the model with respect the real to reality, understanding how much the simulation is accurate, and for this reason V&V are important issues.

1.2.1 Preliminary evaluations

The subject of this work is ECCO and the focus is the evaluation of errors on the homogenized cross section produced of a Lead-cooled Fast Reactor. To do a validation, as said before, are needed data take at the end of experiments, since ALFRED is currently under design and not yet operational, direct experimental data on the reactor are not available. Therefore, it is necessary to rely on a different type of reference benchmark. In this work, a model of the LFR reactor will be developed using an already validated stochastic code, which will serve as the reference for the analyses.

This work is a preliminary analysis based on the evaluation of errors between these outputs and the corresponding values from the Monte Carlo code (OpenMC), which will be used as a reference, as no data from experiments will be used.his work is the first step and is a preliminary analysis between the deterministic code . The procedure of this work will be similar a V & V one, composed by three phases:

- choice of a reference problem;
- modeling in the software;
- evaluation of errors.

Chapter 2

Theory

2.1 Physical quantities

The population density $n(\vec{r}, \vec{\Omega}, E, t)$ is a function of time and a distribution of particles in the phase space. The properties of a medium are given in terms of probability per unit path (macroscopic cross sections), so it is possible know the total distance of particles done in one second in a element of phase space $drd\Omega dE$. The product of the population density and the module of their average velocity is angular flux:

$$\phi(\vec{r}, \vec{\Omega}, E, t) = v(\vec{r}, E)n(\vec{r}, \vec{\Omega}, E, t) \tag{2.1}$$

While the scalar flux is the number of reactions per unit time, unit volume and energy interval around point $\vec{r}$ and energy E, and it is the result of the contributions of all the particles coming from any direction, and is defined as:

$$\Phi(\vec{r}, E, t) = \oint d\Omega\phi(\vec{r}, \vec{\Omega}, E, t) \tag{2.2}$$

The particles inside the reactor interacts with each other and these events are base on the cross section, which defined the probability that a specific event occurs when two particles interact. The number of reactions of type x per unit surface and unit time is observed to be proportional to the number of incident particles per unit surface and unit time and the number of nuclides per unit surface:

$$drr_x = \sigma_x N n v_r ds \tag{2.3}$$

where drr_x is the surface reaction rate of type x,σ_x microscopic cross section of x reaction type, N is number of nuclides per unit volume, n particles per unit volume, v_r relative velocity and ds is small width od the target of beam.

The dimension of σ_x is an area and it is possible define it as bigger is and more possibility they will interact to have a reaction x.

Obliviously in a reactor the target is a mixture of isotopes and to describe the it is used the macroscopic cross section Σ_x define as:

$$\Sigma_x = \sum_i \Sigma_{x,i} = \sum_i \sigma_{x,i} N_i \tag{2.4}$$

where N_i is the number of the particles of the isotope i. The unit of macroscopic cross section is $\frac{1}{cm}$

If 2.3 is integrate per unite time, unite volume, and energy interval around $\vec{r}$, is defined as:

$$RR_x(t) = \int dE \oint d\Omega \Sigma_x(\vec{r}, E)\phi(\vec{r}, \vec{\Omega}, E, t) \tag{2.5}$$

The next definition will also be useful in this thesis for comparison on microscopic values, such as the microscopic reaction rate, which depends on isotope i and reaction type x integrates per unite time, unite volume, and energy interval around $\vec{r}$.

$$rr_{x,i}(t) = \int dE \oint d\Omega \sigma_{x,i}(\vec{r}, E)\phi(\vec{r}, \vec{\Omega}, E, t). \tag{2.6}$$

2.2 Neutron transport equation

The behavior of a nuclear reactor is governed by the distribution in space, energy, and time of the particles in the system, and one of the central problems of reactor theory is to predict this distribution and the transport equation describes how is the balance of particles in each point of the phase space (r, Ω, E) changes in time. In reactor physics, the main assumptions that are generally adopted are the following:

- Neutrons do not interact with each other, justified by the nearly absence of force fields and the much lesser density of the neutron gas with respect to that of the materials, making the probability per unit path to interact with other neutrons so small that the event is rare and can be neglected;
- The neutrons are modeled as points moving along straight lines called free paths,that are defined as the distance between two collision points and are much larger than the neutron size;
- The materials are isotropic in space;
- The nuclides are in thermal equilibrium with their neighbors.

To obtain the neutron transport equation, we generally adopt an Eulerian approach, so we observe an element drdΩdE of the phase space, centered in the position r, solid angle Ω and energy E, we call it A($\vec{r}$, $\vec{\Omega}$, E), and see how the number of particles changes in it during a time interval dt between the instants t and t+dt. This variation is expressed as:

$$[n(\vec{r}, \vec{\Omega}, E, t + dt)\hat{a}n(\vec{r}, \vec{\Omega}, E, t)]drd\Omega dE \tag{2.7}$$

Let's consider all the events for a particles to be emitted in A($\vec{r}$, $\vec{\Omega}$, E). It's possible define $S(\vec{r}, \vec{\Omega}, E)$ an external source density that provides the number of particles emitted in A($\vec{r}$, $\vec{\Omega}$, E) per unit volume, unit solid angle and unit energy element at time t. The total number of emitted particles is:

$$S(\vec{r}, \vec{\Omega}, E)drd\Omega dEdt \tag{2.8}$$

Now let's consider also the particles emitted through scattering events, for which any of them can traveling with all possible energy and directions. This contribution is the scattering source is given by the number of events:

$$\int_{4\pi} d\Omega' \int_0^\infty dE' \Sigma_s(\vec{r}, E' \to E, \vec{\Omega'} \cdot \vec{\Omega}) \phi(\vec{r}, E, \vec{\Omega}, t) dr d\Omega dE dt \tag{2.9}$$

with isotropic material assumption. Move on the fission source, the most interesting source, and its contributions is to A($\vec{r}, \vec{\Omega}$, E):

$$\sum_i \frac{\chi_i(\vec{r}, E)}{4\pi} \int_{4\pi} d\Omega' \int_0^\infty dE' \nu \Sigma_{f,i}(\vec{r}, E' \to E, \vec{\Omega'} \cdot \vec{\Omega}) \phi(\vec{r}, E, \vec{\Omega}, t) dr d\Omega dE dt \tag{2.10}$$

where $\nu_i(E)$ is the average number of neutrons produced by the fission of an isotope i and it depends on the incident particle energy, and $\chi_i(E)$ is the fission spectrum of isotope i, supposed independent of the energy of the incident particles and modeled iso-tropically resulting in a uniform probability of emission in angle equal to $\frac{1}{4\pi}$ and it is normalized to one.

Now let's focus on the losses, so the events for which the particles disappear from $A(\vec{r}, \vec{\Omega}, E)$, that are three: absorption, scattering with an other element and spatial leakage. The first two way can be sum up in one contribution and it represents the probability of a neutron undergoing any type of interaction (scattering or absorption) with a nucleus in the material.

$$\Sigma_t(\vec{r}, \vec{\Omega}, E) \phi(\vec{r}, E, \vec{\Omega}, t) dr d\Omega dE dt \tag{2.11}$$

Then the spatial leakage in $A(\vec{r}, \vec{\Omega}, E)$ is :

$$\vec{\Omega} \cdot \nabla \phi(\vec{r}, E, \vec{\Omega}, t) dr d\Omega dE dt \tag{2.12}$$

To preserve the balance of neutrons in $A(\vec{r}, \vec{\Omega}, E)$ at each instant t, the variation of the population in the interval dt must equal:

$$Population\ Variation = Sources - Leakages$$

Putting together all the previous contributions for the losses and the emissions in the last equation, dividing by $dr d\Omega dE dt$ both sides of the equation and taking the limit $t \to 0$, the neutron transport equation reads:

$$\begin{aligned} \frac{1}{v(\vec{r}, E)} \frac{\partial \phi(\vec{r}, \vec{\Omega}, E, t)}{\partial t} = & \int_{4\pi} d\Omega' \int_0^\infty dE' \Sigma_s(\vec{r}, E' \to E, \vec{\Omega'} \cdot \vec{\Omega}) \phi(\vec{r}, E, \vec{\Omega}, t) + \\ & \sum_i \frac{\chi_i(\vec{r}, E)}{4\pi} \int_{4\pi} d\Omega' \int_0^\infty dE' \nu_i \Sigma_{f,i}(\vec{r}, E' \to E, \vec{\Omega'} \cdot \vec{\Omega}) \phi(\vec{r}, E, \vec{\Omega}, t) + \\ & S(\vec{r}, \vec{\Omega}, E) - \vec{\Omega} \cdot \nabla \phi(\vec{r}, E, \vec{\Omega}, t) - \Sigma_t(\vec{r}, \vec{\Omega}, E) \phi(\vec{r}, E, \vec{\Omega}, t) \end{aligned} \tag{2.13}$$

where we have substituted $n(\vec{r}, \vec{\Omega}, E, t) = \frac{1}{v(\vec{r}, E}) \phi(\vec{r}, \vec{\Omega}, E, t)$.

In this work, the problems will be always in steady state so it is possible rewrite it as follow:

$$\vec{\Omega}\cdot\nabla\phi(\vec{r},E,\vec{\Omega})+\Sigma_t(\vec{r},\vec{\Omega},E)\phi(\vec{r},E,\vec{\Omega}) = \int_{4\pi} d\Omega' \int_0^\infty dE'\Sigma_s(\vec{r},E'\to E,\vec{\Omega'}\cdot\vec{\Omega})\phi(\vec{r},E,\vec{\Omega})+ \sum_i \frac{\chi_i(\vec{r},E)}{4\pi}\int_{4\pi} d\Omega' \int_0^\infty dE'\nu_i\Sigma_{f,i}(\vec{r},E'\to E,\vec{\Omega'}\cdot\vec{\Omega})\phi(\vec{r},E,\vec{\Omega}) + S(\vec{r},\vec{\Omega},E) \quad (2.14)$$

Equation 2.14 is the integro-differential form of the neutron transport equation, which is a first-order differential equation with respect to space. It requires one boundary condition such that:

$$\phi^-(\vec{r_b},E,\vec{\Omega}) = \phi^-_{in}(\vec{r_b},E,\vec{\Omega}) + \beta(E,\vec{\Omega'}\to\vec{\Omega})\phi^+(\vec{r'_b},E,\vec{\Omega'}) \quad (2.15)$$

where $\vec{r_b}$ stand for boundaries od spatial domain, ϕ^-_{in} is the incoming angular flux, β is the albedo parameter that accounts for any albedo boundary condition. For vacuum boundary condition, the parameter β equals zero, and ϕ^-_{in} can be considered as an external source or null.

2.3 Treatment of the Scattering Source

In reactor physics, the materials treated is typically isotropic for neutrons, so the cross sections are independent of the incident direction of a particle and it depends only on the angle of deviation.

$$\Sigma_s(E\to E',\vec{\Omega}\to\vec{\Omega'}) = \frac{1}{2\pi}\Sigma_s(E\to E',\vec{\Omega}\cdot\vec{\Omega'}) \quad (2.16)$$

Where the 2π is for the take in account the isotopically. Now, the scattering cross section is generally expanded on the Legendre polynomials P_l up to the the order of scattering of the system, that depends on μ_o and is equal of $\vec{\Omega}\to\vec{\Omega'}$.

$$\Sigma_s(E\to E',\mu_o) = \sum_{l=0}^{L}\frac{2l+1}{2}\Sigma_{sl}(E\to E')P_l(\mu_o) \quad (2.17)$$

with

$$\Sigma_{sl}(E\to E') = \int_{-1}^{1} d\mu_o\Sigma_s(E\to E',\mu_o)P_l(\mu_o) \quad (2.18)$$

Let's rewrite the scattering source, 2.9, with the Legendre polynomials expansion:

$$\int_0^\infty dE'\sum_{l=0}^{L}\frac{2l+1}{4\pi}\Sigma_{sl}(E\to E')\int_{4\pi} d\Omega' P_l(\Omega\cdot\Omega')\phi(\vec{r},E',\vec{\Omega'}) \quad (2.19)$$

To compute the integral over $d\Omega'$, is useful take advantage of spherical harmonics, ad the following:

$$P_l(\Omega\cdot\Omega') = \sum_{m=-l}^{l} A_{l,m}(\Omega)A_{l,m}(\Omega') \quad (2.20)$$

where $A_{l,m}(\Omega)$ is a spherical harmonic, [6]. After some steps, It is possible represent the angular flux over with the spherical harmonics approximated to L-order:

$$\phi(\vec{r}, E, \vec{\Omega}) = \sum_{l=0}^{L} \frac{2l+1}{4\pi} \sum_{m=-l}^{l} \phi_{l,m}(\vec{r}, E) A_{l,m}(\Omega) \tag{2.21}$$

where the $\phi_{l,m}(\vec{r}, E)$ are the angular moments of neutron flux,which is defined as:

$$\phi_{l,m}(\vec{r}, E) = \oint_{4\pi} d\Omega' \phi(\vec{r}, E, \vec{\Omega'}) A_{l,m}(\Omega') \tag{2.22}$$

And finally the Scattering source become:

$$\int_0^{\infty} dE' \sum_{l=0}^{L} \frac{2l+1}{4\pi} \Sigma_{sl}(E \to E') \sum_{m=-l}^{l} \phi_{l,m}(\vec{r}, E') A_{l,m}(\Omega) \tag{2.23}$$

2.4 Leakage model

This model is introduced in the deterministic codes, because can simulate the leakage of the system though the evaluation of a geometrical parameter called Buckling B, so thank to its it's possible enforce a study of a infinity lattice, which is generally super critical, to a critical situation, value of $k_{inf} = 1$. In the following part we will explore better the homogenization, but the base of it is this method because to do it is useful an angular flux of a critical assembly or pin.

The neutron flux is written as the product of a macroscopic distribution in space ψ and a periodic fundamental mode φ :

$$\phi(\vec{r}, E, \vec{\Omega}) = \varphi(\vec{r}, E, \vec{\Omega}) \psi(\vec{r}) \longmapsto \phi(\vec{r}, E, \vec{\Omega}) = \varphi(\vec{r}, E, \vec{\Omega}) e^{i\vec{B}\cdot\vec{r}} \tag{2.24}$$

This factorization is exact if we are under the asymptotic situation, which can be represented by the Laplace problem:

$$\nabla^2 \psi(\vec{r}) + B^2 \psi(\vec{r}) = 0 \tag{2.25}$$

where ψ is a property of the reactor and the solution of the Laplace equation, and B is the Buclking, a geometrical parameter. Let's substitute in the transport equation:

$$\begin{aligned} i\vec{B} \cdot \vec{\Omega} + \Sigma_t(\vec{r}, E)]\varphi(\vec{r}, E, \vec{\Omega}) = & \int \oint_{4\pi} \Sigma_s(\vec{r}, E' \to E, \vec{\Omega'} \to \vec{\Omega}) \varphi(\vec{r}, E', \vec{\Omega'}) d\vec{\Omega'} dE' \\ & + \frac{1}{k} \int \oint_{4\pi} \nu\Sigma_f(\vec{r}, E') \varphi(\vec{r}, E', \vec{\Omega'}) \frac{\chi(\vec{r}, E)}{4\pi} d\vec{\Omega'} dE' \end{aligned} \tag{2.26}$$

Where the first term of equation $i\vec{B} \cdot \vec{\Omega}$ acts as a fictitious absorption term, depending on the geometrical buckling B.

Chapter 3

Numerical Methods

3.1 Deterministic approximation

This chapter will discuss of numerical method introduces by deterministic codes to solve the transport equation, for examples the multigroups approximation and inconsistent method, to simplify the equation and the level of computation cost.

3.2 Multi-group Approximation

The first approximation that i would introduce is on the energy domain, and it is the **Multigroups formalism**. The idea is of moving from a continuous domain to a discrete one. To do this it's necessary integrate the equation on a interval of energy $[E, E + \Delta E]$ called **group**. Moreover we have a maximum energy and minimum one and we divide into finite groups N, inside which the neutrons are considered uniformly distributed. The **multigroup cross sections** are then to be precomputed per each energy group as follows:

$$\Sigma_{x,i}^{g}(\vec{r}) = \frac{\int_{\Delta E} dE\, \Sigma_{x,i}(\vec{r}, E) w(\vec{r}, E)}{\int_{\Delta E} dE\, w(\vec{r}, E)} \tag{3.1}$$

where ΔE is the energy interval associated to group g, x and i are respectively the reaction type and the isotope, and w is a weighting function. The number of the groups can change because there are some isotopes, called resonant isotopes, that have a particular behavior in the epithermal region, energies between 0.4 eV and 10 eV. The w is generally substitute with the spectrum of emission in order to preserve the the reaction rates in each group, although a rigid process would like angular flux.

The multigroup cross sections is not the unique quantity to be integrated, but also the multigroup angular flux, and scalar flux:

$$\phi^{g}(\vec{r}) = \oint dE \phi(\vec{r}, \vec{\Omega}, E) \tag{3.2}$$

$$\Phi^{g}(\vec{r}, E) = \oint d\Omega \phi^{g}(\vec{r}, \vec{\Omega}) \tag{3.3}$$

$$\varphi^g(\vec{r}) = \oint dE\varphi(\vec{r},\vec{\Omega},E) \tag{3.4}$$

To obtain the multigroup transport equation is necessary integrate each operator of 2.26. Let's start from the **loss operator**:

$$\int_{\Delta E} dE[i\vec{B}\cdot\vec{\Omega}+\Sigma_t(\vec{r},E)]\varphi(\vec{r},E,\vec{\Omega}) = [i\vec{B}\cdot\vec{\Omega}+\Sigma_t^g(\vec{r})]\varphi^g(\vec{r},\vec{\Omega}) \tag{3.5}$$

The **fission source**:

$$\sum_i \int_{\Delta E} dE\frac{\chi_i(\vec{r},E)}{4\pi}\oint_{4\pi} d\Omega'\int_0^\infty dE'\nu_i\Sigma_{f,i}(\vec{r},E')\varphi(\vec{r},E',\vec{\Omega'}) =$$
$$= \frac{\chi_i^g(\vec{r})}{4\pi}\sum_{g'}^{N}\oint_{4\pi} d\Omega'\nu_i\Sigma_{f,i}^{g'}(\vec{r})\varphi^{g'}(\vec{r},\vec{\Omega'}) \tag{3.6}$$

In the end the **scattering source**:

$$\int_{\Delta E} dE\int_0^\infty dE'\oint_{4\pi}\Sigma_s(\vec{r},E'\to E,\vec{\Omega'}\to\vec{\Omega})\varphi(\vec{r},E',\vec{\Omega'})d\vec{\Omega'} =$$
$$= \sum_{l=0}^{L}\frac{2l+1}{4\pi}\sum_{m=-l}^{l}A_{l,m}(\Omega)\int_{\Delta E}dE\int_0^\infty dE'\Sigma_{sl}(E\to E')\varphi_{l,m}(\vec{r},E')$$
$$= \sum_{g'}^{N}\sum_{l=0}^{L}\frac{2l+1}{4\pi}\Sigma_{sl}^{g'\to g}(\vec{r})\sum_{m=-l}^{l}A_{l,m}(\Omega)\varphi_{l,m}^{g'}(\vec{r}) \tag{3.7}$$

It can be seen that $\Sigma_{sl}^{g'\to g}$ is a square matrix, which ca be divide into three sub-matrices : in a diagonal self -scattering matrix, a lower triangular down-scattering matrix and an upper triangular up-scattering matrix.

Thanks to this rearranging, the transport equation turns into a system of N mono-kinetic equations coupled by the fission and scattering source, with the following form:

$$[i\vec{B}\cdot\vec{\Omega}+\Sigma_t^g(\vec{r})]\varphi^g(\vec{r},\vec{\Omega}) = \sum_{g'}^{N}\sum_{l=0}^{L}\frac{2l+1}{4\pi}\Sigma_{sl}^{g'\to g}(\vec{r})\sum_{m=-l}^{l}A_{l,m}(\Omega)\varphi_{l,m}^{g'}(\vec{r})+$$
$$+\sum_i\frac{\chi_i^g(\vec{r})}{4\pi}\sum_{g'}^{N}\oint_{4\pi}d\Omega'\nu_i\Sigma_{f,i}^{g'}(\vec{r})\varphi^{g'}(\vec{r},\vec{\Omega'}),\quad \forall g\in[1,...,N] \tag{3.8}$$

In order to solve the system of N equations, an iterative method is used to reduced the number of unknowns. It is composed by three loops [6]:

1. Outers: consists in a Power iterations , where the fission source and eigenvalue are fixed and updated at the end of each step using the new neutron flux. This loop is used to resolved the equations also for fast groups;

2. Thermals: some terms of scattering source are unknowns because they have the up-scattering, which depends on the high energy groups. So this loop focuses on the up scattering source, which is update at the end of each iteration;

3. Inners: here the convergence is on the self-scattering source, which is update at the end of each iteration.

3.3 The Spherical Harmonics Method

I have obtained a system of integro-differential equations, and generally the deterministic codes use spherical harmonics as basis functions to project the system and to obtain the Pn or the Bn method, because I have already the expansion of scattering source on them 2.3. To simplify the notation, is useful define the emission density ,$Q^g(\vec{r},\vec{\Omega})$ depends on the neutron flux, therefore, it is also expanded on spherical harmonics:

$$Q^g(\vec{r},\vec{\Omega}) = \sum_{l=0}^{L} \frac{2l+1}{4\pi} \sum_{m=-l}^{l} A_{l,m}(\Omega) Q_{l,m}^{g'}(\vec{r}) \tag{3.9}$$

with

$$Q_{l,m}^{g'}(\vec{r}) = \sum_{g'}^{N} \Sigma_{sl}^{g'\to g}(\vec{r}) \varphi_{l,m}^{g'}(\vec{r}) + \frac{1}{k} \sum_{i} \frac{\chi_i^g(\vec{r})}{4\pi} \sum_{g'}^{N} \nu_i \Sigma_{f,t}^{g'}(\vec{r}) \varphi_{l,m}^{g'}(\vec{r}) \delta_{l0} \tag{3.10}$$

to rewrite the system as following :

$$[i\vec{B}\cdot\vec{\Omega} + \Sigma_t^g(\vec{r})]\varphi^g(\vec{r},\vec{\Omega}) = Q^g(\vec{r},\vec{\Omega}) \tag{3.11}$$

There are a lot definition of spherical harmonics, but the following is the one which the function after the projection will be real [6]:

$$A_{0,0} = 1 \quad A_{1,-1} = \Omega_z \quad A_{1,0} = \Omega_x \quad A_{1,1} = \Omega_y \tag{3.12}$$

where $l = 0{,}1$ *and* $m = -1{,}0{,}1$. The angular distribution of the neutron flux over the unit sphere can be expressed through a spherical harmonics expansion truncated at order L. In this formulation, the coefficients $\varphi^{\ell,m}$ represent the angular moments of the flux.

In particular, for $\ell = 0$ and $\ell = 1$, the corresponding angular moments are associated with the scalar flux and the neutron current, respectively, as follows:

$$\varphi(\vec{r}) = \varphi_{0,0} \quad \mathbf{J}(\vec{r}) = \varphi_{1,0}\cdot\hat{i} + \varphi_{1,1}\cdot\hat{j} + \varphi_{1,-1}\cdot\hat{k} \tag{3.13}$$

.

3.3.1 *Pn*

The PN equations are given by expanding

$$[i\vec{B}\cdot\vec{\Omega} + \Sigma_t^g(\vec{r})]\varphi_{l,m}^g(\vec{r},\vec{\Omega}) = Q_{l,m}^{g'}(\vec{r}) \tag{3.14}$$

and projecting Equation 3.11 on spherical harmonic $A_{l',m'}(\Omega)$

$$\int_{4\pi} d\vec{\Omega} A_{l',m'}(\vec{\Omega}) \left[i\vec{B}\cdot\vec{\Omega} + \Sigma_t^g \right] \sum_{\ell=0}^{N} \sum_{m=-\ell}^{\ell} \varphi_{\ell,m}^g A_{l,m}(\vec{\Omega}) = \int_{4\pi} d\vec{\Omega} A_{l',m'}(\vec{\Omega}) Q_{\ell,m}^g \tag{3.15}$$

After that, there is the integration over the domain of $\vec{\Omega}$ we obtain a system of $L+1$ equation for each groups. The order of scattering used in this study is $L = 1$, as said before, and the P1 equation are:

$$\begin{cases} iB\varphi_1^g + \Sigma_t^g \varphi_0^g = \sum_{g'} \Sigma_{s,0}^{g'\to g} \varphi_0^{g'} + \frac{1}{k} \sum_{g'} \nu\Sigma_f^{g'} \varphi_0^{g'} \frac{\chi^g(\vec{r})}{4\pi} \\ \frac{iB}{3}\varphi_0^g + \Sigma_t^g \varphi_1^g = \sum_{g'} \Sigma_{s,1}^{g'\to g} \varphi_1^{g'} + \frac{1}{k} \sum_{g'} \nu\Sigma_f^{g'} \varphi_1^{g'} \frac{\chi^g(\vec{r})}{4\pi} \end{cases} \tag{3.16}$$

where φ_0^g is the angular flux , and φ_1^g is the current.

3.3.2 *Bn*

As the Pn, the process to derive the Bn equation has the same steps more one. Indeed before the projection the transport equation it is necessary divide by $[\Sigma_t^g - i\vec{B}\cdot\vec{\Omega}]$, then is the same, and for our study the equations of B1 are [8]:

$$\begin{cases} iB\varphi_1^g + \Sigma_t^g \varphi_0^g = \sum_{g'} \Sigma_{s,0}^{g'\to g} \varphi_0^{g'} + \frac{1}{k} \sum_{g'} \nu\Sigma_f^{g'} \varphi_0^{g'} \frac{\chi^g(\vec{r})}{4\pi} \\ \frac{iB}{3}\varphi_0^g + \frac{b_0}{\Sigma_{t,1}} \Sigma_t^g \varphi_1^g = \sum_{g'} \Sigma_{s,1}^{g'\to g} \varphi_1^{g'} + \frac{1}{k} \sum_{g'} \nu\Sigma_f^{g'} \varphi_1^{g'} \frac{\chi^g(\vec{r})}{4\pi} \end{cases} \tag{3.17}$$

where b_0 is a constant [11].

3.4 Homogeneous and Heterogeneous

The treatment of homogeneous or heterogeneous geometries in ECCO are based on two formulation. For the first one it uses **Fundamental mode**, other than the equations derived in the previous paragraphs and applied to all geometry. If the model is **heterogeneous**, it is necessary use the **Collision Probability** (CP) method. The Collision Probability (CP) Method originates from the projection of the integral form of the neutron transport equation onto spherical harmonics, resulting in a system of equations expressed in terms of the angular flux moments $\varphi_{\ell,m}$.

Due to the strong spatial coupling introduced by this formulation which often leads to computationally expensive solutions historical implementations have relied on approximations of the scattering source. A common approach is to truncate the source expansion up to a certain anisotropy order, typically $L = 1$.

To numerically solve the resulting equations in multidimensional geometries, the domain is partitioned into N_r homogeneous regions. For simplicity, the scalar flux and cross sections are assumed constant within each region. As a result, the volume integral over the entire domain becomes a sum over the regions j (each with volume V_j).

Integrating over the volume of region i, the resulting balance equation takes the form:

$$V_i \varphi_i = \sum_{j=1}^{N_r} Q_j^0 V_j P_{ij} \tag{3.18}$$

where:

φ_i is the scalar flux in region i, Q_j^0 is the isotropic source in region j, V_j is the volume of region j, P_{ij} is the collision probability coefficients defined below.

The coefficients P_{ij} is given by:

$$P_{ij} = \frac{1}{V_j} \int_{V_i} d^3r \int_{V_j} d^3r' \frac{e^{-\tau(\vec{r}',\vec{r})}}{|\vec{r} - \vec{r}'|^2} \tag{3.19}$$

The matrix P_{ij} is symmetric, and each P_{ij} represents the probability that a neutron emitted isotropically and uniformly in region j reaches region i without undergoing a collision. The product $\Sigma_i P_{ij}$, where Σ_i is the total macroscopic cross section in region i, is called the first-flight collision probability which gives the method its name.

Due to the full spatial coupling, the CP method is most suited to small systems where the number of regions N_r remains manageable. Another limitation is the approximation of the isotropic angular source, as including higher-order angular moments would require similarly dense coupling matrices. Nevertheless, the method has key advantages:

- It eliminates the angular variable without approximating the angular flux representation;
- It allows grouping of regions with similar properties, assuming they experience comparable neutron fluxes thus reducing computational burden.

This formulation is particularly suited to heterogeneous geometries, such as fuel pins or assemblies, where a fine spatial subdivision of the domain is required.

3.5 Consistent and Inconsistent

This approximation is a peculiarity of ECCO because the equations 3.17 and 3.16 are already in the consistent formulation. To achieve faster computation, it is possible to introduce another approximation on the first-order scattering moment,the **extended transport approximation**, and it consisting of assuming:

$$\sum_{g'} \Sigma_{s,1}^{g' \to g} \varphi_1^{g'} = \Sigma_{s,1}^{g} \varphi_1^{g'} \tag{3.20}$$

With this addition, the method becomes **inconsistent**.

3.6 Resonance Effects and Self-Shielding Treatment Using Probability Tables

In reactor physics, certain isotopes such as ^{238}U and ^{240}Pu exhibit prominent resonance behavior due to quantum-level nuclear effects. These resonances appear as sharp peaks

in the microscopic cross section $\sigma(E)$, especially in the epithermal energy region. When neutrons slow down and pass through these resonance energies, their probability of interaction increases significantly, leading to localized flux depressions known as *self-shielding*.

Self-shielding occurs because strong absorbers reduce the neutron flux precisely where their absorption cross section is highest. As a result, the effective (i.e., flux-weighted) cross section becomes smaller than its unshielded value. This phenomenon must be accurately treated to predict reaction rates and neutron economy, especially in heterogeneous reactor cores.

Traditional deterministic transport methods average cross sections over energy groups, which can smooth out sharp resonance features. To address this limitation, the `ECCO` code uses *probability tables* a statistical method that allows for accurate modeling of cross-section fluctuations and self-shielding within each energy group.

Within ECCO, the total microscopic cross section $\sigma(u)$ is statistically represented over a lethargy group $[u_{g-1}, u_g]$ using a discrete probability distribution. Each probability table is composed of K sublevels, each defined by:

- a total cross section value σ_k,
- an associated probability weight ω_k (with $\sum_k \omega_k = 1$),
- corresponding partial cross sections $\sigma_{x,k}$ for reaction types x (e.g., capture, fission, scattering).

This approach allows ECCO to compute self-shielded cross sections and neutron fluxes using a consistent transport framework, preserving detailed resonance behavior.

While the self-shielding treatment in ECCO is based on the *subgroup method*, where a separate transport calculation is performed for each cross-section level in the probability table. The main steps are:

1. Flux Calculation for Each Probability Level: For each subgroup k, the neutron flux φ_g^i is determined by solving the collision probability transport equation:

$$\varphi_g^i = S_g^i + \sum_j P_{ij}^{gg} \varphi_g^j, \tag{3.21}$$

where P_{ij}^{gg} are the collision probabilities calculated using the total cross section σ_k for the corresponding level.

2. Self-Shielded Cross Section Evaluation: Once the fluxes are known, the self-shielded cross section for a reaction type x is computed as:

$$\sigma_{x,g}^i = \frac{\sum_{k\in\alpha_j} p^k S_{g,k}^j \sigma_{x,g}^k}{\sum_{k\in\alpha_j} p^k S_{g,k}^j}, \tag{3.22}$$

where p^k are the probabilities from the table and $S_{g,k}^j$ are the source terms at level k.

The narrow resonance approximation (NRA), used in this method, becomes valid in fine lethargy meshes, where:

- the energy loss by elastic scattering is much greater than the group width,
- the within-group neutron source is nearly constant due to external origin of incoming neutrons.

The use of a fine group structure is essential not only to validate the NRA, but also to:

- explicitly resolve wide and overlapping resonances from different isotopes,
- build group-to-group transfer matrices that are independent of the weighting spectrum,
- ensure accurate flux profiles across energy groups, particularly for slowing-down calculations.

Chapter 4

Codes

4.1 Deterministi code: The ECCO Cell Code and the ERANOS Suite

The study of nuclear reactors requires simulating physical phenomena at small scales, even when the geometric domain spans several meters. This need arises from the competing scales imposed by the neutron mean free paths in the various materials of a highly heterogeneous domain, alongside the macroscopic distribution of the neutron flux. To reduce the computational cost of such simulations, calculations are typically divided into two sequential phases: cell (or lattice) calculations followed by reactor calculations.

The main purpose of a cell calculation is to generate, from a general-purpose nuclear data library (such as JEFF or ENDF/B), a derived dataset tailored to the specific problem being studied. The cell code is generally applied to a limited domain, like a single assembly or pin, where microscopic and macroscopic cross sections are computed through energy condensation and volume homogenization.

In the subsequent reactor calculation, the data obtained from the cell calculations are assigned to the various core regions, each assumed to be homogeneous. The reactor code is then used to solve the quasi-static transport equation and to compute the required quantities, including integral parameters, sensitivity coefficients, and uncertainties. Additionally, the reactor code can be used for other analyses, such as depletion calculations.

In this thesis, ECCO was employed as the cell code. ECCO is part of the ERANOS suite, which is a reference tool for the core design of fast-spectrum nuclear reactors. Within ERANOS, the BIdimensionnel Sn TRansport OptimisÃ¨ (**BISTRO**) code is used for reactor calculations, enabling the solution of the transport (or diffusion) equation in one-dimensional or two-dimensional core geometries. BISTRO uses the discrete ordinates method for angular discretization and the finite difference method for spatial discretization of the neutron flux. While **BISTRO** provides the neutron flux distributions within the reactor core, the **VARIANT** module extends these calculations by performing sensitivity and uncertainty analyses relevant to fast reactor systems. It executes perturbation calculations on nuclear data and system parameters, enabling the evaluation of the impact of uncertainties on key reactor performance indicators such as reactivity and neutron

flux distributions.

The overall calculation scheme, which integrates these two phases, is illustrated below:

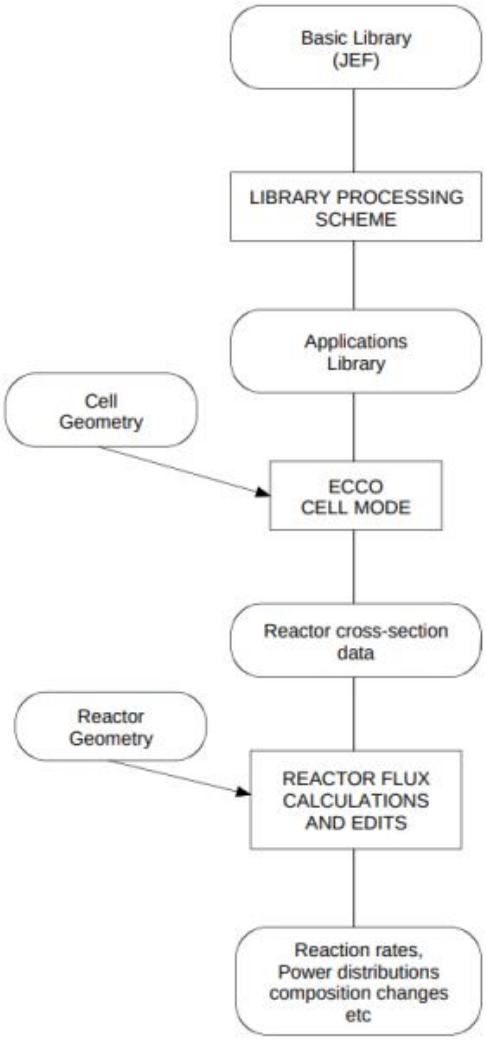

Figure 4.1: ERANOS calculation scheme

4.1.1 The ECCO Cell Code

As noted in the previous section, the ECCO cell code is designed to process original nuclear data libraries at 1968 (ultra-fine) energy groups (e.g., JEFF or ENDF/B) and produce condensed cross sections for use in reactor calculations. For computational efficiency, reactor calculations typically use a reduced number of energy groups compared to those in the original libraries, and material properties are **homogenized** within the calculation lattice cell. This approach enables a simplified core model while ensuring

that the cross sections and material properties are generated from refined cell or lattice calculations.

To perform **energy condensation** and **spatial homogenization**, ECCO requires detailed information about the geometry and materials of the cell under analysis. The input data for ECCO can be organized into two main components:

- Cell Description: Includes the geometry, material compositions, and boundary conditions of the cell;
- Calculation Procedure Description: Specifies the number of calculation steps and the operations to be performed at each stage, also called **ROUTE**.

Before analysing these two components in detail, it is important to emphasize that ECCO is a versatile code capable of handling any type of cell calculation, whether for thermal or fast reactor applications.

Cell description The geometric description of a cell in ECCO involves constructing geometries with varying levels of complexity, beginning with simple geometric elements referred to as *links* within ECCO. These links vary according to their dimensionality and can be:

- 0D (zero-dimensional, `HOMOGENEOUS`),
- 1D (`CYLINDRICAL`, `PLANE`),
- 2D (`SQUARE LATTICE`, `RECTANGULAR LATTICE`, `HEXAGONAL LATTICE`).

More generally, links are categorized as either *simple* or *lattice-type*. Each cell is represented using a three structure in which a simple model corresponds to a branch, while a lattice acts as a node capable of generating multiple branches.

The geometry is defined in a **nested** manner, progressing from the outermost link inward. Each link can contain other links or be filled with a homogeneous material, whose composition must be specified at a given temperature (thermal expansion coefficients can be included to account for temperature-dependent effects). If the inner link does not fully occupy the outer link, a uniform material must be specified in the remaining space. A **VOID** material can be used in such cases, effectively reducing the material density to zero; to avoid computational errors (such as divisions by zero densities), certain workarounds are applied, for example, homogenizing with the immediately adjacent geometry.

It is important to note that the permissible geometries depend on the method selected for computing the neutron flux within the cell, as will be discussed in the section on calculation methods.

Boundary conditions are defined on the faces of the outermost link, except in the case of homogeneous cells, where boundary conditions are not required. Various boundary conditions are available, as described in the ECCO manual, and their selection depends on the geometry of the cell under analysis.

In summary, ECCO is capable of handling both homogeneous and heterogeneous cells using suitable resolution methods. Additionally heterogeneous cells can be automatically homogenized during a computational step of the cross-section condensation process.

Calculation Procedure Description The procedure for generating the nuclear data library to be used by the reactor code for a specific case involves several sequential steps. The user typically defines the number of these steps and specifies, for each step, the approach for the geometrical schematization, energy group structure, list of nuclides, resonance shielding treatment, and flux calculation. This is essential because cross sections for different nuclides and reactions may require calculations at different levels of geometric detail or with varying energy group structures.

For instance, fine-group calculations (1968 groups in ECCO) may be performed using a homogenized cell, even if the original geometry is heterogeneous, to condense elastic scattering matrices for light elements efficiently. Conversely, standard broad-group calculations (33 groups in ECCO), using the subgroup method, can be conducted on the heterogeneous geometry of the same cell to handle the remaining nuclides and reactions.

ECCO offers two primary calculation routes: **"Reference"** and **"Fast."** The Reference route involves a fine-group treatment of elastic scattering, with subgroup parameters for resonance self-shielding also evaluated at the fine-group level. The Fast route similarly applies fine-group treatment for elastic scattering. Users may also select arbitrary group structures, provided that the outer boundaries of all structures align with those of the finest group structure in the general library. Further details can be found in [4].

Condensation of fluxes, cross sections, and other relevant quantities occurs whenever transitioning from a fine-group calculation step to a broader group step. Most cross sections are collapsed using flux weighting:

$$\sigma^G_{x,e,i} = \frac{\sum_{g\in G} \sigma^g_{x,e,i}\phi^g_i}{\phi^G_i}, \tag{4.1}$$

where:

- i: cell region,
- e: isotope,
- x: reaction type (e.g., total, capture, fission),
- g: fine energy group,
- G: broad energy group,
- $\phi^G_i = \sum_{g\in G} \phi^g_i$: collapsed flux.

It is important to note that some quantities are weighted using the current instead of the flux, as detailed in [4].

Homogenization of quantities can be performed within the calculation steps using multiple energy groups or in the final step to generate data for reactor calculations. Microscopic cross sections are homogenized using a volume (V), flux (φ), and number density (N) weighted average:

$$\sigma^g_{x,e} = \frac{\sum_i V_i \varphi^g_i N_{e,i} \sigma^g_{x,e,i}}{V \varphi^g N_e}, \tag{4.2}$$

where:

- $\varphi^g = \frac{\sum_i V_i \varphi_i^g}{V}$: homogenized flux,

- $N_e = \frac{\sum_i V_i N_{e,i}}{V}$: homogenized number density.

Calculation Scheme: ROUTE Each step is a transport calculation to evaluate the angular flux.

In the first step, the cell is homogenized, and using the 172-group cross-section library, the flux distribution is calculated either by imposing a fixed buckling (in the case of an infinite cell configuration) or by searching for the critical buckling value (in the case of a critical cell configuration).

In the second step, the calculation is performed using the original heterogeneous geometry, starting from the buckling obtained in the previous step while maintaining the same 172-group energy structure.

In the third step, the calculation is repeated with the energy structure expanded to the 1968-group (ultra-fine) cross-section library. For the main isotopes, a standard 1968-group library is used, while for the remaining isotopes, the 172-group structure is deconvoluted to match the 1968-group structure. Subsequently, the cross sections are **condensed** to the number of groups n.

In the fourth step, the calculation is carried out in the original heterogeneous geometry using the condensed n-group structure, and the buckling value is updated (noting that in the infinite configuration, the buckling remains unchanged, because is zero).

In the final step, the buckling value from the previous step is used, and the cell is **homogenized**, resulting in the homogenization of the cross sections. These newly **condensed** and **homogenized** cross sections are then saved and provided to reactor calculations.

From this point forward, the calculation scheme for the critical cell will be referred to as the **"REFERENCE ROUTE"**.

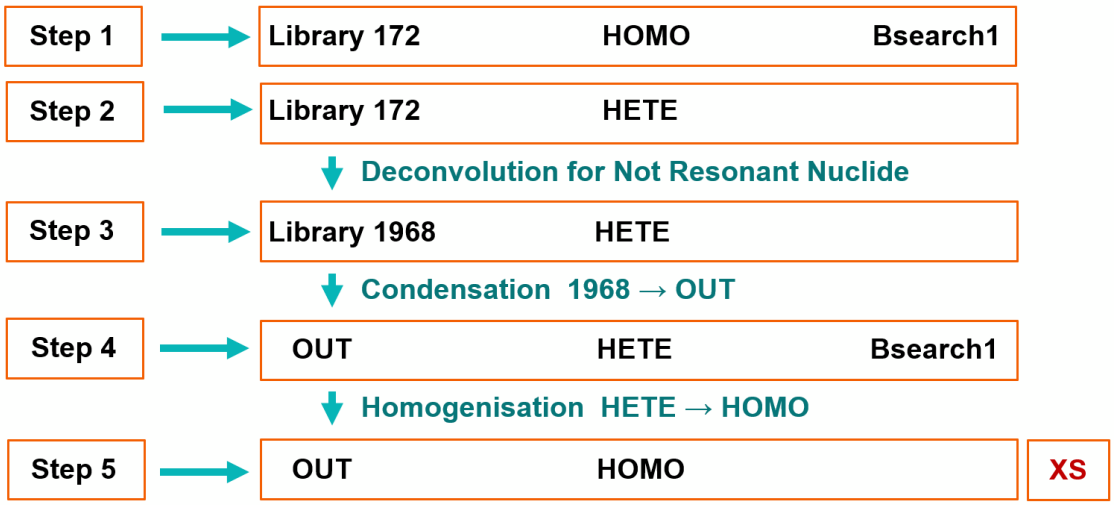

Figure 4.2: REFERENCE ROUTE scheme

This scheme was originally necessary when computers had significantly lower computational power than those available today. In fact, the first step could now be skipped, starting directly with the heterogeneous geometry and the critical buckling search, without a significant increase in computation time (on the order of minutes).

This thesis will not use the **REFERENCE ROUTE** because the stochastic code is not able to reproduce the leakage model in its calculations. For this reason, the route will be changed to the **ZERO BUCKLING ROUTE**. The differences lie in the first and fourth steps, where the REFERENCE ROUTE performs a *Bsearch* (to find the values of buckling), while in this new route, the buckling is set equal to zero, as the name suggests.

4.2 Stochastic ode: OpenMC

The Monte Carlo (MC) methods provide a statistical approach to estimate physical observables by performing computer-based sampling. These methods are essential for resolving integrals in scattering and fission source terms within the neutron transport equation (NTE) [12].

Using probability density functions (PDFs), it is possible to analyse the evolution and probability of event occurrences, such as the number of neutron collisions during their lifetime. The PDF, denoted as $f(x)$, depends on the independent variable x and contains all the information about the probability of event occurrence. The space where the density function is defined is the *Sample Space* (S), which in nuclear physics corresponds to the phase-space (three spatial variables and one energy variable), encapsulating all NTE operators (Collision, Transport, Fission, Scattering).

MC methods utilise *Random Variables* (ξ) to perform statistical sampling from the PDF, where ξ maps outcomes from the sample space to real numbers. Random variables

can be discrete (fixed event probabilities) or continuous (taking any value within an interval). The PDF, $f_\xi(x)$, is positive and normalised, ensuring:

$$\int_a^b f_\xi(x)\,dx = 1. \tag{4.3}$$

The mean value for a distribution, corresponding to the first-order moment, is given by:

$$E[x] = \int_a^b x f_\xi(x)\,dx. \tag{4.4}$$

MC sampling allows estimation of this mean value using:

$$\bar{\xi}^{(N)} = \frac{1}{N}\sum_{i=1}^{N}\xi_i, \tag{4.5}$$

where N is the number of experiments, with each ξ_i sampled independently and identically according to the PDF. As $N \to \infty$, the sample average converges to the mean value.

A general integral can be rewritten as:

$$R = \int_D \xi(x) f_\xi(x)\,dx, \tag{4.6}$$

where $\xi(x)$ is an estimator dependent on the integral under consideration and D is the integration domain. Since finite integrals equate to the expected value of the integrand, Eq. (4.5) can be utilised to evaluate integrals in the NTE.

The estimation of physical phenomena through statistical sampling inherently carries uncertainty, typically expressed as variance, calculated via the second-order moment:

$$E[x^2] = \int_a^b x^2 f_\xi(x)\,dx, \tag{4.7}$$

$$\sigma^2(x) = E[x^2] - (E[x])^2. \tag{4.8}$$

The sample variance during MC sampling is:

$$\bar{\sigma}_x^2 = \frac{1}{N-1}\sum_{i=1}^{N}(\xi_i - \bar{\xi}^{(N)})^2, \tag{4.9}$$

and converges to the distribution variance as $N \to \infty$. Lower variance indicates higher estimation accuracy. Furthermore, the standard deviation (SD) and relative standard deviation (RSD) are defined as:

$$\bar{\sigma}_x = \sqrt{\bar{\sigma}_x^2}, \tag{4.10}$$

$$\text{RSD} = \frac{\bar{\sigma}_x}{\bar{\xi}^{(N)}}. \tag{4.11}$$

In MC methods, the variance convergence is inversely proportional to $\sqrt{N}$, implying that to reduce variance, an increase in sample size (and computational time) is necessary.

4.2.1 Monte Carlo Methods for Particle Transport

MC methods for particle transport simulate the behaviour of neutral particles (neutrons, photons) using statistical sampling to solve the transport equation, including displacement and interaction terms. The exponential distribution PDF for particle displacement is:

$$f(x) = \Sigma_t e^{-\Sigma_t x}, \quad x \geq 0, \tag{4.12}$$

where Σ_t is the total macroscopic cross-section, constant for homogeneous media, with the mean free path:

$$\langle x \rangle = \frac{1}{\Sigma_t}. \tag{4.13}$$

To determine particle paths, a *Random Walk* (RW) is generated using the inverse transform method by relating the cumulative density function (CDF):

$$F(x) = 1 - e^{-\Sigma_t x} = \rho, \tag{4.14}$$

where ρ is a uniformly distributed random number in [0,1). Inverting Eq. (4.14) yields:

$$l = -\frac{\ln(1-\rho)}{\Sigma_t}, \tag{4.15}$$

which computes the particle's path length until its next collision.

MC codes simulate numerous particle histories, estimating flux or reaction rates through tallies during fixed source or eigenvalue (criticality) modes, and in this OpenMC is employed in eigenvalue mode.

4.2.2 OpenMC Estimators

Tallies in MC codes compute macroscopic quantities through:

$$X = \int d\vec{r} \int d\Omega \int dE\, f(\vec{r}, \Omega, E)\phi(\vec{r}, \Omega, E), \tag{4.16}$$

where f is the scoring function and ϕ is the flux.

OpenMC supports three estimators:

1. **Analog Estimator**: counts the number of actual reactions:

$$R_x = \frac{1}{W} \sum_{i \in A} w_i, \tag{4.17}$$

   where W is the total particle weight.

2. **Collision Estimator**: scores contributions at each collision:

$$\phi = \frac{1}{W} \sum_{i \in C} \frac{w_i}{\Sigma_t(E_i)}. \tag{4.18}$$

3. **Track-length Estimator** (default in OpenMC):

$$V\phi = \frac{1}{W} \sum_{i \in T} w_i l_i, \tag{4.19}$$

   where l_i is the path length within the desired volume.

Chapter 5

Results

5.1 Introduction to Nuclear Reactors

Nuclear reactors are devices designed to initiate, control, and sustain nuclear fission reactions for the purpose of generating thermal energy, which is subsequently converted into electricity. Over time, technological advancements have led to the development of several generations of nuclear reactors, each introducing improvements in safety, efficiency, and environmental sustainability [18].

Generational Classification:

- **Generation I**: Prototype reactors built during the 1950s and 1960s, most of which are now decommissioned.
- **Generation II**: Commercial reactors currently in operation in many countries, such as PWRs (Pressurized Water Reactors) and BWRs (Boiling Water Reactors).
- **Generation III / III+**: Advanced reactors featuring improved efficiency and passive safety systems (e.g., EPR, AP1000).
- **Generation IV**: Reactors currently under development, aiming to enhance sustainability, reduce long-term radioactive waste, increase resistance to nuclear proliferation, and lower operational costs.

5.2 The Lead - Cooled Fast Reactor

Among the Generation IV technologies, in this section, the principles, technological challenges, and design features of Lead - Cooled Fast Reactors (LFRs) are presented, with detailed focus on the ALFRED demonstrator core, focus also of this work [13].

Lead-Cooled Fast Reactors are fast-spectrum systems operating at high temperatures with pressures close to atmospheric levels. Lead is used as coolant due to its high boiling point of $1737 \hat{A} \check{r} C$ and chemical inertness, which eliminates the risk of violent reactions in the event of contact of the coolant with air or water.

The absence of explosive reactions with lead simplifies the reactor design, removing the necessity for an intermediate heat exchanger, and its high thermal inertia and density

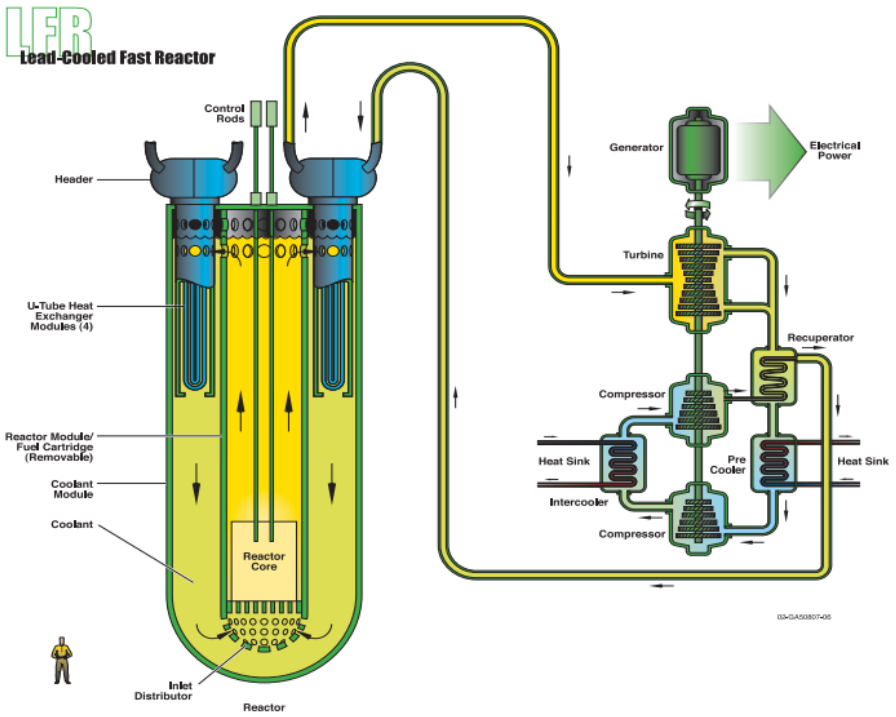

Figure 5.1: Scheme of LFR reactor. [19]

enable effective decay heat removal through natural circulation. Neutronic properties of lead allow wider fuel rod spacing, reducing pressure drops while preserving the fast neutron spectrum.

Current designs operate with coolant outlet temperatures between $480 \hat{A} \check{r} C$ and $530 \hat{A} \check{r} C$ due to corrosion limitations, with targets up to $750 - 880 \hat{A} \check{r} C$ in the future, enabling efficiencies of at least 42% in secondary cycles [14].

Two design configurations were studied: loop and pool-type, with the pool-type prevailing to avoid seismic issues with lead-filled piping. Reference Generation IV LFR systems include the ELFR (600 MWe), the BREST-OD-300 (300 MWe), and SSTAR (10 - 100 MWe). The European design evolved from ELSY, which introduced compact pooltype configurations with integrated steam generators.

A critical challenge remains the development of structural materials capable of withstanding hightemperature lead corrosion, necessitating extensive material qualification under irradiation conditions.

5.3 The ALFRED Features

ALFRED (Advanced Lead Fast Reactor European Demonstrator) serves as the European demonstrator for LFR technology and as a prototype for LFR -SMR applications, designed with a power of 300 MW_{th} (125 MW_{el}) [15].

Its pooltype design ensures passive safety by maintaining lead temperatures between

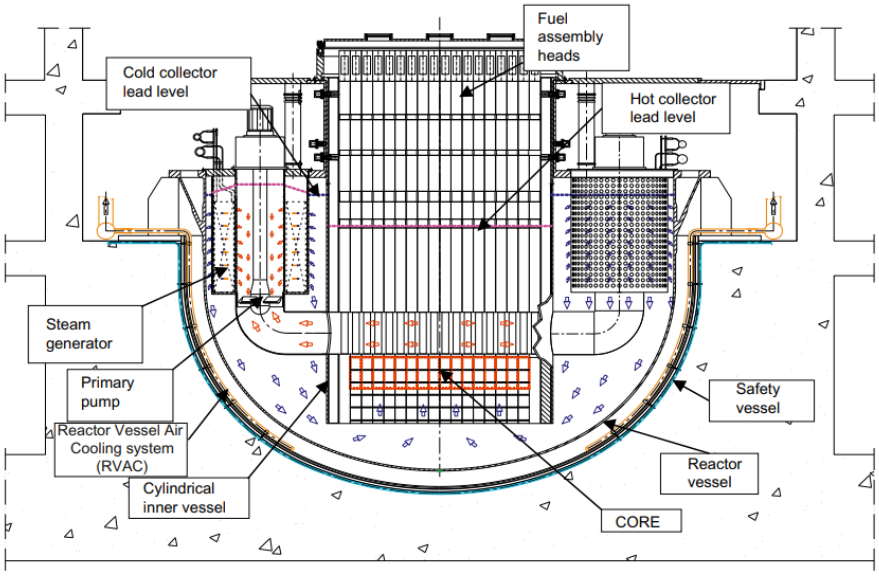

Figure 5.2: Primary system of ELSY reactor [21].

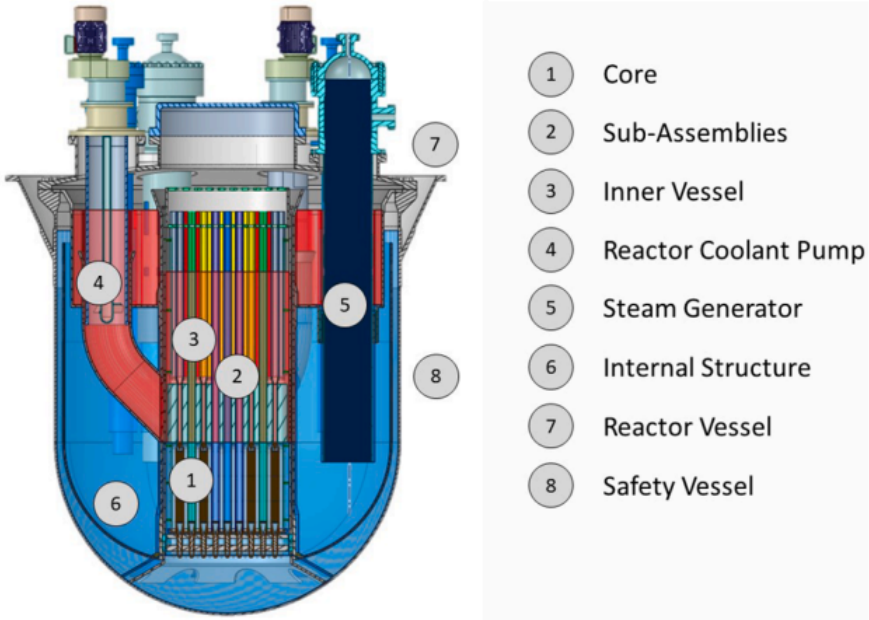

Figure 5.3: Primary system of the ALFRED demonstrator [16].

380ÂřC and 600ÂřC, preventing coolant solidification and limiting corrosion rates. Due to the limited availability of fastspectrum irradiation facilities, ALFRED will qualify protective coatings within its own operational cycles.

In 2018, the core design was revised to incorporate a central irradiation position and

phased power and temperature increases to achieve material qualification under operational conditions.

The updated core comprises 151 main assemblies: 134 Fuel Assemblies (FAs), 12 Control Rods (CRs), 4 Safety Devices (SDs), and 1 Test Assembly, surrounded by 102 Dummy Assemblies for reflection and shielding.

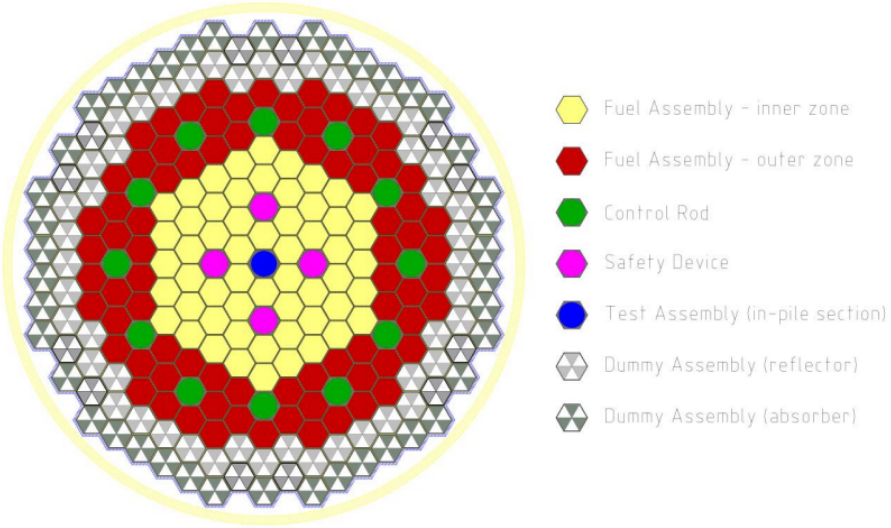

Figure 5.4: Crosssectional map of the ALFRED core [15].

MOX fuel enrichment is distributed as:

- 56 inner FAs with 20.5 wt.% $PuO_{1.97}$,
- 78 outer FAs with 26.2 wt.% $PuO_{1.97}$,

supporting a five - batch annual refueling strategy, with a targeted maximum burnup of 100 MWd/kgHM and optimized power distribution for reactivity control and safety [16].

5.3.1 The ALFRED Fuel Pin

Fuel pins consist of sintered MOX pellets with a diameter of 9 mm and a 2 mm central hole to reduce pellet cladding mechanical interaction (PCMI). The AIM1 steel cladding has a thickness of 0.6 mm with a 0.15 mm gap to accommodate assembly tolerances and limit PCMI.

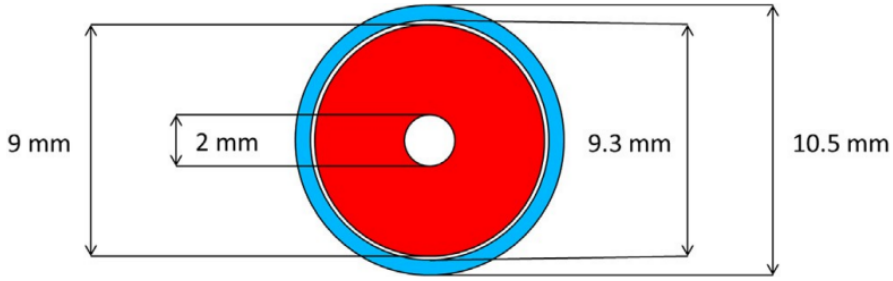

Figure 5.5: Cross-section of an ALFRED fuel pin [20].

5.3.2 The ALFRED Fuel Assembly

Each hexagonal fuel assembly features an AIM1 steel wrapper enabling lead outlet temperature monitoring, containing 126 fuel pins arranged in a triangular lattice around a central dummy pin for diagnostics, with a lattice pitch of 13.6 mm, a wrapper thickness of 3.5 mm, and a 4 mm interassembly gap for lead bypass flow.

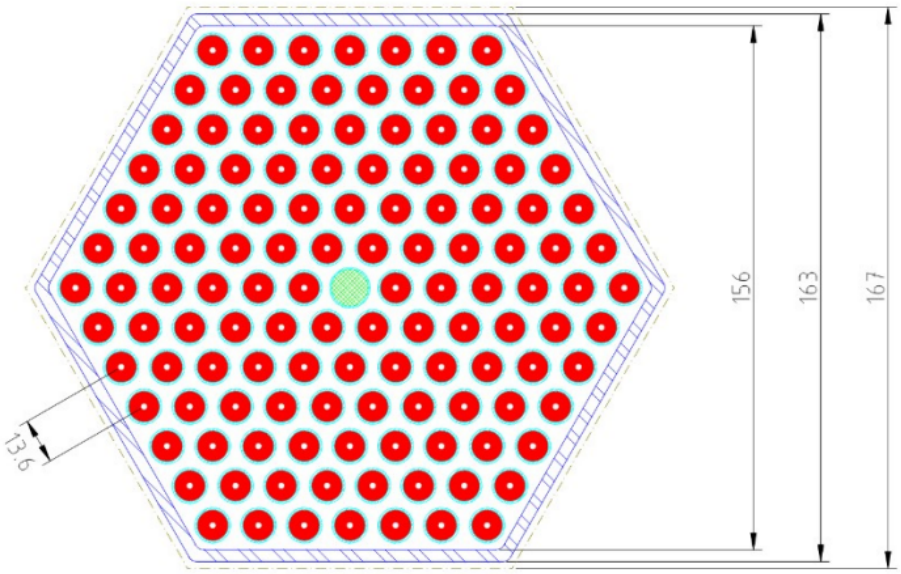

Figure 5.6: Fuel assembly crosssection at the active region [16].

This structured overview provides a comprehensive technical foundation on ALFRED's design, operational safety strategy, and its role in the development of Generation IV LFR technology.

5.4 Analysis

In this chapter, we will discuss of outputs of ECCO and Open MC. The results will be show from the simplest geometry, the homogeneous pin, to the heterogeneous assembly.

In each of this geometry will find similar comparison expect for the homogeneous, which is the simplest and for this reason is the perfect subject to isolate the discrepancies without an overlapping of effect.

Normalizations Before to show the result is important to elaborate what are these normalizations and how we can reproduced them. By starting from the eigenvalue problem in the form of operators, it is possible to obtain two normalizations.

$$\hat{L} \cdot \varphi = \frac{1}{k} \hat{F} \cdot \varphi \tag{5.1}$$

where $\hat{L}$ is the reduced absorption operator [12], and $\hat{F}$ is the fission operator.

$\hat{L} \cdot \varphi = 1$ Thanks this notarization it is possible underline the contribution og each fissionable isotopes in each group on the k_{inf} The 5.1 become:

$$\hat{F_n} \cdot \varphi = k \tag{5.2}$$

and the key is the comparison of two calculation

$$\hat{F_n} \cdot \varphi - \hat{F_n'} \cdot \varphi' = k - k' = \Delta k \tag{5.3}$$

Where the prime indicates the value obtained from the OpenMC calculation, while the absence of a prime refers to the ECCO calculation.

By adding the assumption of constant flux across the entire region, we can write the operators as a summation over the groups of macroscopic reaction rates and a summation over the nuclides.

$$\hat{F_n} \cdot \varphi = \sum_g \sum_i rr_{i,g,\nu f} = k \tag{5.4}$$

As shown previously we can obtain the difference between them for each individual group and nuclide.

$\hat{F} \cdot \varphi = 1$ Similarly as previus with this notarization it is possible underline the contribution of each isotopes in each group on the ρ The step and assumption are the same.

$$\hat{L_n} \cdot \varphi = \frac{1}{k}$$

Compare two calculation:

$$\hat{L_n} \cdot \varphi - \hat{L_n'} \cdot \varphi' = \rho' - \rho = \Delta\rho$$

Each Reduced absorption operator is:

$$\hat{L_n} \cdot \varphi = \sum_g \sum_i (rr_{i,g,t} - rr_{i,g,s}) = \rho$$

5.5 Homogeneous Pin

The **homogeneous pin** is an inner fuel pin of the ALFRED reactor. The pin composition was taken from the reactor benchmarking in [7]. The model is analyzed under the following conditions:

- homogeneous ALFRED fuel pin ;
- *infinite lattice* (no leakages);
- no dilatation (geometry in cold conditions), and at $T = 973.6K$ [7];
- nuclear libraries used ENDB-F VII.

The weight homogenization was then performed before the calculation as follows:

- V_f: volume of the fuel;
- V_g: volume of the gap;
- V_c: volume of the cladding;
- $V_{tot} = V_f + V_g + V_c$: total volume of the pin.

For each isotope i, the homogenized atomic density $\bar{N}_i$ over the pin volume is calculated as:

$$\bar{N}_i = \frac{1}{V_{tot}} \left(N_{i,f} \cdot V_f + N_{i,g} \cdot V_g + N_{i,c} \cdot V_c \right)$$

where:

- $N_{i,f}$: atomic density of isotope i in the fuel,
- $N_{i,g}$: atomic density of isotope i in the gap,
- $N_{i,c}$: atomic density of isotope i in the cladding.

The analyses that will be performed on the homogeneous pin are:

1. Comparison of the different setups used for the flux calculation.;
2. resonance treatment;
3. evaluations of errors.

The route used to perform the calculations consists of the following steps:

1. Calculation of the flux on 172 groups;
2. Calculation of the flux on 1968 groups and condensation of **new** Cross section on X groups;
3. Calculation of the flux on **new** cross section.

For the comparison between the methods, the condensation was performed three times the first on 1G, the second on 33G (ECCO-33) and in the end on 172G (XMAS).

5.5.1 Comparison between methods

Four calculations are made chancing only the method inside the run. This step is very important , because is the base of work, as a basis of the subsequent analysis that will investigate the best method to represent the geometry. As a starting point, a 1-group analysis was employed:

		P1		B1	
		Consistent	Inconsistent	Consistent	Inconsistent
k_{inf}		1.35166	1.35166	1.35166	1.35166
1G Macro XS	Total	-	0	0	0
	Capture	-	0	0	0
	ν Fis	-	0	0	0
	Elastic	-	0	0	0
	n,xn	-	0	0	0

Table 5.1: Difference between the setups.

It can be clearly seen that that there is no difference between the Pn and Bn expansions, but it was necessary to proceed with the 33-group analysis.

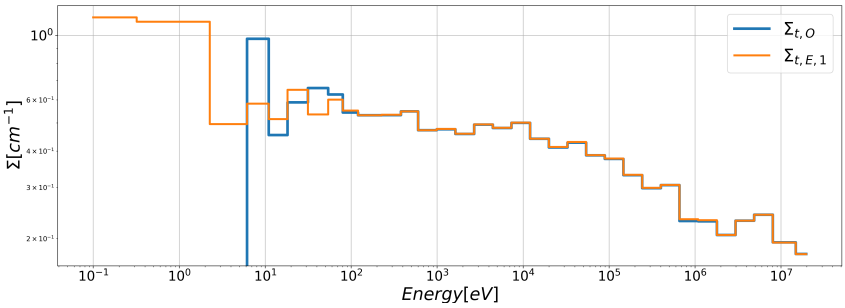

Figure 5.7: Cross-section for total reactions.

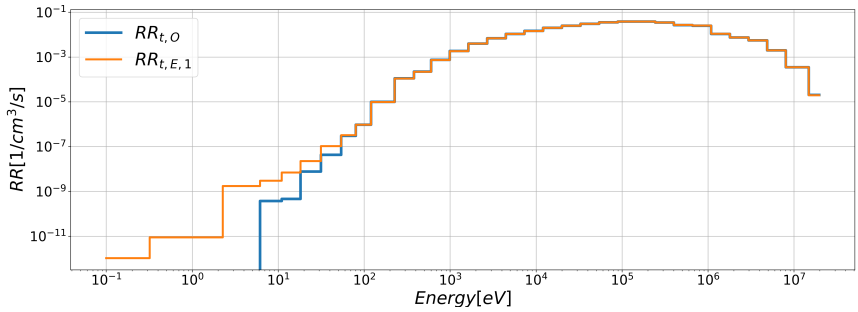

Figure 5.8: Microscopic reaction rate for total reactions.

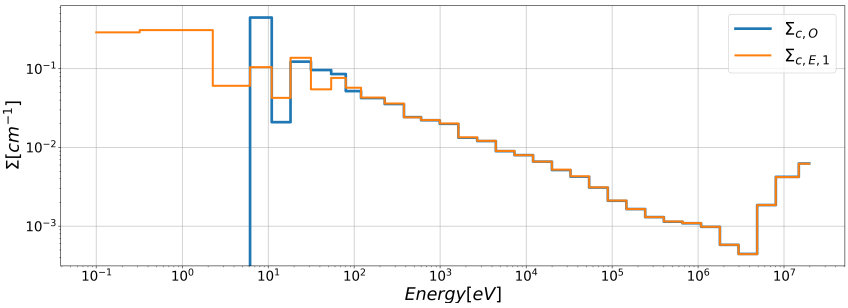

Figure 5.9: Cross-section for capture reactions.

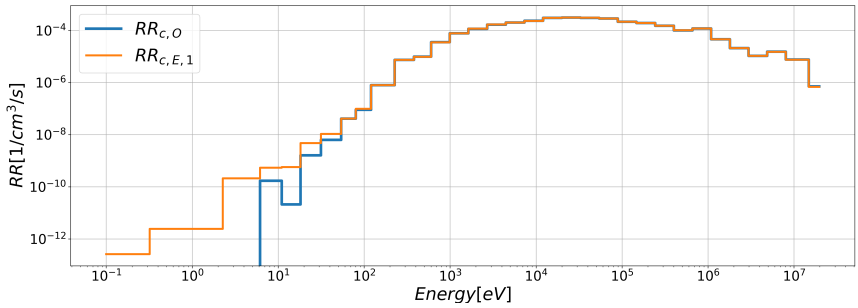

Figure 5.10: Microscopic reaction rate for capture reactions.

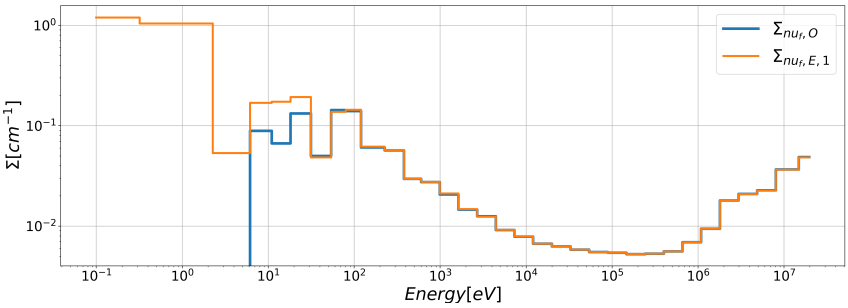

Figure 5.11: Cross-section for nu-fission reactions.

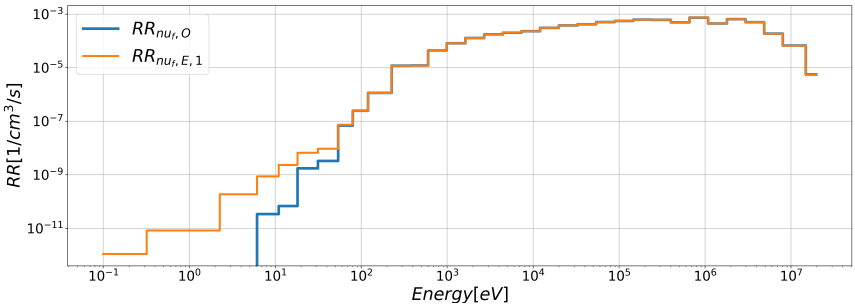

Figure 5.12: Microscopic reaction rate for nu-fission reactions.

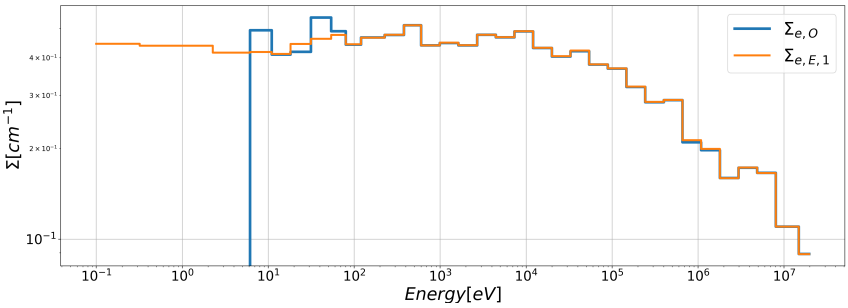

Figure 5.13: Cross-section for elastic reactions.

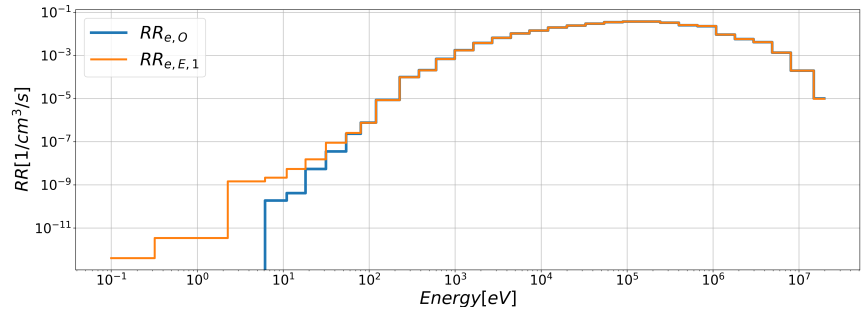

Figure 5.14: Microscopic reaction rate for elastic reactions.

The following are the comparisons of the different setups for the 33-group calculations. In the legend there is only the subscript "E" in general form, without specify if is P1 consisten, P1 inconsiste, ecc. because there are not differences as show the next table.

		P1		B1	
		Consistent	Inconsistent	Consistent	Inconsistent
macro XS	Total	-	0.0	0.0	0.0
	Capture	-	0.0	0.0	0.0
	ν Fis	-	0.0	0.0	0.0
	Elastic	-	0.0	0.0	0.0
RR	Total	-	0.0	0.0	0.0
	Capture	-	0.0	0.0	0.0
	ν Fis	-	0.0	0.0	0.0
	Elastic	-	0.0	0.0	0.0

Table 5.2: Root mean square errors with respect P1 consistent

This table shows the Root Mean Square (RMS) differences between the macroscopic cross sections and reaction rates with respect to the OpenMC values, demonstrating that the model behaves consistently. To be sure it is suitable said that the method are already identical, but was made also an analysis on 172 groups, but i will show only the table with the RMS, because the result is the same of previeuv analysis.

The errors between the setup are zero and for this reason the next result are evaluated on **P1 Consistet**, because it is the setup recommanded by tecnical guide in ECCO.

5.5.2 Resonance treatment

To eliminate interpolation errors due to the input nuclear data, three temperatures were used: 293.6 K, 573.6 K, 973.6 K, and 1473.6 K. In parallel, 4 fixed temperature libraries were also created in Open Mc to avoid the same problem. For this reason there would be 4 sections that will change only on the temperature and in each of them we would see the comparison of flux to underline if a finer mesh on energy is useful or not. To

		P1		B1	
		Consistent	Inconsistent	Consistent	Inconsistent
macro XS	Total	-	0.0	0.0	0.0
	Capture	-	0.0	0.0	0.0
	ν Fis	-	0.0	0.0	0.0
	Elastic	-	0.0	0.0	0.0
RR	Total	-	0.0	0.0	0.0
	Capture	-	0.0	0.0	0.0
	ν Fis	-	0.0	0.0	0.0
	Elastic	-	0.0	0.0	0.0

Table 5.3: Root mean square errors with respect P1 consistent

facilitate reading, only 973.6K analisys will be reported but the other are summarized in the table ??. With respect the route of comparison of methods, there is no differnts in the number of step but in this paragraph the route will have as output only cross section on 172 groups, to avoid undesirable phenomena on condensation.

For clarity, the steps of this workflow are reported again below:

1. Calculation of flux on 172 groups;
2. Calculation of flux on 1968 groups and condensation of new Cross section on **172 groups;**
3. Calculation of flux on new cross section.

As numbered in the previous list, the first step will have the subscript $X_{E,1}$, the second $X_{E,2}$ and the third $X_{E,3}$. The errors will have $\varepsilon_{E,1/O}$ is the Root Mean Square between the step 1 of ECCO and the result of OpenMC (O), and similir for the other.

973.6 K Let's start on the comparison of the k_{inf} in each step:

Results	k_1	$k_{2,3}$	OpenMc	$\Delta k_{1,2}$	$\Delta k_{1,O}$	$\Delta k_{2-3,O}$
973.6K	1.35880	1.35166	1.35374 $\pm$0.00017	-714 pcm	506pcm	-208pcm

Table 5.4: Comparison of k_{inf} between each step and the reference.

This initial result already shows the impact on the model of using the fine library in the second step. Moreover I like to remember that is impossible start at first step with data taken from 1968G because insede it there are only the data of resonce isotopes. Indeed the $\Delta k_{1,2}$, which is only a subtraction, shows a huge difference on k, and the $\Delta k_{1,O}$ and $\Delta k_{2-3,O}$ prove that the second is closer.

Moving on to the flux plots:

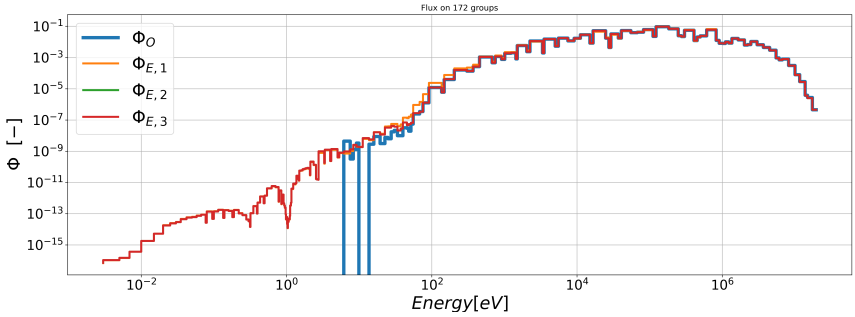

Figure 5.15: Flux on 172 groups of homogeneous pin.

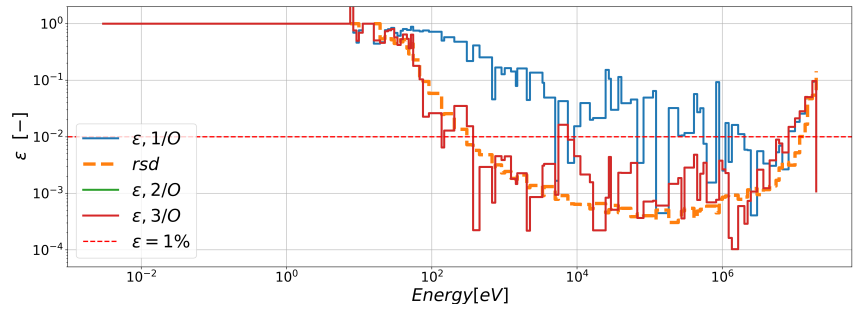

Figure 5.16: Comparison of the flux on 172 groups of homogeneous pins.

In the 5.15, ECCO fluxes and the OpenMC flux have an obvious difference at low energy values, the OpenMc has no values, and from our point of view is 0. This is a logical consequence arising from the choice of reactor type. Alfred is a fast reactor and therefore its spectrum will be concentrated on high energy values, where corresponds a high probability of having neutrons with that energy. Therefore having made some neutron calculations with OpenMC trying to have an uncertainty on the k_{inf} of about 10 pcm, it is possible that all the neutrons simulated on the model did not reach that range. This idea is also enhanced by the second plot showing rsd(relative standard deviation). The yellow dashed line is in the shape of a 'parabola' and tells us the uncertainty that each energy range has, in the middle we find the lowest values and that are the energy values at which there is more probability to find neutrons, and at the sides less and less.Also for this reason the root mean square, is not calculated on all groups (it would result in a very high error) but only on those in which OpenMC value is meaningful according to the formula 5.5.
Indeed the zeros values and the values that has the some order their standard deviations aren't used.

$$\varepsilon_{1,O} = \sqrt{\frac{1}{N}\sum_{g=1}^{N}\left(\frac{x_{E,1,g} - y_{O,g}}{x_{E,1,g}}\right)^2} \tag{5.5}$$

Root Mean Square	
$\varepsilon_{1,O}$	0.45341
$\varepsilon_{2/3,O}$	0.0108
$\varepsilon_{1,2/3}$	0.78860
$\varepsilon_{2,3}$	0.00019

Table 5.5: Comparison of RMS of the Flux on 172 groups of homogeneous pins.

Both the two plots and the table show the trend described above, where refinement shows a better result.

It is possible notice that the second step, which introduce a better behaviour under resonance phenomena and it is evidence on the small error of $\varepsilon_{2,O}$ and $\varepsilon_{3,O}$.

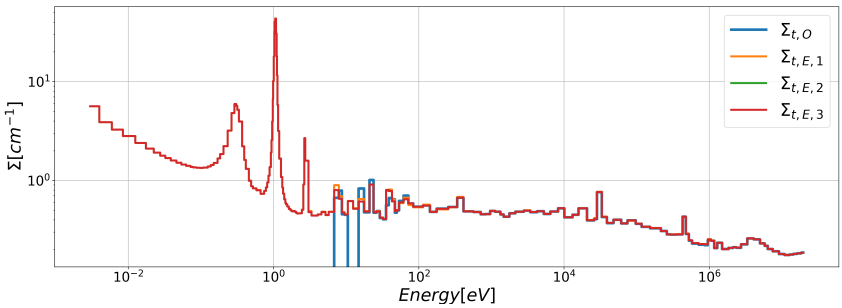

Figure 5.17: Cross-section for total reactions.

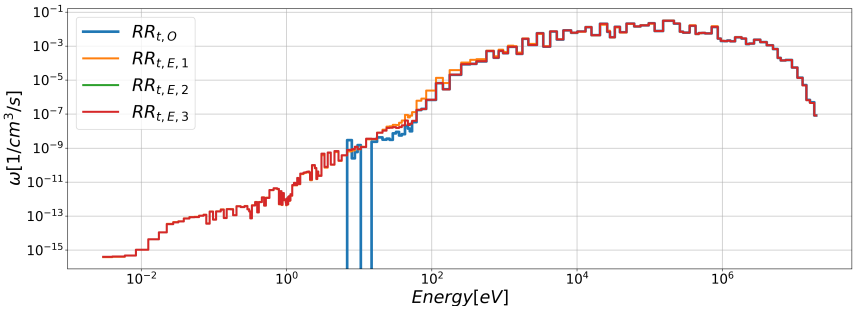

Figure 5.18: Microscopic reaction rate for total reactions.

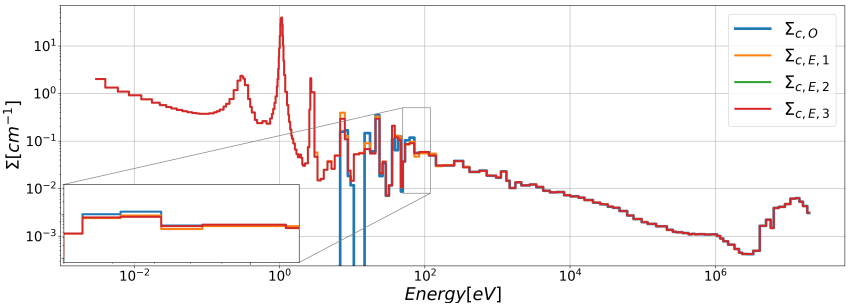

Figure 5.19: Cross-section for capture reactions.

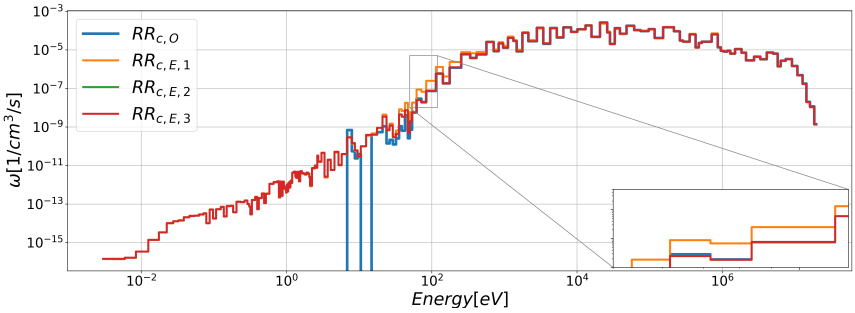

Figure 5.20: Microscopic reaction rate for capture reactions.

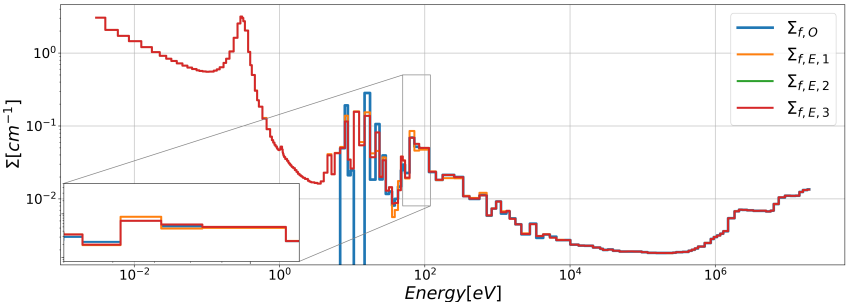

Figure 5.21: Cross-section for nu-fission reactions.

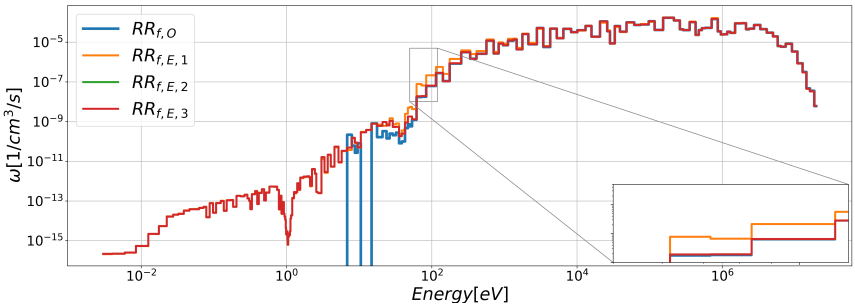

Figure 5.22: Microscopic reaction rate for nu-fission reactions.

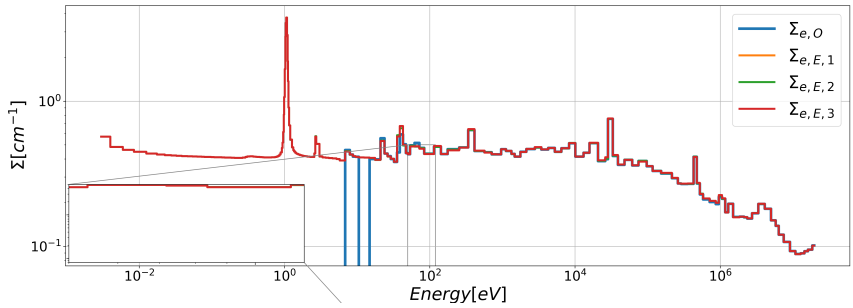

Figure 5.23: Cross-section for elastic reactions.

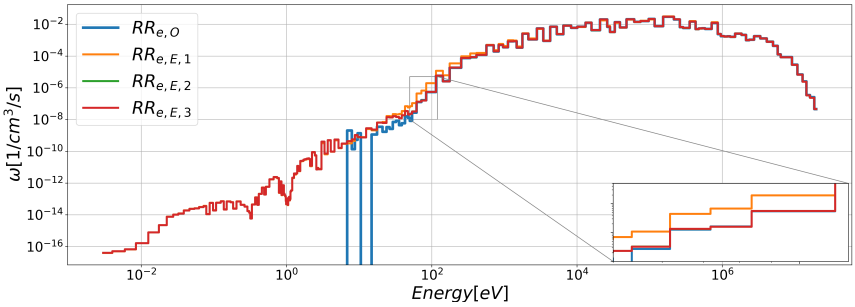

Figure 5.24: Microscopic reaction rate for elastic reactions.

	Root Mean Square			
973.6 K	Σ_t	Σ_c	Σ_f	Σ_e
$\varepsilon_{1,O}$	0.02537	0.01905	0.03633	0.02533
$\varepsilon_{2/3,O}$	0.01943	0.02784	0.01124	0.01892
$\varepsilon_{1,2/3}$	0.01442	0.04893	0.06284	0.06284
$\varepsilon_{2,3}$	0.0	0.0	0.0	0.0

Table 5.6: Root mean square on macroscopic cross section.

Table 5.6 presents the Root Mean Square (RMS) of the relative errors on macroscopic cross sections: Σ_c (capture cross section), Σ_f (fission cross section), and Σ_e (extinction cross section), comparing ECCO calculations across different steps.

It can be seen that the error between step 2 and 3 of ECCO of the cross sections is zero, since even if the flow is calculated on XMAS the output of the second coincides with the cross sections used by the third. What is expected is that the same error on reaction rate is different to zero.

	Root Mean Square			
973.6k	RR_t	RR_c	RR_f	RR_e
$\varepsilon_{1,O}$	0.47912	0.47184	0.47501	0.57462
$\varepsilon_{2/3,O}$	0.02509	0.01656	0.03331	0.02561
$\varepsilon_{1,2/3}$	0.49481	0.48159	0.49480	0.49245
$\varepsilon_{2,3}$	0.00012	0.00015	0.00012	0.00793

Table 5.7: Root mean square on macroscopic reaction rates.

The $\varepsilon_{2,3}$ can be seen as a check on ECCO, because from definition the cross sections at the output of 2-nd step are the same of the cross sections used in the 3-rd, but this is not true for the flux because in the second step is evaluated on 1968 gruops and then condenseted on 172 while in the third step is evalueted with the new cross section. In other words, it is inferred that the flux calculated using the cross sections on 1968 and after condensation on 172 groups and condenses the cross sections, is different from the flux calculated using the latter cross sections.

Then there are the microscopic cross-section and reaction rates:

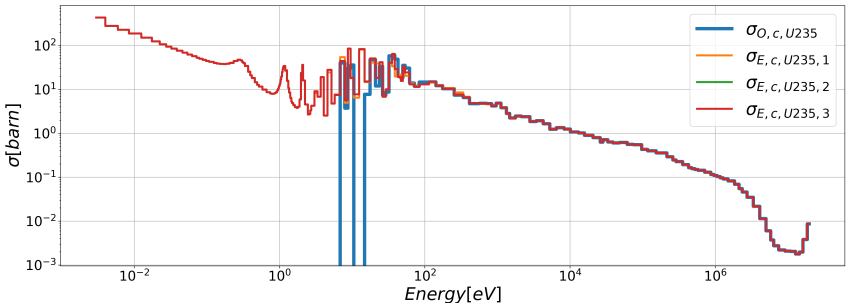

Figure 5.25: Microscopic cross-section for U-235 capture reaction.

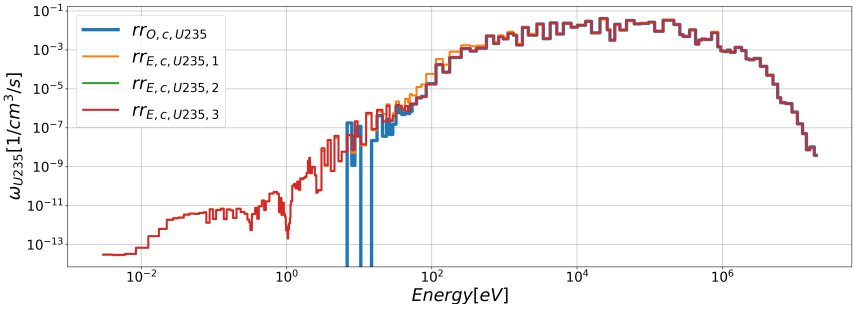

Figure 5.26: Microscopic reaction rate for U-235 capture reaction.

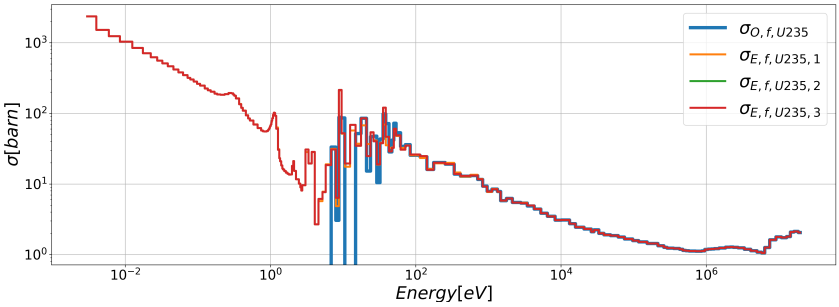

Figure 5.27: Microscopic cross-section for U-235 fission reaction.

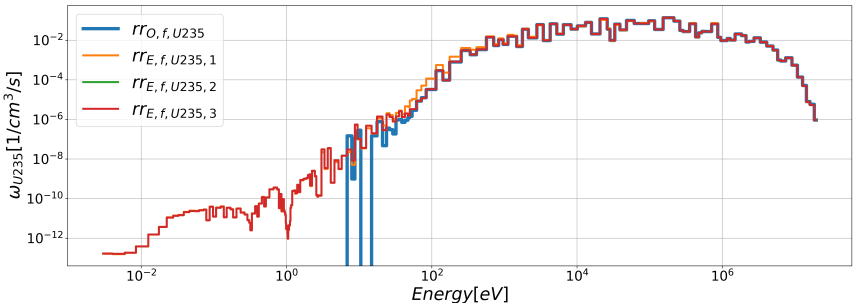

Figure 5.28: Microscopic reaction rate for U-235 fission reaction.

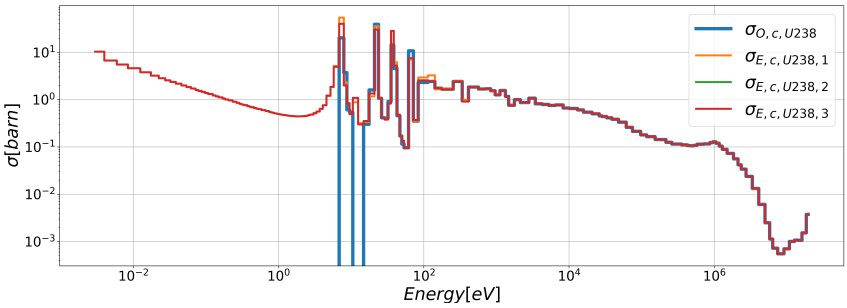

Figure 5.29: Microscopic cross-section for U-238 capture reaction.

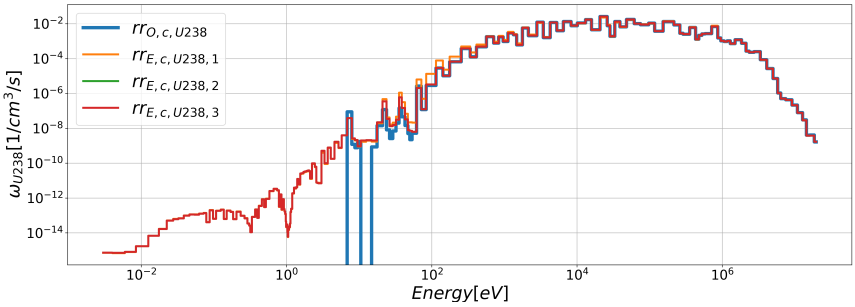

Figure 5.30: Microscopic reaction rate for U-238 capture reaction.

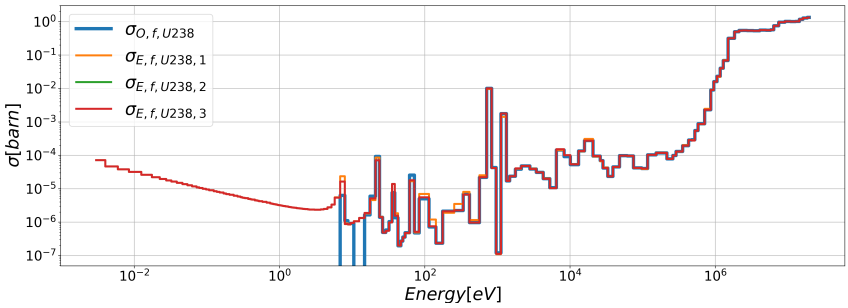

Figure 5.31: Microscopic cross-section for U-238 fission reaction.

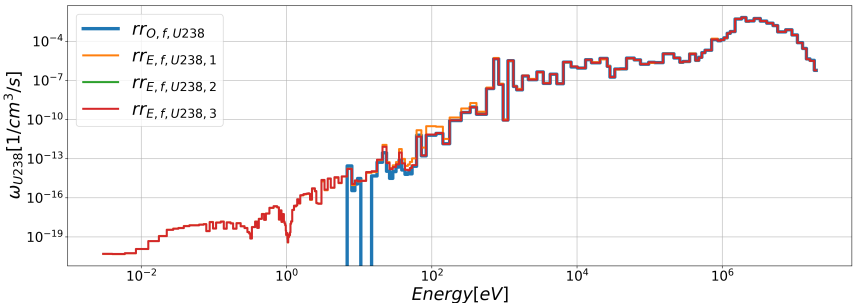

Figure 5.32: Microscopic reaction rate for U-238 fission reaction.

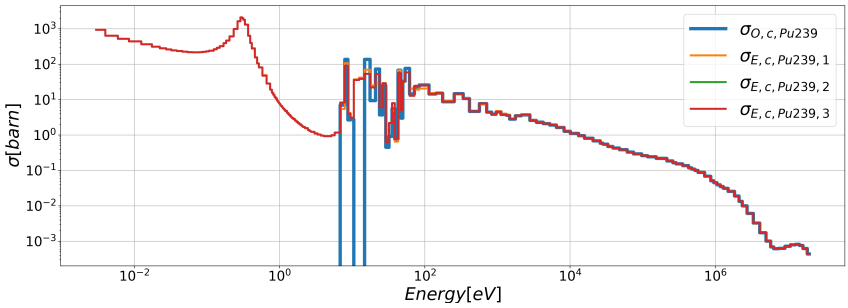

Figure 5.33: Microscopic cross-section for Pu-239 capture reaction.

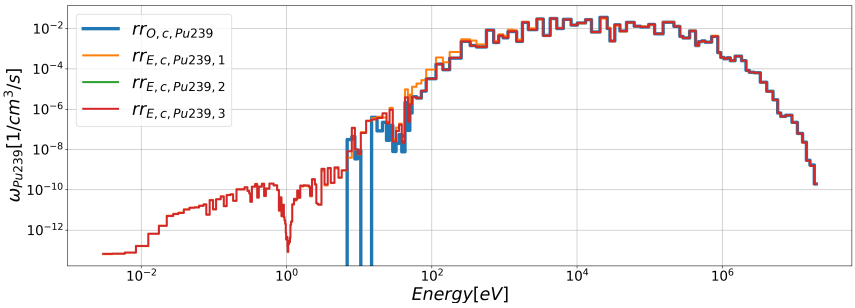

Figure 5.34: Microscopic reaction rate for Pu-239 capture reaction.

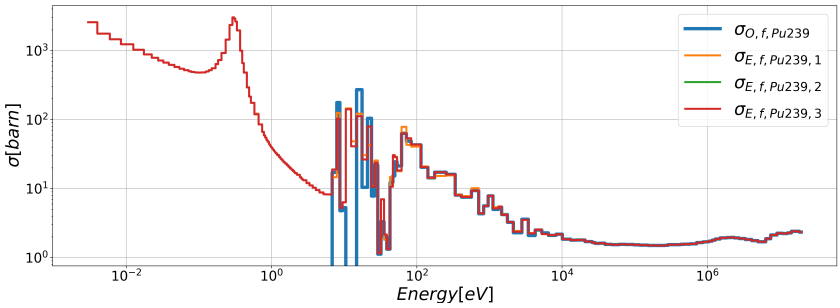

Figure 5.35: Microscopic cross-section for Pu-239 fission reaction.

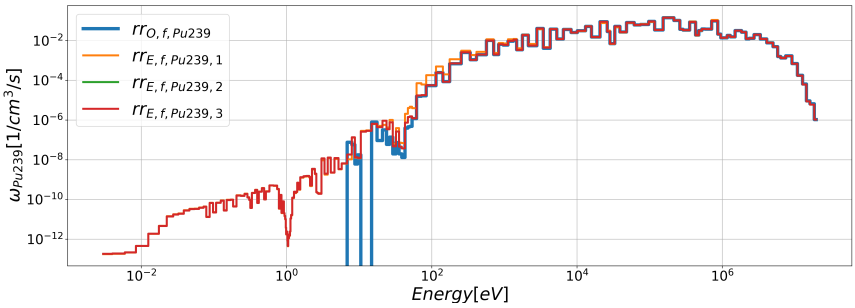

Figure 5.36: Microscopic reaction rate for Pu-239 fission reaction.

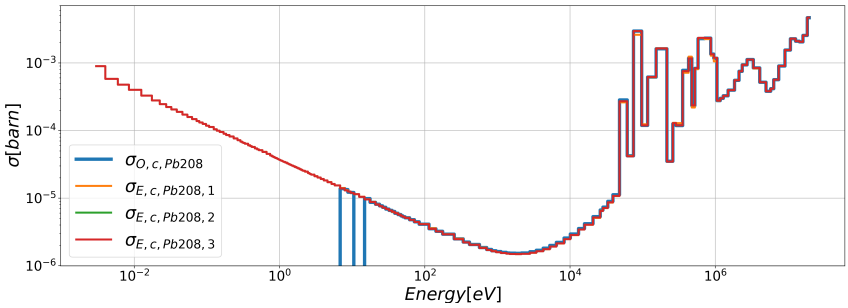

Figure 5.37: Microscopic cross-section for Pb-208 capture reaction.

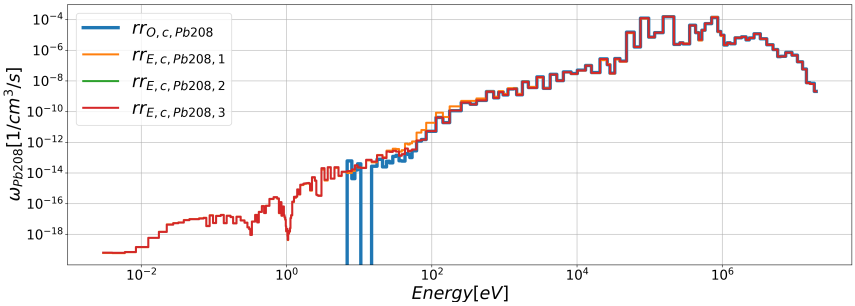

Figure 5.38: Microscopic reaction rate for Pb-208 capture reaction.

Root Mean Square							
	U^{238}		U^{235}		Pu^{239}		Pb^{208}
	σ_c	σ_f	σ_c	σ_f	σ_c	σ_f	σ_c
$\varepsilon_{1,O}$	0.44283	0.445208	0.46675	0.45633	0.47675	0.43088	0.43328
$\varepsilon_{2/3,O}$	0.00957	0.02056	0.00054	0.00545	0.01356	0.00096	0.08940
$\varepsilon_{1,2/3}$	0.45133	0.48346	049215	0.462620	0.48207	0.46364	0.41806
$\varepsilon_{2,3}$	0.0	0.0	0.0	0.0	0.0	0.0	0.0

Table 5.8: Root mean square on microscopic cross section for isotopes and reaction type.

There is the same performance of the macroscopic cross section and reaction rate, where the effect of high number of groups improve the flux and the reaction rate with respect the reference, and in addition we notice that the error between untreated cross sections and those treated with refinement is very high.

Now the self shielding factor is the ratio between the unshielded cross section and the self-shielded cross section

$$F_{sh} = \frac{\sigma_m}{\sigma_f} = \frac{\sigma_{E,1}}{\sigma_{E,2/3}} \tag{5.6}$$

Root Mean Square							
	U^{238}		U^{235}		Pu^{239}		Pb^{208}
	rr_c	rr_f	rr_c	rr_f	rr_c	rr_f	rr_c
$\varepsilon_{1,O}$	0.26033	0.26470	0.25016	0.24942	0.25792	0.25616	0.25616
$\varepsilon_{2/3,O}$	0.02354	0.01256	0.03268	0.02766	0.01949	0.03413	0.12281
$\varepsilon_{1,2/3}$	0.51788	0.54749	0.50740	0.49764	0.52923	0.50051	0.50055
$\varepsilon_{2,3}$	0.00012	0.00010	0.00014	0.00012	0.00012	0.00015	0.00012

Table 5.9: Root mean square on microscopic reaction rate for isotopes and reaction type.

where σ_m is the microscopic cross section of medium mesh, and σ_f is the microscopic cross section of fine mesh.

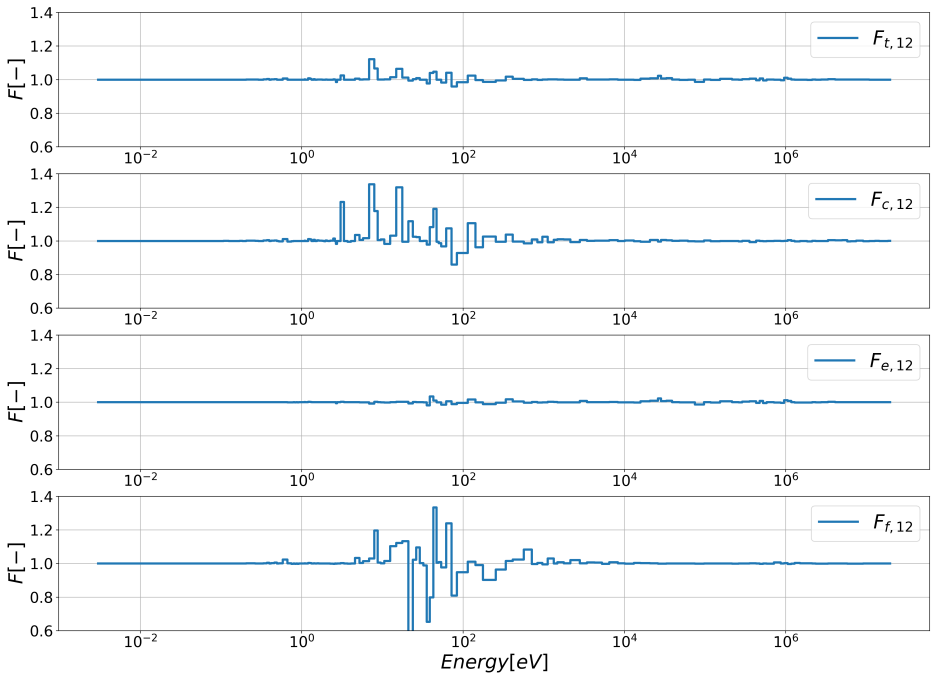

Figure 5.39: Evaluation of auto protection Factor.

The graph shows that the treatment of resonances results in a local reduction of macroscopic cross sections at the resonances, particularly in the epithermal zone, due to the self-protection of the material. This effect results in a self-protection factor less than 1 in the resonant regions and correctly reflects the physics of the problem, confirming the effectiveness of the treatment in reducing the apparent absorption and correctly calculating the reaction cross sections in the presence of narrow resonances.

We have just seen how to derive normalisation, and now we can understand its utility, and start with the possibility to understand the weight of each isotope on the k:

$$W_{i,k} = \frac{\sum_g rr_{i,g,\nu f}}{k} \tag{5.7}$$

where $W_{i,k}$ the weight of isotope i on k_{inf}.

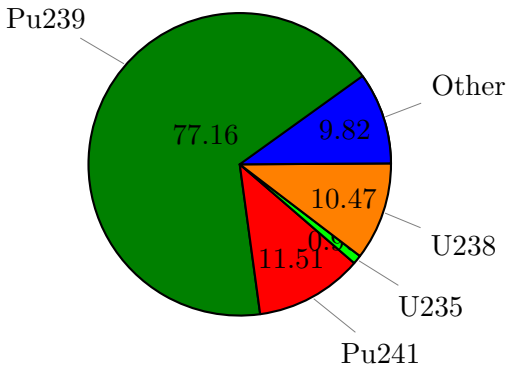

The plot is a comparison of the most important nuclide in term of difference between the calculation ^{239}Pu, and also in term of important of the k.

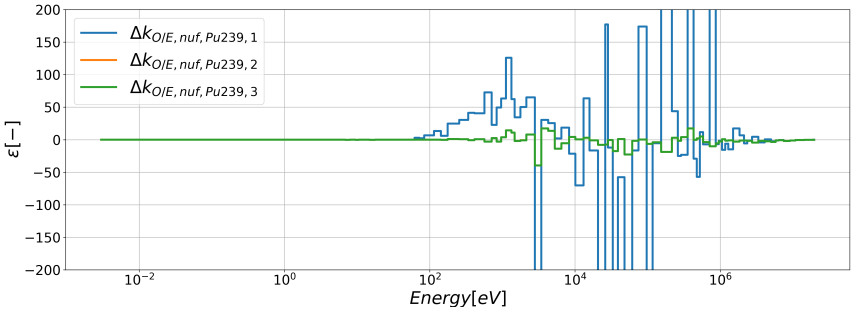

Figure 5.40: Comparison of Δk of ^{239}Pu

Where $\Delta rr_{^{239}Pu} = rr_{^{239}Pu,g,E} - rr_{^{239}Pu,g,O}$ is the difference between ECCO and OpenMC of the macroscopic reaction rate of group **g**.

The plots show the delta k in each groups for the nuclide ^{239}Pu and it shows positive and negative ϵ, that can be associeted to compensation effect.

^{239}Pu	$S_1 - O$	$S_{2-3} - O$
Δrr	295	**-88**

Where $\Delta rr = \sum_g(\Delta rr_{^{239}Pu})$ is the sum of the difference between ECCO and OpenMC for each groups, and the result is same of previous. Now it is possible focus on the second second normalization:

$$W_{i,\rho} = \frac{\sum_g \left(rr_{i,g,t} - rr_{i,g,s}\right)}{\rho} \tag{5.8}$$

where $W_{i,k}$ the weight of isotope i on ρ.

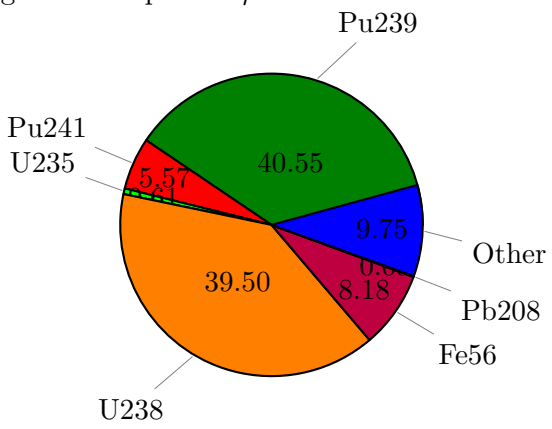

The nuclide ^{238}U was selected because it significantly highlights the transition from a coarse library to a fine one.

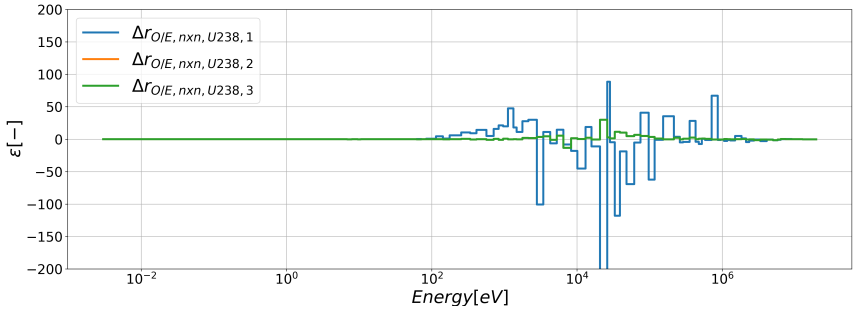

Figure 5.41: Comparison of Δk of ^{238}U

^{239}Pu	$S_1 - O$	$S_{2-3} - O$
Δrr	-247	**-88**

Where $\Delta rr_{^{238}U} = rr_{^{238}U,g,E} - rr_{^{238}U,g,O}$ is the difference between ECCO and OpenMC of the macroscopic reaction rate of group **g**.

The plots show the delta k in each groups for the nuclide ^{238}U and it shows positive and negative ϵ. It possible to notice errors on the 3th step are lower.

At the end of this section is evident that the second step, so going through a step to which has a finer energy mesh for resonant isotopes is critical.

293.6 - 573.6 - 1473.6 K The behavoir of other temperatures is the same and for this reason there is the following table, which summarises the general features and underline

the thermal effect on k_{inf}, which the increasing of the temperatures there is a decreasinf of k_{inf}(**Doppler effect**).

Results	k_1	$k_{2,3}$	OpenMc	$\Delta k_{1,2}$	$\Delta k_{1,O}$	$\Delta k_{2-3,O}$
293.6 K	1.36903	1.36147	1.36432 ± 0.00015	-759 pcm	471 pcm	-285 pcm
573.6K	1.36317	1.35584	1.35840 ±0.00017	-833 pcm	477 pcm	-256 pcm
973.6K	1.35880	1.35166	1.35374 ± 0.00017	-714 pcm	506 pcm	-208 pcm
1473.6K	1.35580	1.34859	1.35060 ± 0.00017	-699 pcm	498 pcm	-201 pcm

Table 5.10: Comparison between of k_{inf} at different step.

5.6 Heterogeneous geometries

The following analysis are very similar because the initial idea is a first step to validate ECCO, and to do its is important have a evaluation on the same parameters. In the following section we will see:

- evaluation of critical factors on 1 group discretization [7];
- calculation on different values of groups(33 ,172),for both of them there will be valuation of errors on:
  - macroscopic cross section;
  - macroscopic reaction rates;
  - microscopic cross section;
  - microscopic reaction rates.

5.6.1 Heterogeneous Pin

The analysis is on a fuel pin of a inner fuel assembly of the ALFRED's core The Hypothesys are:

- *Infinity lattice*, to do a critical analysis;
- Cold configuration, so no dilatation ;
- Consideration of the heterogeneity;
- The library used is the ENDFB-VII.
- the pin-cell is a Hexagonal, with a sudivition of 5 regions 5.5;
- the diameters of pellets and claddings, and composotion of materials are provided by ALFRED's benchmark;

The route used is similar to the Reference route (5 steps) but with a difference:

- The Buckling is imposedd equal to zero, to simulate the infinite lattice;

The buclikng was emposed equal to zero, because OpenMC has not a option already implemented to simulate the leakages.

k_{inf} & Critical factors The first step of benchmarking of ALFRED required the following parameters evalueted on 1G discretization:

	ECCO	OpenMC		Δk
k_{inf}	1.35315	1.35581	± 0.00015	266 pcm
Critical Factors				
	ECCO	OpenMC		Relative Error
η	1.40252	1.40530	0.00105	0.20%
f	0.9623**8**	0.9623**5**	0.00082	3e-03%
Σ_{tr}A	0.30751	0.31191	0.00023	1.41%

Table 5.11: Comparison of critical factors on heterogenous pin.

where η (Neutron reproduction factor) and f (Thermal utilization factor), and Σ_{tr} is transport cross section. For Σ_{tr}A, the relative difference is **1.41%**, which is a larger value than the other factors, attributable to the different approximations in the treatment of anisotropic scattering and transport in deterministic methods compared with Monte Carlo.

Microscopic σ_x		ECCO	OPENMC		$\varepsilon_{E/O}$[%]
Fe^{56}	CAT	0.00818	0.00821	±0.00002	0.41%
Pb^{208}	CAT	0.00067	0.00067	±0.00000	0.43%
	INE	0.02594	0.02637	±0.00001	1.65%
Pu^{239}	FIS	1.72510	1.72503	±0.00112	0.00%
	$\nu \times$ FIS	5.07060	5.07052	±0.00326	0.00%
	CAT	0.44682	0.44630	±0.00152	0.12%
Pu^{241}	FIS	2.39310	2.39572	±0.00333	0.11%
	$\nu \times$ FIS	7.09670	7.10457	±0.00525	0.11%
	CAT	0.40559	0.40796	±0.00432	0.58%
U^{235}	FIS	1.82980	1.83022	±0.00257	0.02%
	$\nu \times$ FIS	4.49230	4.49346	±0.00331	0.03%
	CAT	0.51046	0.51051	±0.00188	0.01%
U^{238}	FIS	0.03663	±0.03677	0.00007	0.36%
	$\nu \times$ FIS	0.09974	0.10014	±0.00011	0.40%
	CAT	0.27093	0.26971	±0.00024	0.45%
	INE	0.96769	0.96880	±0.00661	0.11%

Table 5.12: Comparison of the data required by the ALFRED benchmark**??**

The error on the $\sigma_{Pb,ine}$ is the highest, and the reason might depend on OpenMC inelastic tally.

33G analysis In this section will be the cross section and reaction rate on an energy discretization of 33 groups. Then let's move on the flux :

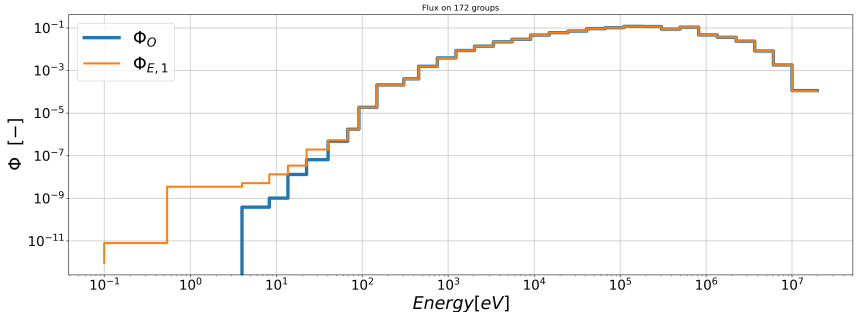

Figure 5.42: Flux on 33 groups of heterogeneous pin.

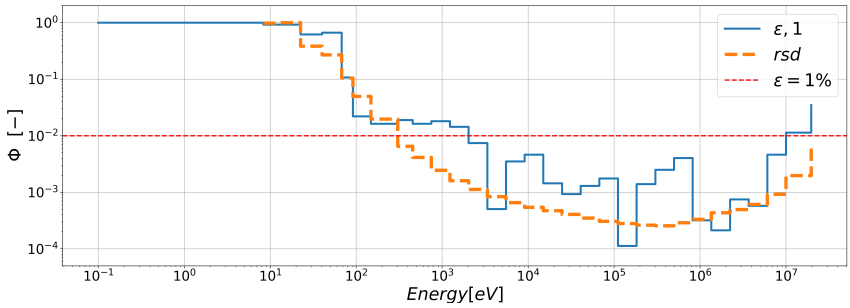

Figure 5.43: Comparison of the flux on 33 groups of heterogeneous pins.

$$RMS_{E/O} = 0.0108 \tag{5.9}$$

this is the RMS on Flux.

Also in this case it is possible notice that the flux of OpenMC is zero at low energy, and is coherent with the physics of problem.

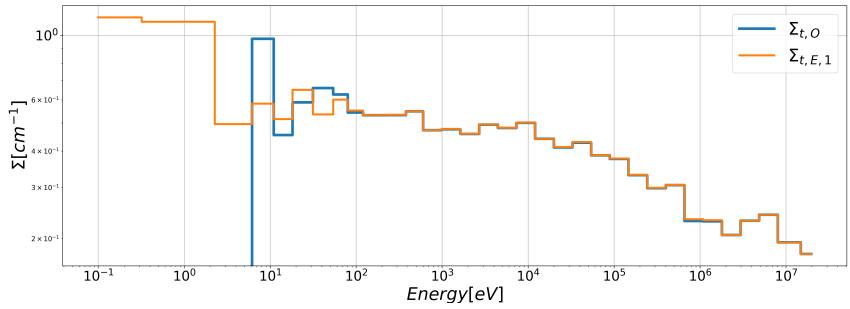

Figure 5.44: Cross-section for total reactions (XS).

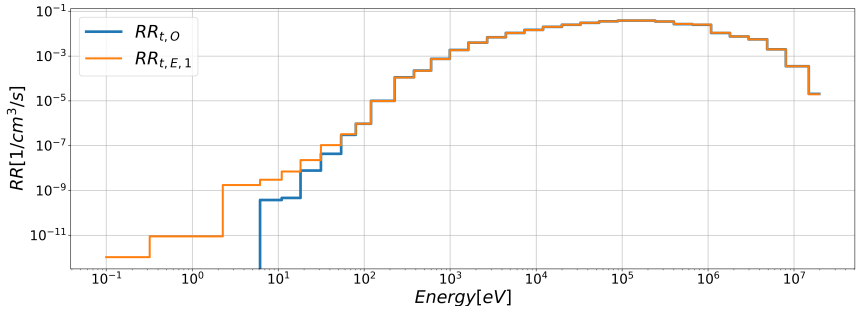

Figure 5.45: Reaction rate for total reactions (RR).

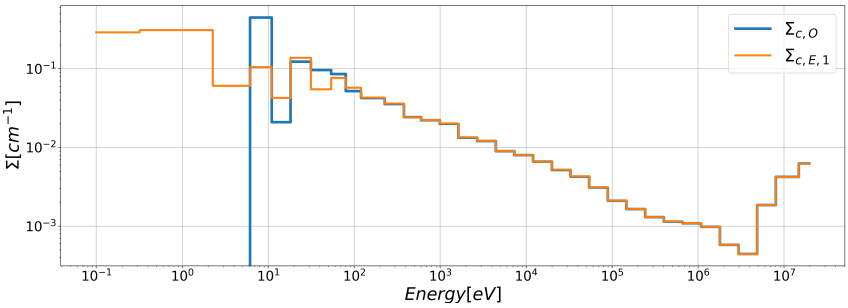

Figure 5.46: Cross-section for capture reactions (XS).

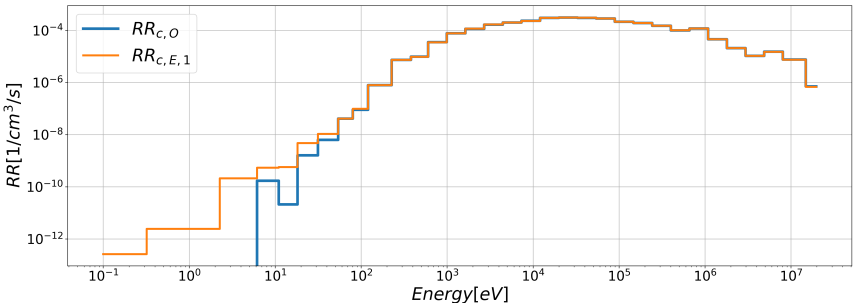

Figure 5.47: Reaction rate for capture reactions (RR).

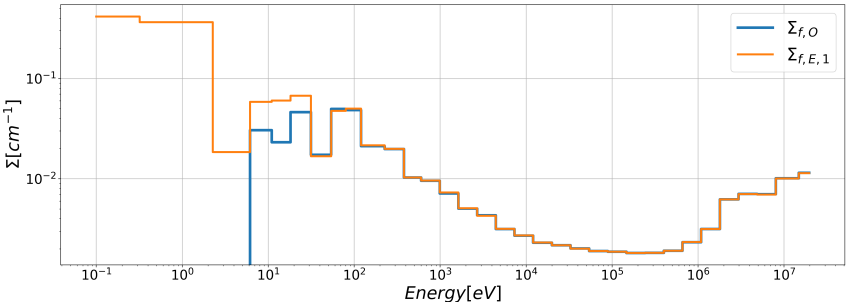

Figure 5.48: Cross-section for fission reactions (XS).

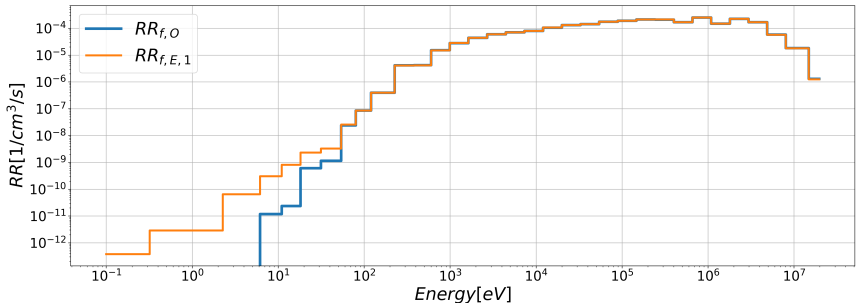

Figure 5.49: Reaction rate for fission reactions (RR).

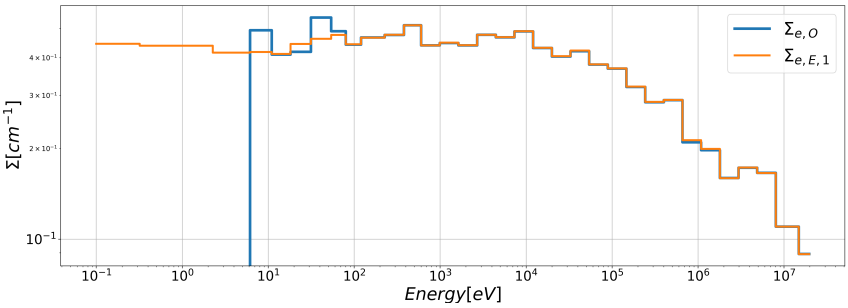

Figure 5.50: Cross-section for elastic reactions (XS).

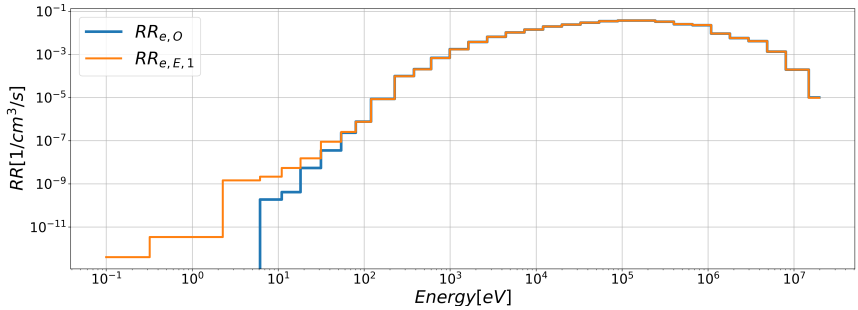

Figure 5.51: Reaction rate for elastic reactions (RR).

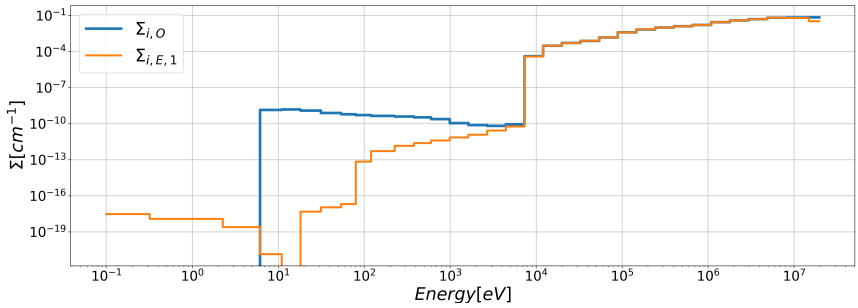

Figure 5.52: Cross-section for inelastic reactions (XS).

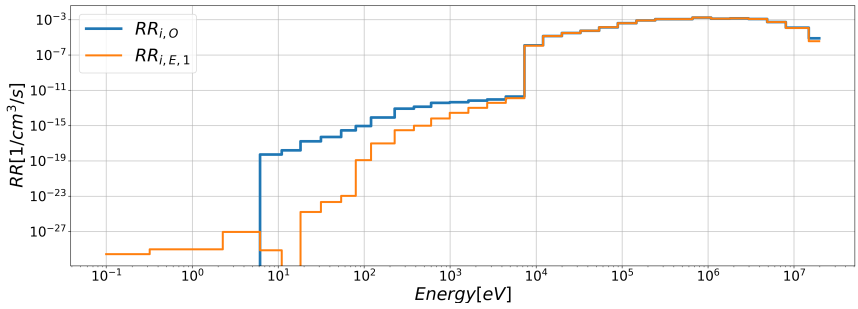

Figure 5.53: Reaction rate for inelastic reactions (RR).

The table above reports the Root Mean Square (RMS) of the Σ_x (macroscopic cross sections) and RR_x (reaction rates) for each reaction type across the 33-group energy structure, allowing a quantitative comparison between ECCO and OpenMC results.

It can be observed that:

$RMS_{E/O}$		
	Σ_x	RR_x
TOTAL	0.00447	0.00540
CAPTURE	0.00976	0.00189
FISSION	0.00431	0.00533
ELASTIC	0.00437	0.00534
INELASTIC	-	0.00534

Table 5.13: Root Mean Square of $Sigma_x$ RR_x of each reaction rate on 33 G

It can be observed that the overall RMS errors for macroscopic cross sections and reaction rates are approximately $0.4\% - 0.5\%$, indicating a good level of agreement between ECCO and OpenMC for total tallies.

No data is reported for the **inelastic** reaction channels in this analysis, as it can be seen from the graph that there is a significant discrepancy between the two curves. Issues

were encountered with the OpenMC tally concerning the inelastic reaction, preventing a reliable comparison B.

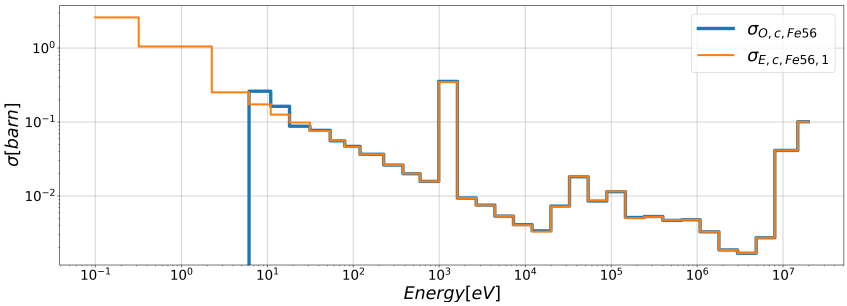

Figure 5.54: Cross-section for Fe-56 capture (XS micro).

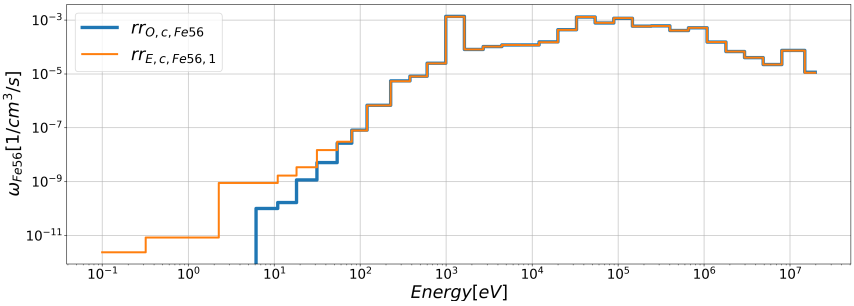

Figure 5.55: Reaction rate for Fe-56 capture (RR micro).

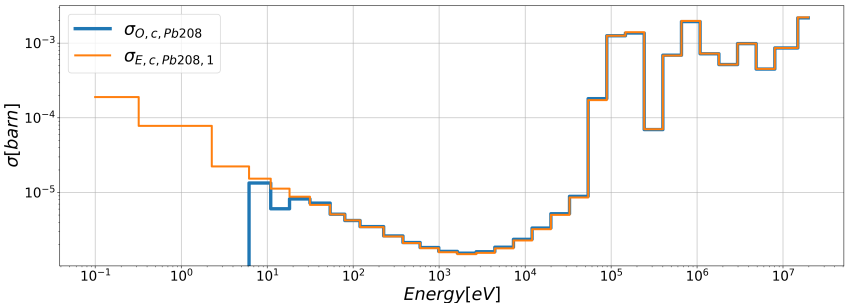

Figure 5.56: Cross-section for Pb-208 capture (XS micro).

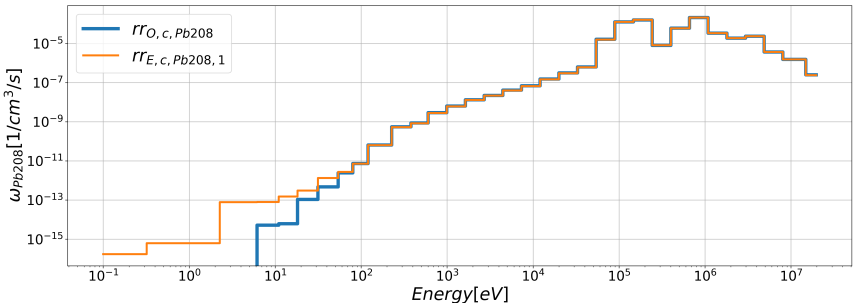

Figure 5.57: Reaction rate for Pb-208 capture (RR micro).

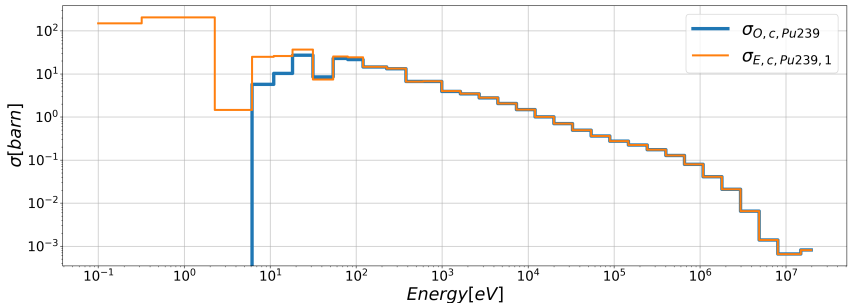

Figure 5.58: Cross-section for Pu-239 capture (XS micro).

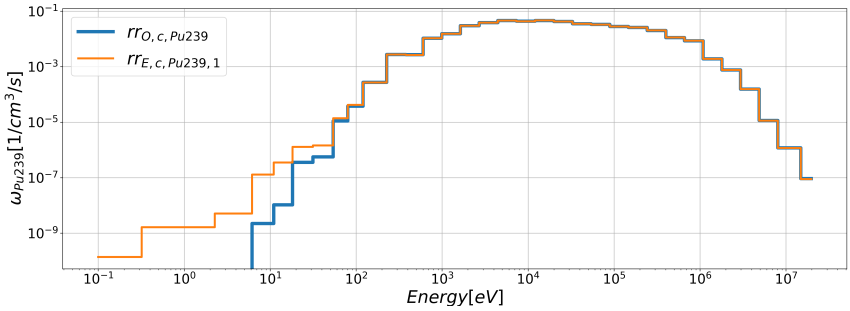

Figure 5.59: Reaction rate for Pu-239 capture (RR micro).

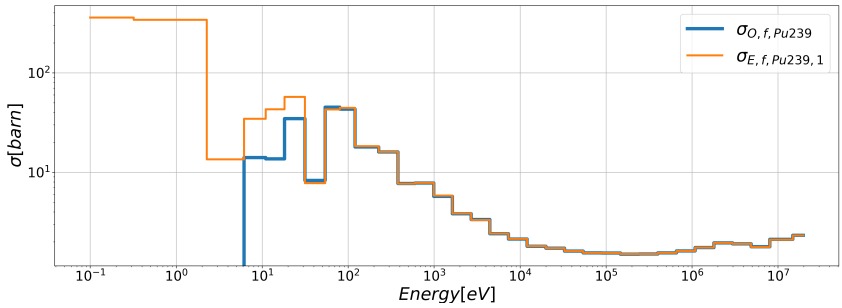

Figure 5.60: Cross-section for Pu-239 fission (XS micro).

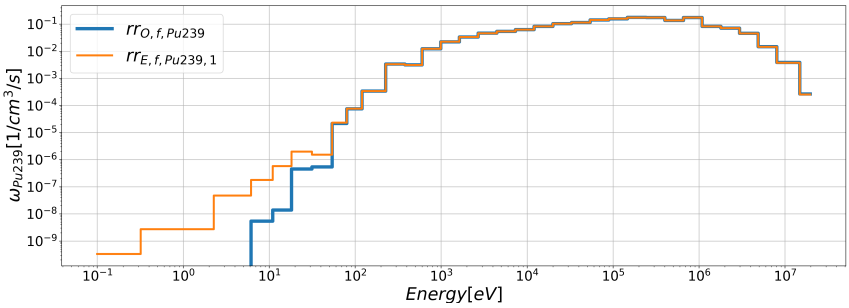

Figure 5.61: Reaction rate for Pu-239 fission (RR micro).

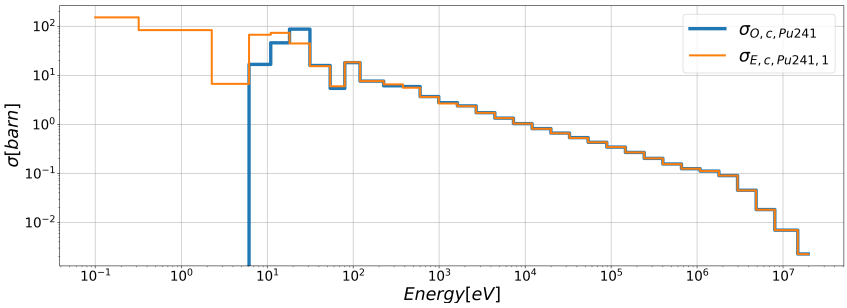

Figure 5.62: Cross-section for Pu-241 capture (XS micro).

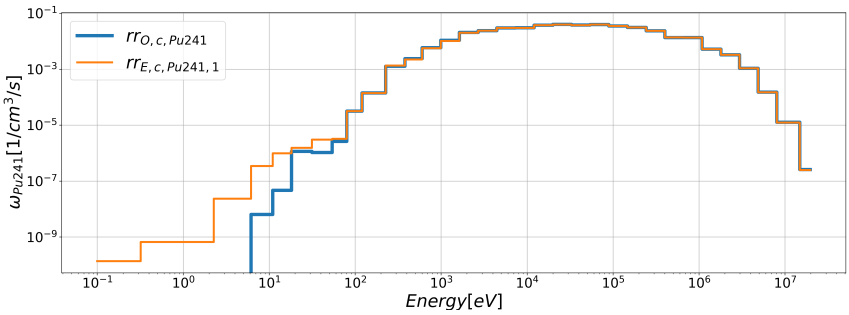

Figure 5.63: Reaction rate for Pu-241 capture (RR micro).

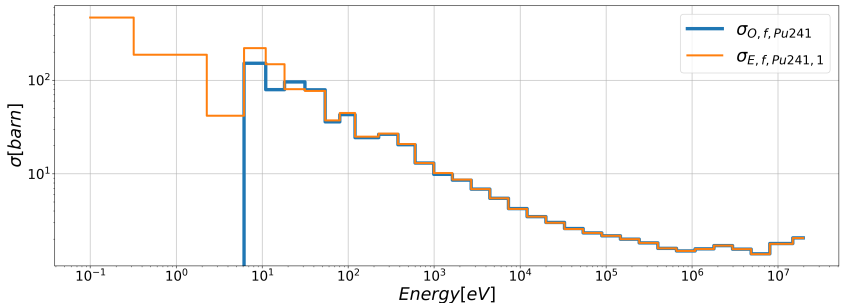

Figure 5.64: Cross-section for Pu-241 fission (XS micro).

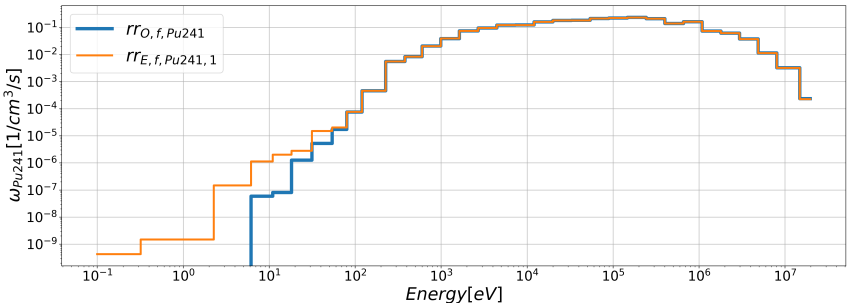

Figure 5.65: Reaction rate for Pu-241 fission (RR micro).

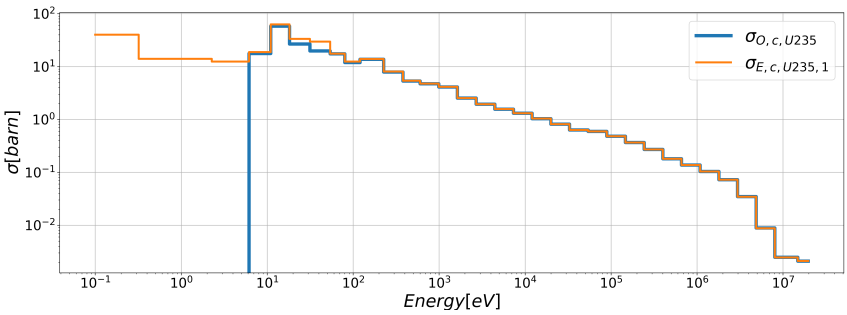

Figure 5.66: Cross-section for U-235 capture (XS micro).

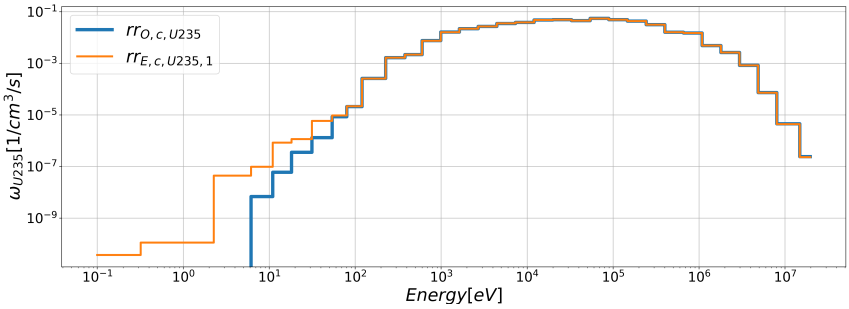

Figure 5.67: Reaction rate for U-235 capture (RR micro).

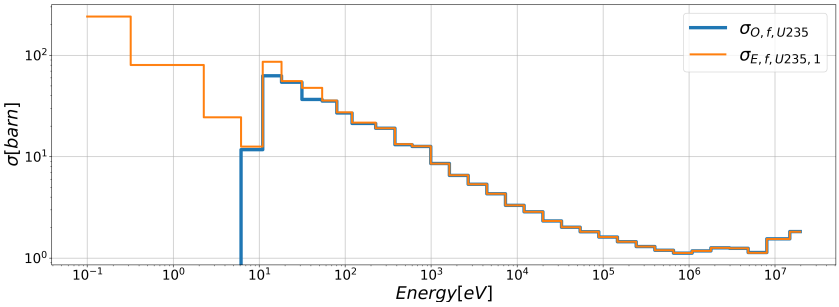

Figure 5.68: Cross-section for U-235 fission (XS micro).

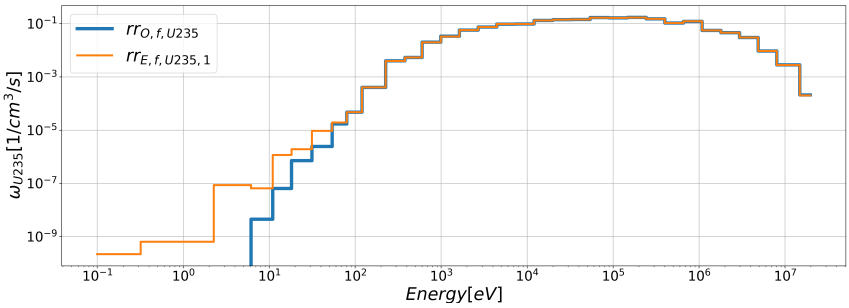

Figure 5.69: Reaction rate for U-235 fission (RR micro).

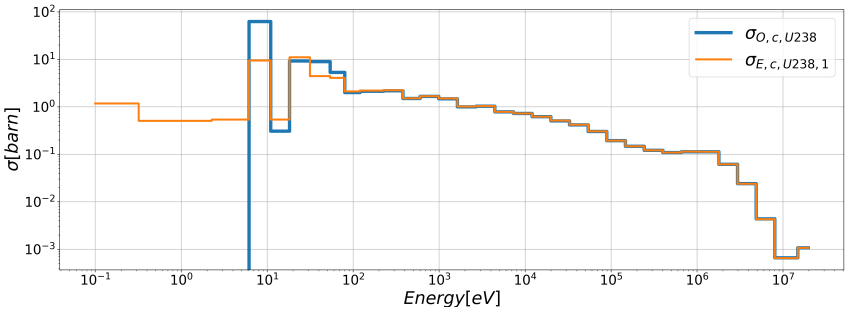

Figure 5.70: Cross-section for U-238 capture (XS micro).

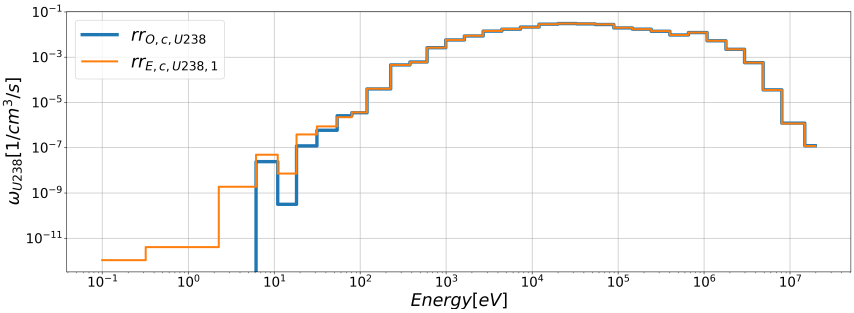

Figure 5.71: Reaction rate for U-238 capture (RR micro).

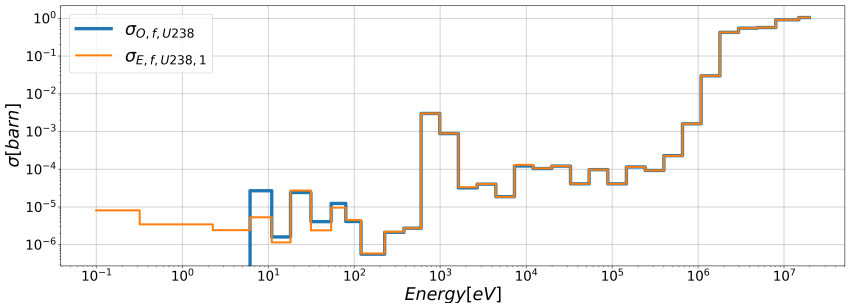

Figure 5.72: Cross-section for U-238 fission (XS micro).

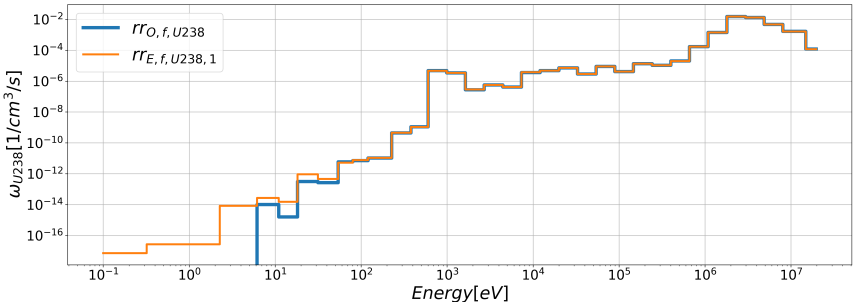

Figure 5.73: Reaction rate for U-238 fission (RR micro).

		$\varepsilon_{E/O}$	
		σ_x	rr_x
Fe^{56}	CAT	0.01590	0.02821
Pb^{208}	CAT	0.05883	0.03390
Pu^{239}	FIS	0.00169	0.01640
	CAT	0.04656	0.02151
Pu^{241}	FIS	0.02479	0.02366
	CAT	0.00020	0.02999
U^{235}	FIS	0.00813	0.02576
	CAT	0.01652	0.02418
U^{238}	FIS	0.00713	0.02289
	CAT	0.02652	0.01330

Table 5.14: Root Mean Square of microscopic cross section and reaction rate far each isotopes.

The RMS values for microscopic cross sections and reaction rates are generally around **1-6%**.

The highest error is the microscopic cross section of capture of Pb^{208}.
The derivation of the normalisation procedure has been presented, allowing for a clear understanding of its utility. This provides the basis for analysing the contribution of each isotope to the effective multiplication factor k and the reactivity.

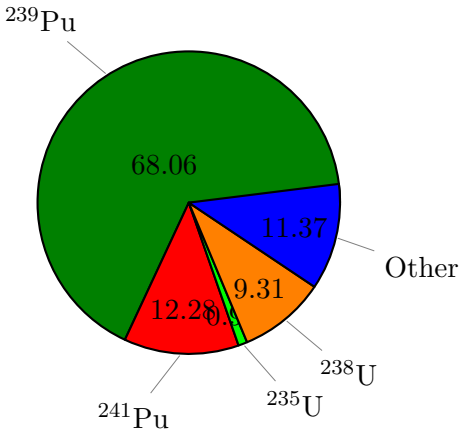

Figure 5.74: Weight of fissionable isotopes with respect the k_{inf}

The plot is a comparison of the most important nuclide in term of difference between the calculation ^{239}Pu, and also in term of important of the k.

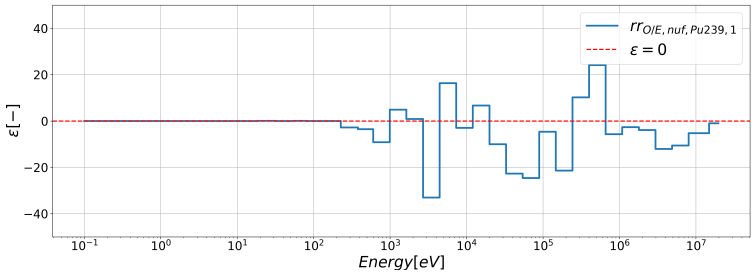

Figure 5.75: Comparison of Δk of ^{239}Pu

Where $\Delta rr_{^{239}Pu} = rr_{^{239}Pu,g,E} - rr_{^{239}Pu,g,O}$ is the difference between ECCO and OpenMC of the macroscopic reaction rate of group **g**.

The 5.75 show the delta k in each groups for the nuclide ^{239}Pu and it shows positive and negative ϵ, that can be associeted to compensation effect.

^{239}Pu	$S_{E/O}$
Δrr	-112

Where $\Delta rr = \sum_g(\Delta rr_{^{239}Pu})$ is the sum of the difference between ECCO and OpenMC for each groups.

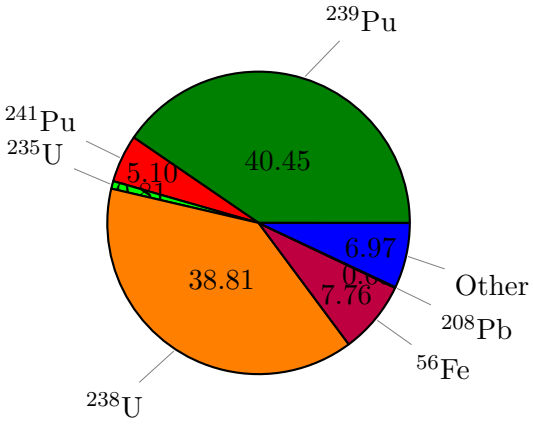

Figure 5.76: Weight of isotopes with respect the ρ

The nuclide ^{238}U was selected because it significantly highlights the transition from a coarse library to a fine one.

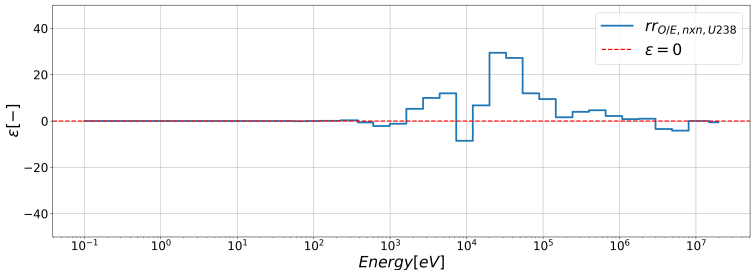

Figure 5.77: Comparison of $\Delta\rho$ of ^{238}U

Where $\Delta rr_{^{238}U} = rr_{^{238}U,g,E} - rr_{^{238}U,g,O}$ is the difference between ECCO and OpenMC of the macroscopic reaction rate of group **g**.

The plots show the delta k in each groups for the nuclide ^{238}U and it shows positive and negative ϵ. It possible to notice errors on the 3th step are lower.

^{238}U	$S_{E/O}$
Δrr	106

Where $\Delta rr = \sum_g(\Delta rr_{^{238}U})$ is the sum of the difference between ECCO and OpenMC for each groups.

172G analysis Having completed the initial comparison and validation on the heterogeneous pin using a 33-group discretization, the analysis is now extended using a finer energy discretization with **172 energy groups**. This will allow a more detailed resolution of the resonance structures, especially in the epithermal and fast regions, improving the consistency of the flux and reaction rate predictions between deterministic and Monte Carlo calculations.

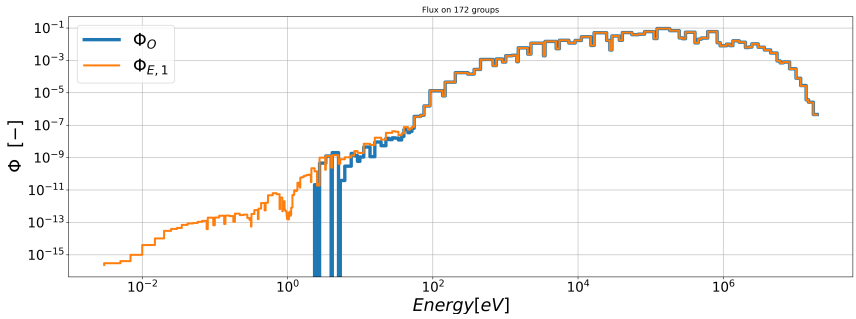

Figure 5.78: Flux on 172 groups of heterogeneous pin.

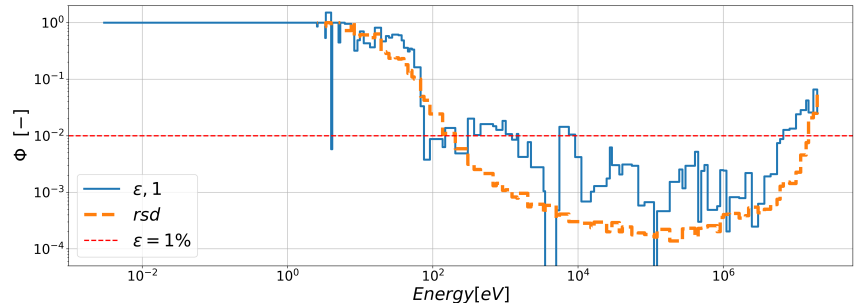

Figure 5.79: Comparison of the flux on 172 groups of heterogeneous pins.

$$RMS_{E/O} = 0.02501 \tag{5.10}$$

this is the RMS on Flux. And if we compare it with the same on 33G we see that the error on 172G is more than the double.

As previously noted, the OpenMC flux approaches zero at low energies, consistent with the fast-spectrum nature of the ALFRED reactor In particular, due to the fast spectrum nature of ALFRED and the absence of a moderator, the thermalization of neutrons is negligible, resulting in a very low flux level in the thermal energy range. This behavior confirms the physical consistency of the OpenMC simulation and provides a valuable reference for evaluating the deterministic ECCO flux treatment in the low-energy region. It is possible to see that the yellow dashed curve(rsd) drops rapidly toward 100eV, as expected, and the values that make statistical sense will be those between about 100 eV and 1circa 2 MeV.

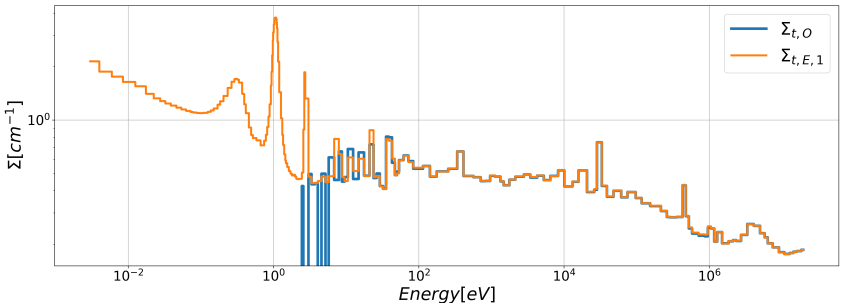

Figure 5.80: Cross-section for total reactions (XS).

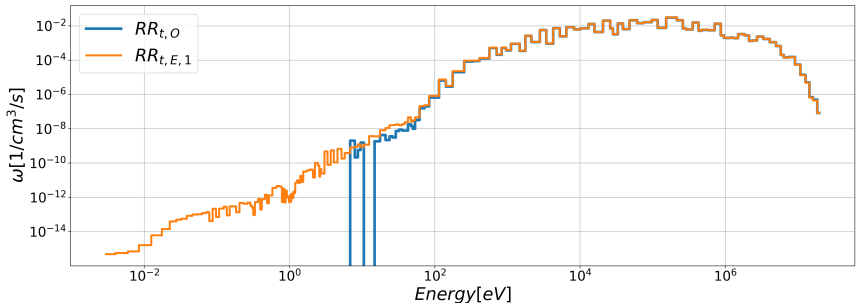

Figure 5.81: Reaction rate for total reactions (RR).

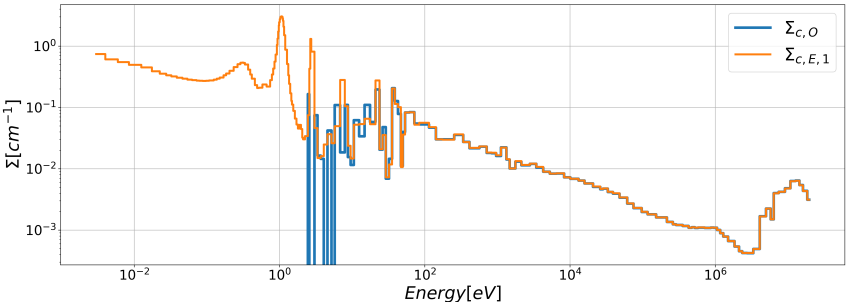

Figure 5.82: Cross-section for capture reactions (XS).

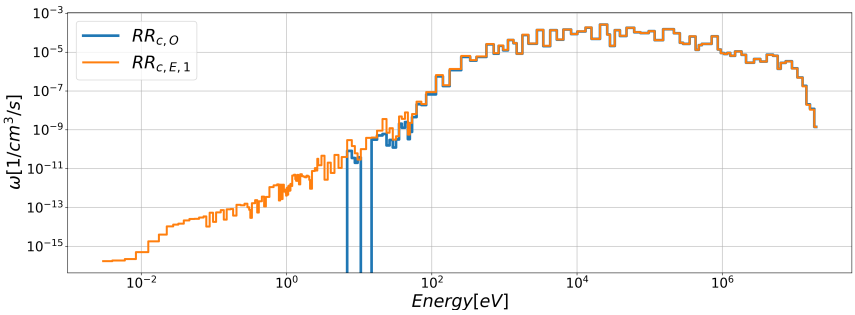

Figure 5.83: Reaction rate for capture reactions (RR).

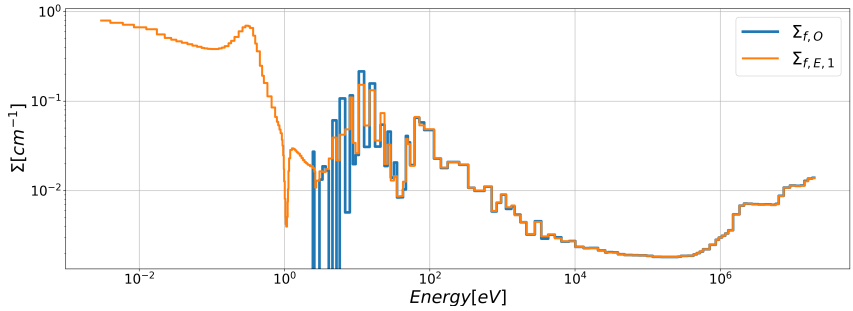

Figure 5.84: Cross-section for fission reactions (XS).

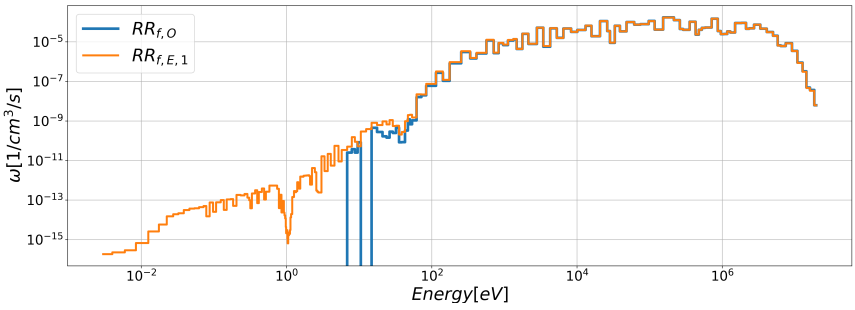

Figure 5.85: Reaction rate for fission reactions (RR).

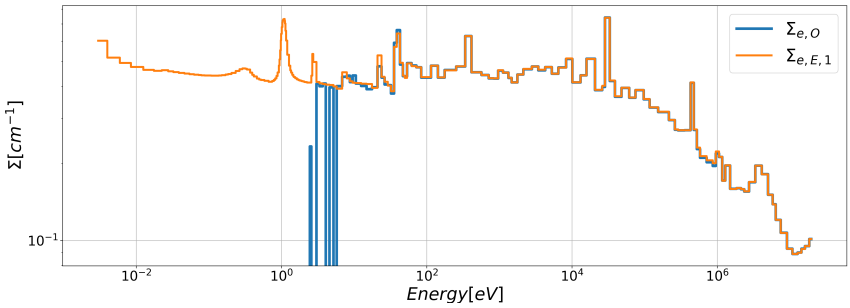

Figure 5.86: Cross-section for elastic reactions (XS).

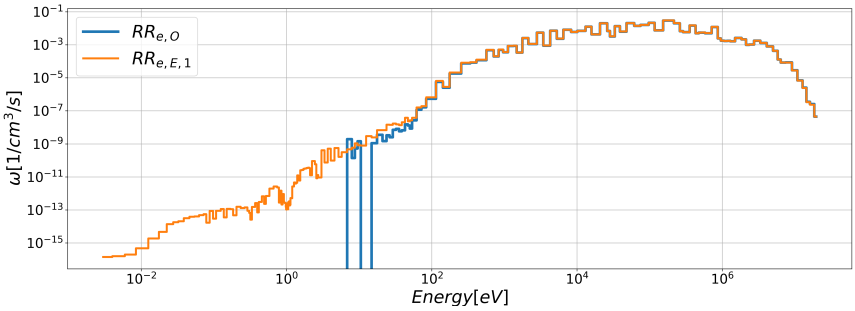

Figure 5.87: Reaction rate for elastic reactions (RR).

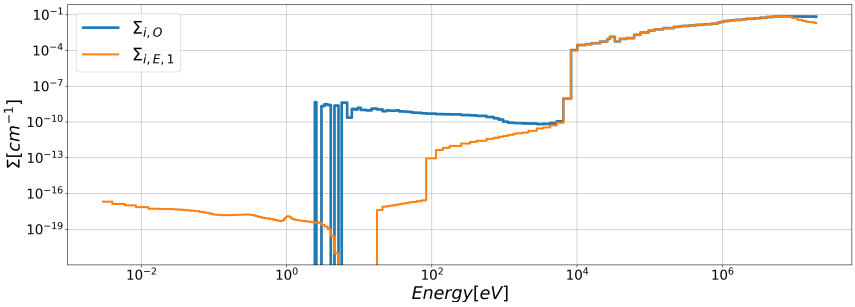

Figure 5.88: Cross-section for inelastic reactions (XS).

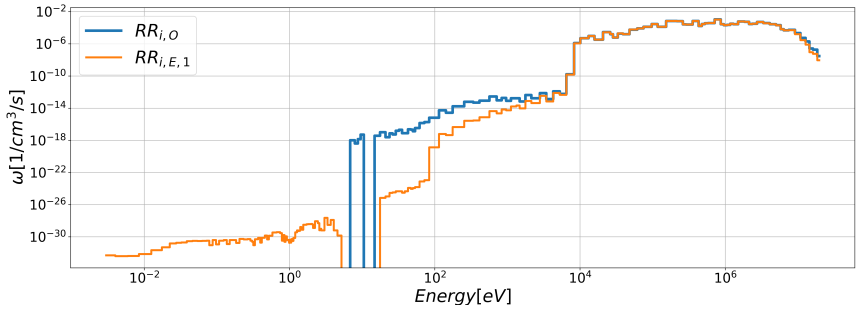

Figure 5.89: Reaction rate for inelastic reactions (RR).

To assess the agreement between ECCO and OpenMC under the refined **172-group discretization**, the following table reports the Root Mean Square (RMS) of the relative differences on the macroscopic cross sections Σ_x and the corresponding reaction rates RR_x for each reaction type.

$RMS_{E/O}$		
	Σ_x	RR_x
TOTAL	0.01910	0.00588
CAPTURE	0.02232	0.02557
FISSION	0.01339	0.01150
ELASTIC	0.01950	0.00547
INELASTIC	-	0.00547

Table 5.15: Root Mean Square of $Sigma_x$ RR_x of each reaction rate on 172 G

Also for these macroscopic cross section and reaction rate, the root mean square is highest on 172G then 33G.

The RMS values on macroscopic cross sections (Σ_x) are in the range of **1% to2.5%**, with the highest discrepancy observed in the **capture reaction rate (2.2%)**.

As 5.88 shows, there is an 'obvious discrepancy between the cross sections that results in an RMS much higher than 1.As much as the error on RR_i agrees with the others it is less reliable.

Following the macroscopic analysis, the comparison between ECCO and OpenMC is now extended to the **microscopic cross sections** and the corresponding **microscopic reaction rates** for the key isotopes within the heterogeneous pin using the **172-group discretization**.

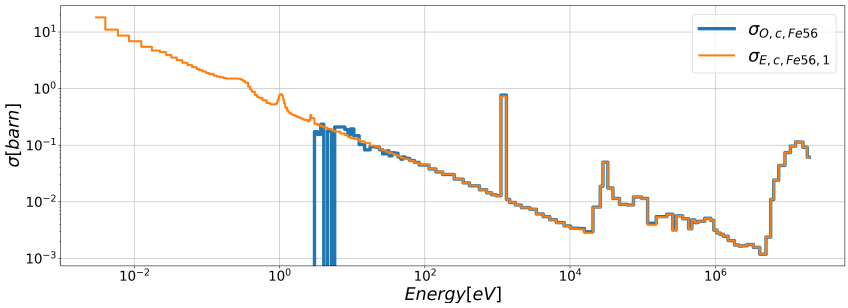

Figure 5.90: Cross-section for Fe56 capture (XS micro).

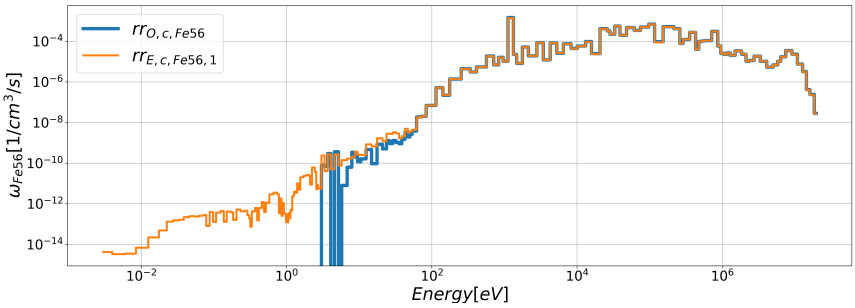

Figure 5.91: Reaction Rate for Fe56 capture (rr micro).

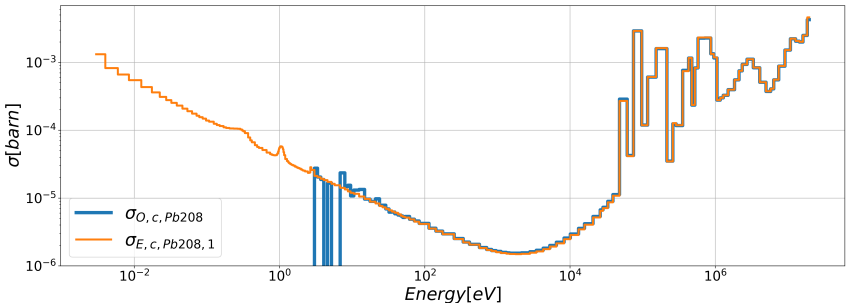

Figure 5.92: Cross-section for Pb208 capture (XS micro).

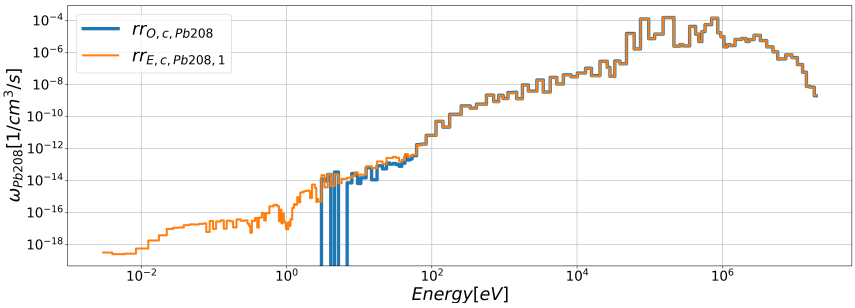

Figure 5.93: Reaction Rate for Pb208 capture (rr micro).

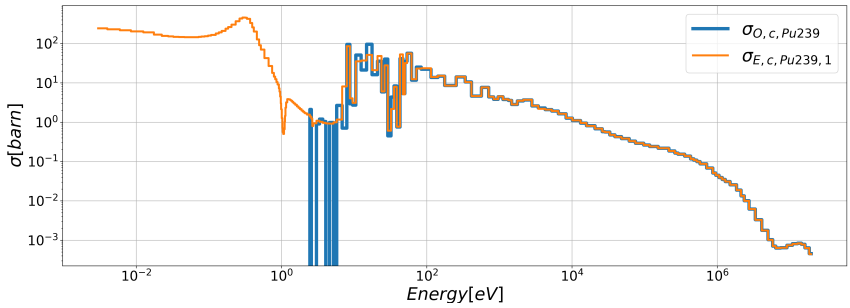

Figure 5.94: Cross-section for Pu239 capture (XS micro).

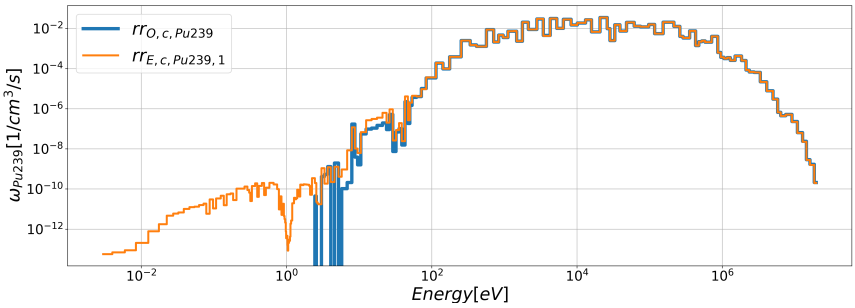

Figure 5.95: Reaction Rate for Pu239 capture (XS micro).

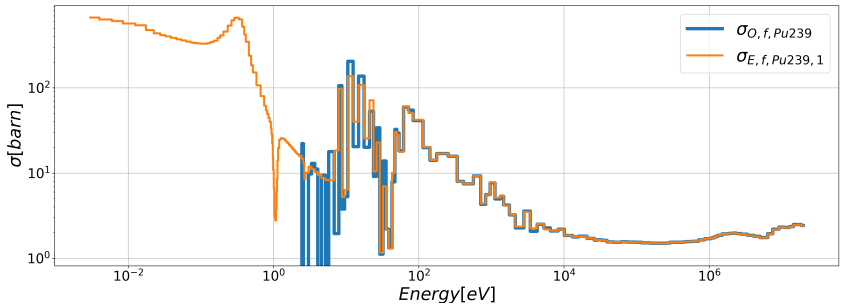

Figure 5.96: Cross-section for Pu239 fission (XS micro).

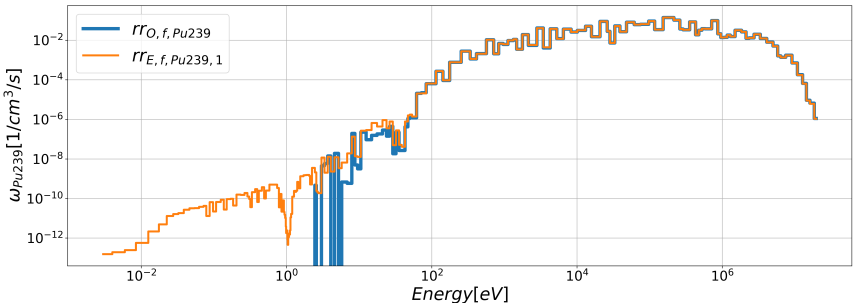

Figure 5.97: Reaction Rate for Pu239 fission (XS micro).

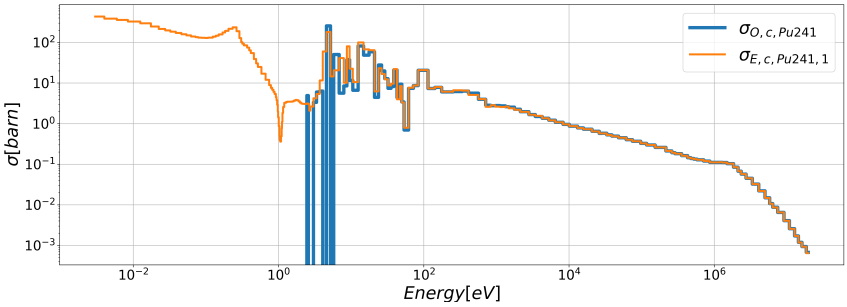

Figure 5.98: Cross-section for Pu241 capture (XS micro).

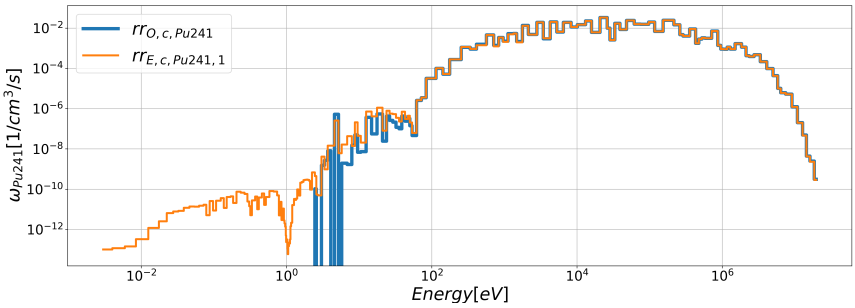

Figure 5.99: Reaction Rate for Pu241 capture (XS micro).

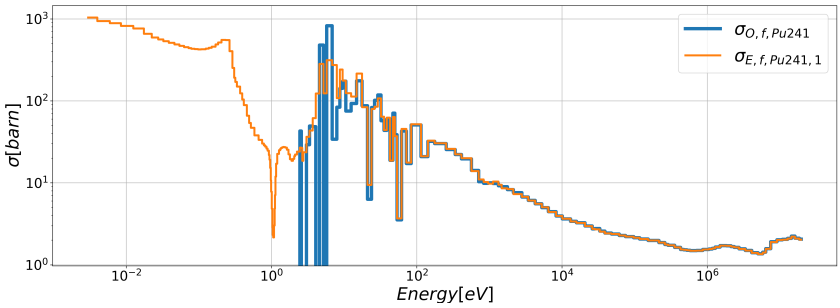

Figure 5.100: Cross-section for Pu241 fission (XS micro).

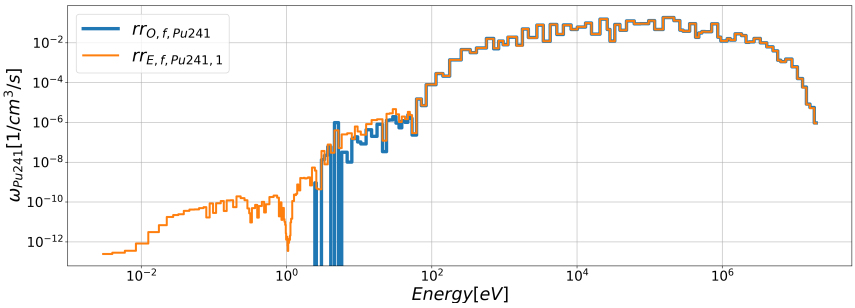

Figure 5.101: Reaction Rate for Pu241 fission (XS micro).

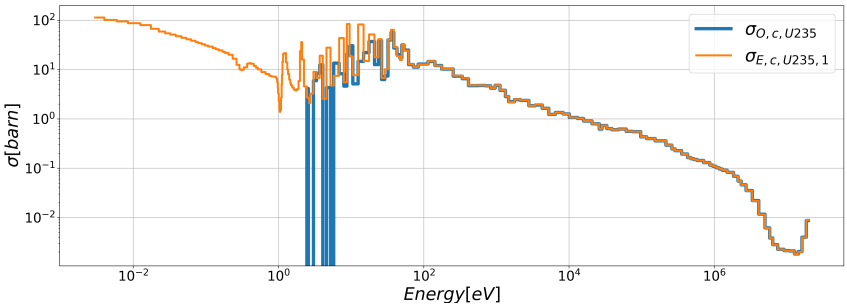

Figure 5.102: Cross-section for U235 capture (XS micro).

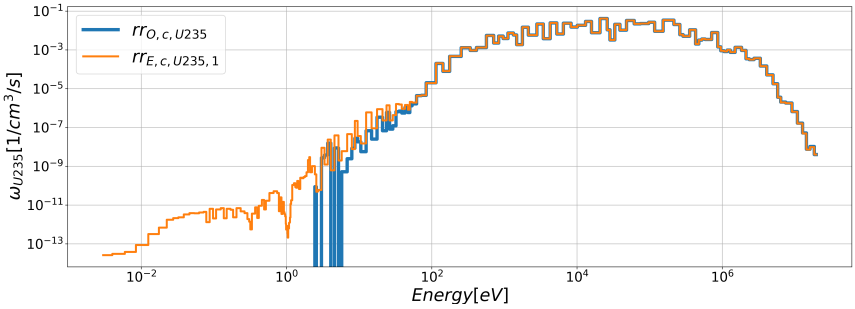

Figure 5.103: Reaction Rate for U235 capture (XS micro).

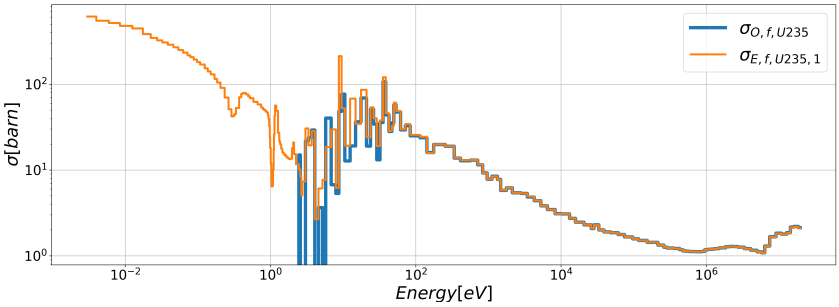

Figure 5.104: Cross-section for U235 fission (XS micro).

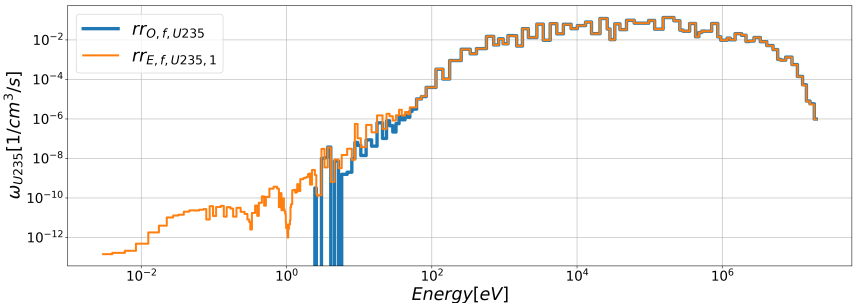

Figure 5.105: Reaction Rate for U235 fission (XS micro).

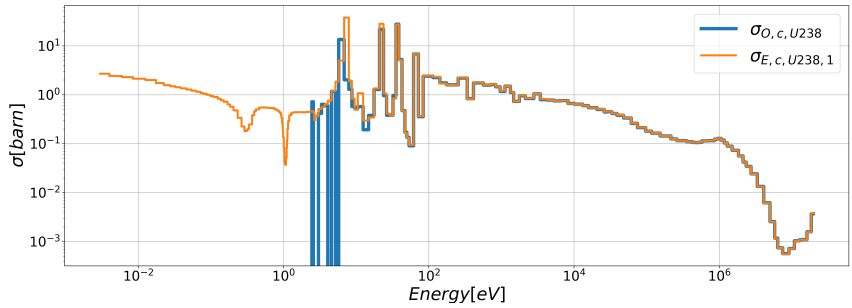

Figure 5.106: Cross-section for U238 capture (XS micro).

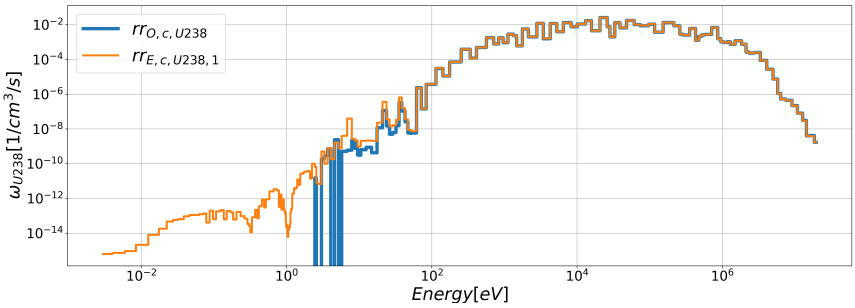

Figure 5.107: Reaction Rate for U238 capture (XS micro).

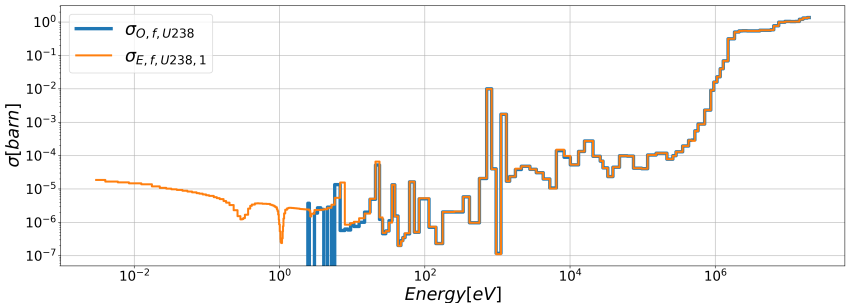

Figure 5.108: Cross-section for U238 fission (XS micro).

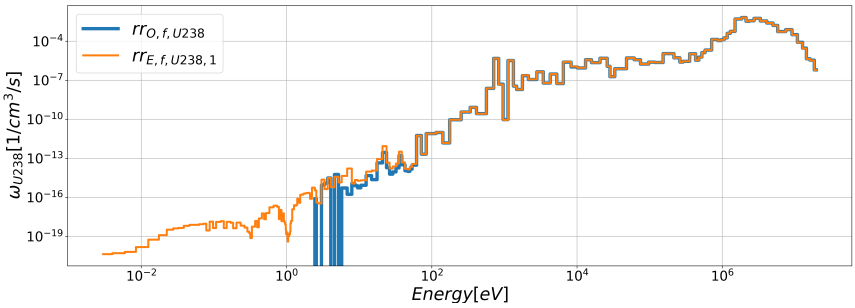

Figure 5.109: Reaction Rate for U238 fission (XS micro).

The table below reports the relative error $\varepsilon_{E/O}$ between ECCO and OpenMC for each isotope and reaction type.

		$\varepsilon_{E/O}$	
		σ_x	rr_x
Fe^{56}	CAT	0.04248	0.07264
Pb^{208}	CAT	0.09051	0.12082
Pu^{239}	FIS	0.01580	0.0142
	CAT	0.00272	0.02741
Pu^{241}	FIS	0.00551	0.01422
	CAT	0.04613	0.07671
U^{235}	FIS	0.00262	0.02755
	CAT	0.00624	0.02382
U^{238}	FIS	0.01378	0.01629
	CAT	0.02110	0.00892

Table 5.16: Root Mean Square of microscopic cross section and reaction rate far each isotopes.

The relative errors on the microscopic cross sections are consistently in the range of **0.5% to 9%** across all isotopes and reaction types, while the relative errors on the microscopic reaction rates are in the range of **0.1% to 12%**, and also in this case the higher error is on the Pb^{208}.

Figure 5.110 shows the distribution of the main nuclides in the system, highlighting that ^{239}**Pu** is the most important contributor both in terms of k.

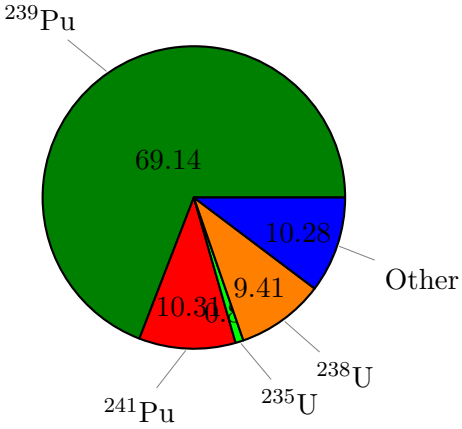

Figure 5.110: Nuclide composition relevant to reactivity.

The plot in Figure 5.111 presents the group-wise Δk for ^{239}**Pu**, where:

$$\Delta rr_{^{239}\mathrm{Pu},g} = rr_{^{239}\mathrm{Pu},g,E} - rr_{^{239}\mathrm{Pu},g,O}$$

represents the difference in the macroscopic reaction rates between ECCO (E) and OpenMC

(O) for group g.

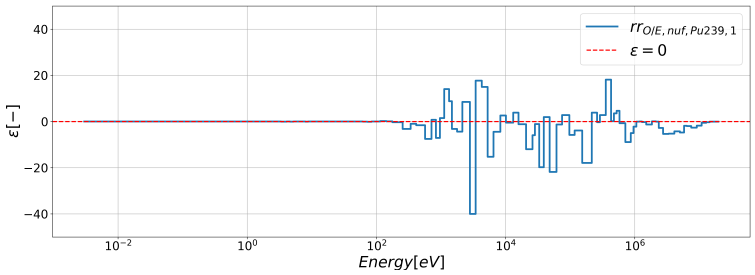

Figure 5.111: Group-wise Δk comparison for ^{239}Pu.

The figure reveals both positive and negative contributions across energy groups, indicative of **compensation effects** where discrepancies in some groups are balanced by opposite differences in others, maintaining consistency in the integrated reactivity.

The integrated differences are summarized in Table 5.17, showing the cumulative sum:

$$\Delta rr = \sum_{g} \Delta rr_{^{239}\mathrm{Pu},g},$$

which quantifies the total difference in macroscopic reaction rates for ^{239}Pu across the groups.

^{239}Pu	$S_{E/O}$
Δrr	**-117 pcm**

Table 5.17: Integrated Δrr for ^{239}Pu across refinement steps.

A similar analysis is performed for ^{238}**U**, shown in Figure 5.112 making it an excellent case to highlight the effects of each isotope with respect the reactivity.

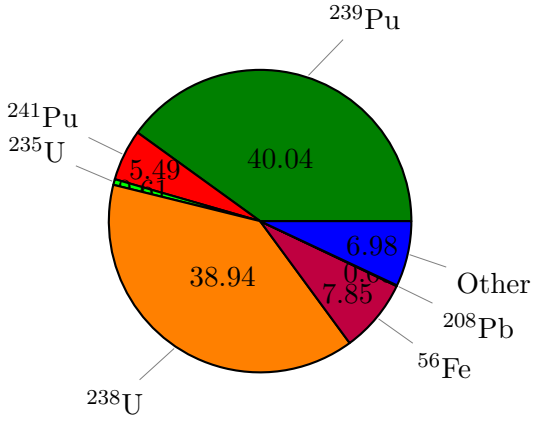

Figure 5.112: Nuclide composition highlighting the relevance of ^{238}U.

The corresponding group-wise $\Delta\rho$ for ^{238}U is presented in Figure 5.113:

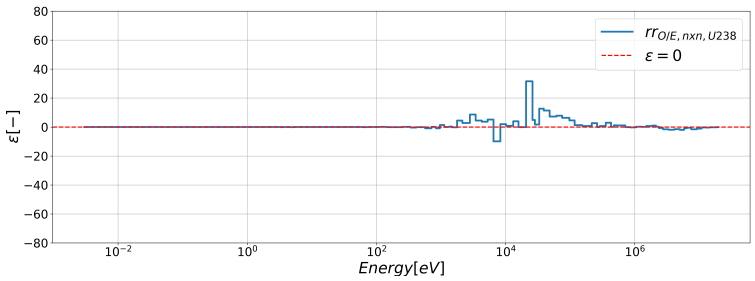

Figure 5.113: Group-wise $\Delta\rho$ comparison for ^{238}U.

Here,

$$\Delta rr_{^{238}\mathrm{U},g} = rr_{^{238}\mathrm{U},g,E} - rr_{^{238}\mathrm{U},g,O}$$

represents the difference in the macroscopic reaction rates for each group.

The plots show positive and negative contributions across the groups, indicative of compensation effects. This confirms the importance of fine-group treatment for isotopes like ^{238}U, where resonance capture and scattering significantly influence reactivity and flux distribution in fast reactor systems.

^{238}U	E - O
Δrr	**117**

Table 5.18: Integrated Δrr for ^{238}U across refinement steps.

5.6.2 Heterogeneous Assembly

The analysis is on a fuel pin of a inner fuel assembly of the ALFRED's core The Hypothesys are:

- *Infinity lattice*, to do a critical analysis;
- Cold configuration, so no dilatation ;
- Consideration of the heterogeneity;
- The library used is the ENDFB-VII.
- the assembly-cell is a Hexagonal, with a subdivision in 7 rings 5.6;
- all pins are fuel pin and except in the center because there is a void-pin ;
- the diameters of pellets and claddings, and composition of materials are provided by ALFRED' s benchmark;

Discretization of Assembly If we see the structure of the assembly, it is possible identify 3 different inner fuel pin, because they are identical under geometrical parameter and materials, but they have different "neighbors":

- from second to fifth ring, each pin is surrounded by other 6 pin;
- each pin of first ring has one neighbor that is a void pin;
- on the sixth ring they are surrounded only by the inner side, while outwardly they see the cladding of the assembly.

This is the reason of this step before of whole analysis of assembly. I made two model in ECCO of assembly:

1. the first has 2 types of pin, the void and mox(i will refer as 2R);
2. the second has 7 types of pin (7R), I had to create 6 different mox pins computationally but not compositionally, because otherwise the same pin cannot be associated with different rings.;

Here are the codes of the two models compared:

```
! 2 region code
CELL 'ASS_INN'
  COMPOSITION_ORDER 'MOX' 'CLAD' 'COOL' 'COOL_EXT' 'VOID' 'COOL2'
   GEOMETRY DATA
    HEX (N_HEX_REG) !3 regions
    (L_int_wrap)          ! PRIMA REGIONE
      HEXLAT                ! NELLA PRIMA REGIONE ABBIAMO IL LATTICE
       !(N_conc_layers) (pitch_lattice) (N_HEX_REG_LAT)
       7              1.36             2
         CYLINDRICAL 2
           (r_clad_void_in)  REGION 1 'VOID'    COMP 5 (T_ref)
           (r_clad_void_ot)  REGION 2 'CLAD'    COMP 2 (T_ref)
           IN                REGION 3 'COOL'    COMP 3 (T_ref)
         CYLINDRICAL 2
           (r_in_clad)      REGION 4 'MOX'      COMP 1 (T_ref)
           (r_ot_clad)      REGION 5 'CLAD'     COMP 2 (T_ref)
           IN               REGION 6 'COOL'     COMP 3 (T_ref)
         1 2 2 2 2 2 2
      IN                   REGION 7 'COOL2'      COMP 6 (T_ref)

   (L_ext_wrap)            REGION 8 'CLAD'       COMP 2 (T_ref) ! SECONDA REG
   (L_ext_hex)             REGION 9 'COOL_EXT'   COMP 4 (T_ref) ! TERZA REG
    REFLECTION
  END OF GEOMETRY DATA
  ;
```

```
! 7 region code
  CELL 'ASS_INN'
     COMPOSITION_ORDER 'MOX' 'CLAD' 'COOL' 'COOL_EXT' 'VOID' 'COOL2'
      GEOMETRY DATA
       HEX (N_HEX_REG) !3 regions
       (L_int_wrap)          ! PRIMA REGIONE
         HEXLAT                ! NELLA PRIMA REGIONE ABBIAMO IL LATTICE
          !(N_conc_layers) (pitch_lattice) (N_HEX_REG_LAT)
          7              1.36             7
            CYLINDRICAL 2
              (r_clad_void_in)  REGION 1 'VOID'    COMP 5 (T_ref)
              (r_clad_void_ot)  REGION 2 'CLAD'    COMP 2 (T_ref)
              IN                REGION 3 'COOL'    COMP 3 (T_ref)
            CYLINDRICAL 2
              (r_in_clad)      REGION 4 'MOX'      COMP 1 (T_ref)
              (r_ot_clad)      REGION 5 'CLAD'     COMP 2 (T_ref)
              IN               REGION 6 'COOL'     COMP 3 (T_ref)
            CYLINDRICAL 2
              (r_in_clad)      REGION 7 'MOX'      COMP 1 (T_ref)
              (r_ot_clad)      REGION 8 'CLAD'     COMP 2 (T_ref)
              IN               REGION 9 'COOL'     COMP 3 (T_ref)
            CYLINDRICAL 2
              (r_in_clad)      REGION 10 'MOX'      COMP 1 (T_ref)
              (r_ot_clad)      REGION 11 'CLAD'     COMP 2 (T_ref)
              IN               REGION 12 'COOL'     COMP 3 (T_ref)
            CYLINDRICAL 2
              (r_in_clad)      REGION 13 'MOX'      COMP 1 (T_ref)
              (r_ot_clad)      REGION 14 'CLAD'     COMP 2 (T_ref)
              IN               REGION 15 'COOL'     COMP 3 (T_ref)
            CYLINDRICAL 2
              (r_in_clad)      REGION 16 'MOX'      COMP 1 (T_ref)
              (r_ot_clad)      REGION 17 'CLAD'     COMP 2 (T_ref)
              IN               REGION 18 'COOL'     COMP 3 (T_ref)
            CYLINDRICAL 2
              (r_in_clad)      REGION 19 'MOX'      COMP 1 (T_ref)
              (r_ot_clad)      REGION 20 'CLAD'     COMP 2 (T_ref)
              IN               REGION 21 'COOL'     COMP 3 (T_ref)
            1 2 3 4 5 6 7
          IN                  REGION 22 'COOL2'      COMP 6 (T_ref)

       (L_ext_wrap)           REGION 23 'CLAD'       COMP 2 (T_ref) ! SECONDA REG
       (L_ext_hex)            REGION 24 'COOL_EXT'   COMP 4 (T_ref) ! TERZA REG
       REFLECTION
     END OF GEOMETRY DATA      ;
```

	2R	7R	OpenMC		Δk_{2R}	Δk_{7R}
k_{inf}	1.28462	1.28584	1.28690	± 0,00013	228	106

Table 5.19: Comparison on k_{inf} with respect the discretization.

Σ_x			
	2R	7R	OpenMC
TOTAL	0.347225	0.347179	0.346171
CAPTURE	0.00272546	0.00272441	0.00271668
FISSION	0.00212837	0.00213089	0.00212716
ELASTIC	0.333318	0.353418	0.332281

Table 5.20: Comparison on Σ_x with respect the discretization.

The most impactful figure is definitely the k_{inf} in that thanks to discretization it could be shortened by about 100 pcm compared to that of OpenMC. In addition, the macroscopic cross sections of the 7R model are also closer. We can infer that as expected creating a better discretization without losing in computation time, both are performed in a couple of minutes, reflects a better result and that is why the following analyses were performed only with **7R**.

k_{inf} & Critical factors As for the pin, let's start again with the first step of benchmarking of ALFRED, which required the following parameters evaluated on 1G discretization:

	ECCO	OpenMC		Δk
k_{inf}	1.28584	1.28690	± 0,00013	106
Critical Factors				
	P1 Con	OpenMC		ε
$\backslash\eta$	1,35873	1,31140	± 0,00024	3,61%
f	0,94112	0,97900	± 0,00020	3,87%
Σ_{tr}	0,30865	0,31892	± 0,00022	3,22%

Table 5.21: Critical factor analysis on heterogeneous assembly.

The comparison shows a very small discrepancy of **106 pcm** on k_{inf}. The relative errors on the critical factors (η, f, Σ_{tr}) ,A, remain within 3-4%.

To deepen the analysis, the microscopic cross sections and reaction rates for key isotopes have also been compared, as reported below.

Microscopic σ_x		ECCO	OPENMC		$\varepsilon_{E/O}$
Fe^{56}	CAT	8.2458E-03	8.2908E-03	± 5E-06	0.544
Pb^{208}	CAT	6.6676E-04	6.6465E-04	± 3E-07	0.318
	INE	2.2495E-02	2.2865E-02	±4E-07	1.618
Pu^{239}	FIS	1.7631	1.7609	±4E-04	0.148
	$\nu \times$ FIS	5.1767	5.1690	±3E-03	0.149
	CAT	4.9439E-01	4.93136E-01	±5E-04	0.254
Pu^{241}	FIS	2.4882	2.4874	±8E-07	0.044
	$\nu \times$ FIS	7.3743	7.3709	±5E-03	0.046
	CAT	4.3411E-01	4.36464E-01	± 8E-04	0.539
U^{235}	FIS	1.9060	1.9046	±6E-07	0.099
	$\nu \times$ FIS	4.6763	4.6715	±3E-03	0.103
	CAT	5.4551E-01	5.4480E-01	± 7E-04	0.130
U^{238}	FIS	3.3850E-02	3.3617E-02	±1E-05	0.692
	$\nu \times$ FIS	9.2103E-02	9.1468E-02	±1E-04	0.770
	CAT	2.8537E-01	2.8422E-01	± 8E-05	0.405
	INE	9.4350E-01	9.4862E-01	±7E-03	0.540

Table 5.22: Comparison of the data required by the ALFRED benchmark**??**

The results show a generally good agreement between ECCO and OpenMC across the isotopes and reactions analyzed, with relative errors typically below 1%. However, it is noted that the **largest discrepancy occurs for the inelastic cross section of** Pb^{208}, where the relative error reaches 1.62%. This behavior is consistent with the sensitivity of lead's inelastic scattering treatment under a 1G discretization and indicates an area where further refinement or detailed energy treatment may be beneficial in future studies.

33G analysis In this section, the flux spectra obtained using the **33-group discretization** are analyzed, providing a visual and quantitative comparison between ECCO and OpenMC for the heterogeneous pin-cell configuration.

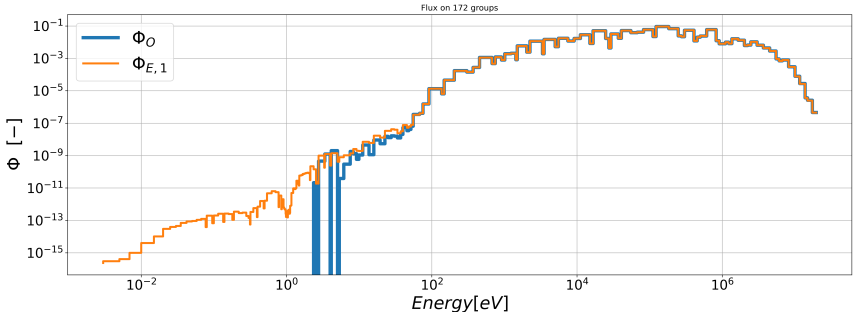

Figure 5.114: Flux on 172 groups of heterogeneous pin.

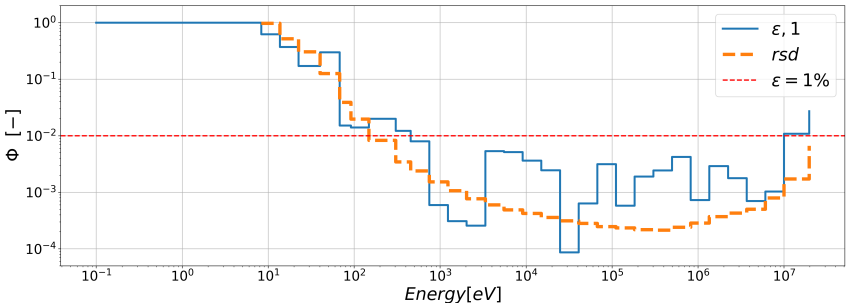

Figure 5.115: Comparison of the flux on 172 groups of heterogeneous pins.

$$RMS_{E/O} = 0.0015 \tag{5.11}$$

which corresponds to a relative difference of approximately **0.1%** on average across all groups.

It can also be observed that, as expected, the **OpenMC flux approaches zero in the low-energy groups**. This behavior is physically consistent with the characteristics of the system under investigation, as ALFRED operates as a fast-spectrum reactor with no moderator, resulting in negligible thermalization of neutrons and a suppressed flux at thermal energies.

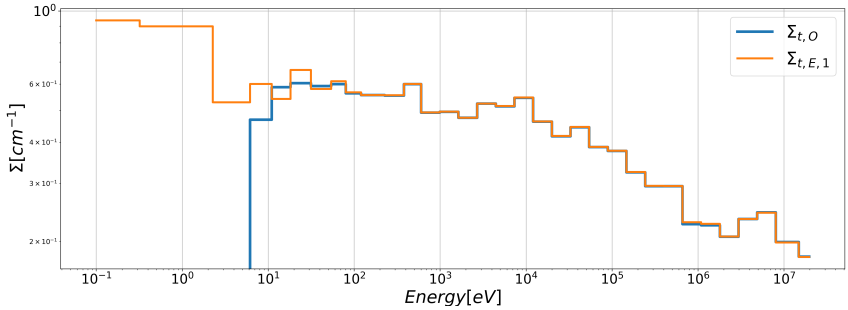

Figure 5.116: Cross-section for total reactions (XS).

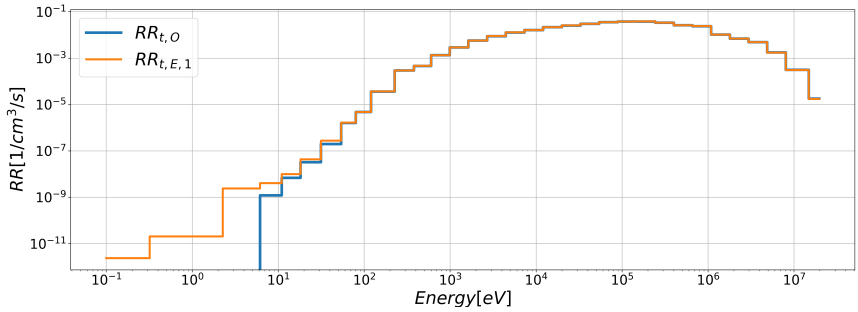

Figure 5.117: Reaction rate for total reactions (RR).

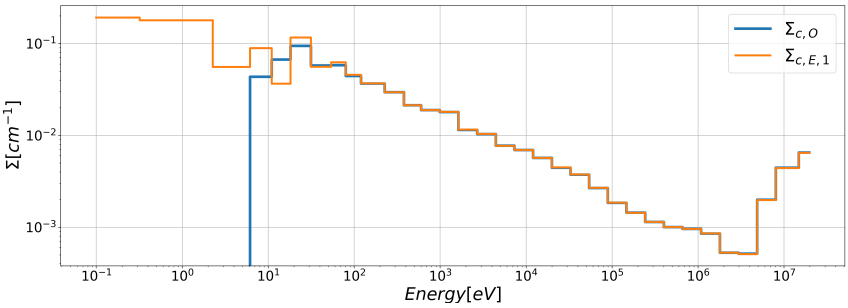

Figure 5.118: Cross-section for capture reactions (XS).

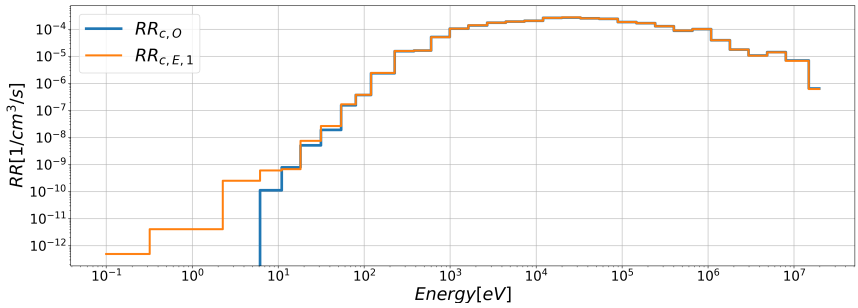

Figure 5.119: Reaction rate for capture reactions (RR).

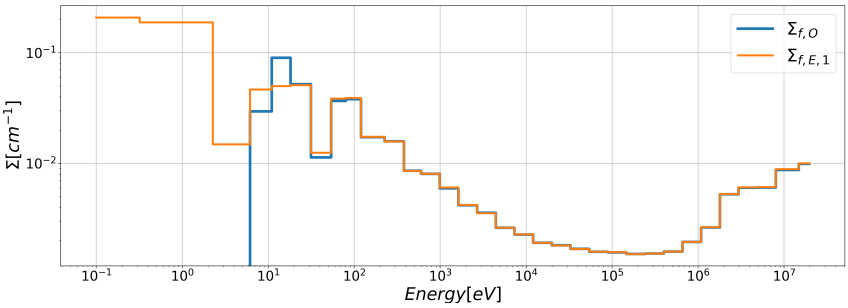

Figure 5.120: Cross-section for fission reactions (XS).

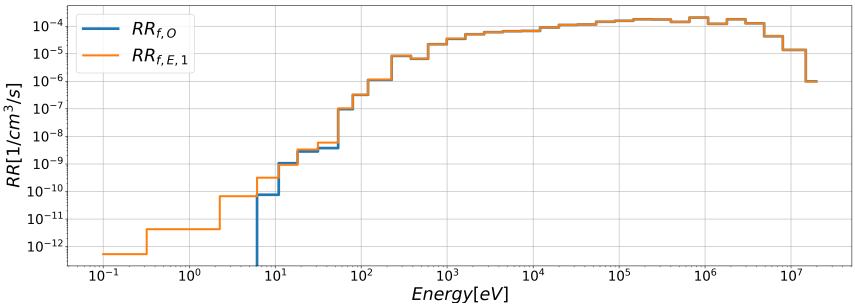

Figure 5.121: Reaction rate for fission reactions (RR).

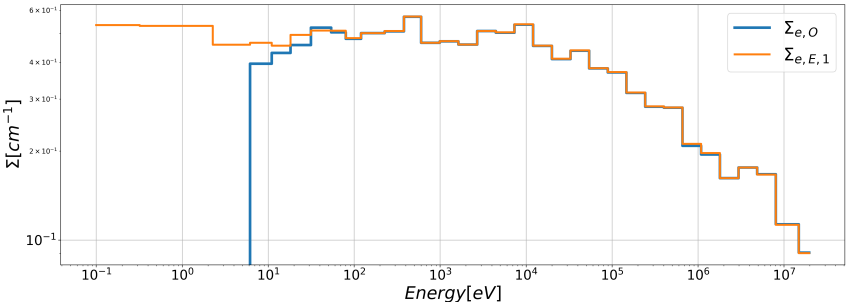

Figure 5.122: Cross-section for elastic reactions (XS).

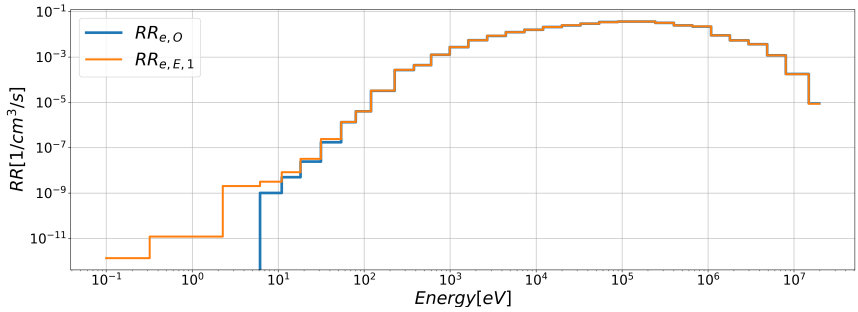

Figure 5.123: Reaction rate for elastic reactions (RR).

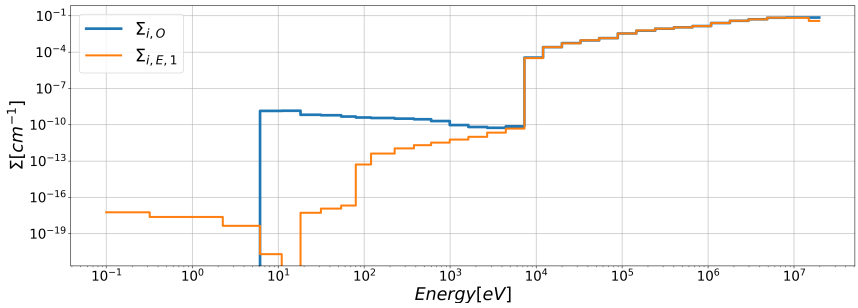

Figure 5.124: Cross-section for inelastic reactions (XS).

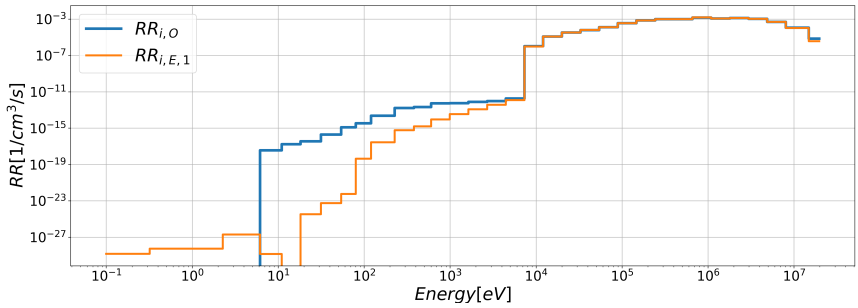

Figure 5.125: Reaction rate for inelastic reactions (RR).

To quantitatively assess the agreement between ECCO and OpenMC under the **33-group discretization**, the Root Mean Square (RMS) of the relative differences has been computed for the macroscopic cross sections Σ_x and the corresponding reaction rates RR_x across each reaction type. The results are summarized in Table ??.

	$RMS_{E/O}$	
	Σ_x	RR_x
TOTAL	0.01325	0.01470
CAPTURE	0.01885	0.02015
FISSION	0.02682	0.02834
ELASTIC	0.01168	0.01346
INELASTIC	-	0.01314

Table 5.23: Root Mean Square of $Sigma_x$ RR_x of each reaction rate on 33 G

It can be observed that the overall RMS errors for macroscopic cross sections and reaction rates are approximately $1.3\% - 2.6\%$ and the RMS values on the macroscopic cross sections (Σ_x) are generally low. No data is reported for the **inelastic** reaction channels in this analysis, as it can be seen from the graph that there is a significant discrepancy between the two curves. Issues were encountered with the OpenMC tally concerning the inelastic reaction, preventing a reliable comparison B.

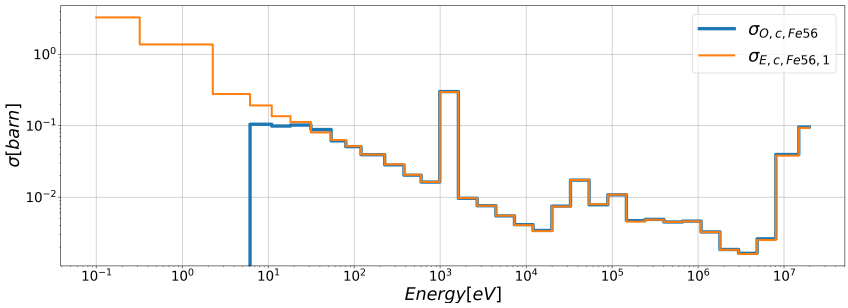

Figure 5.126: Cross-section for Fe56 capture (XS micro).

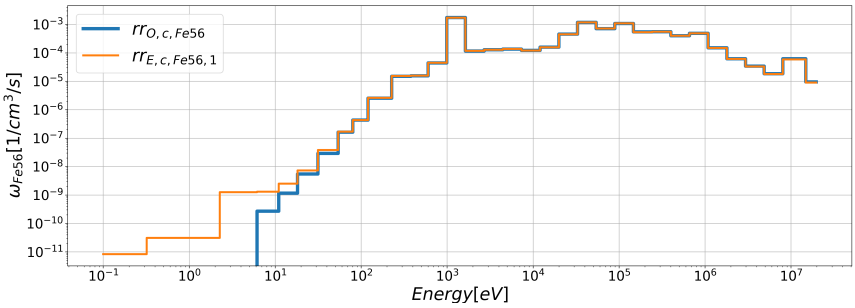

Figure 5.127: Reaction rate for Fe56 capture (RR micro).

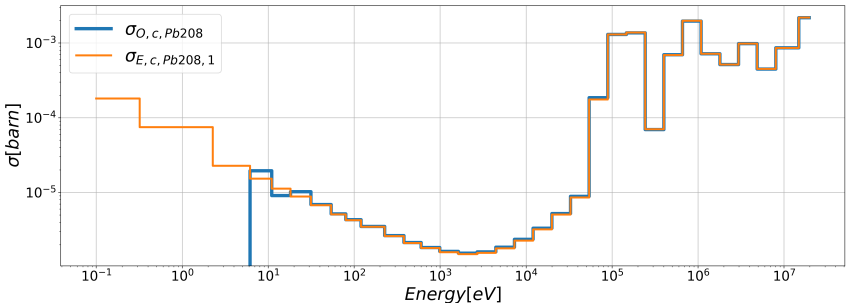

Figure 5.128: Cross-section for Pb208 capture (XS micro).

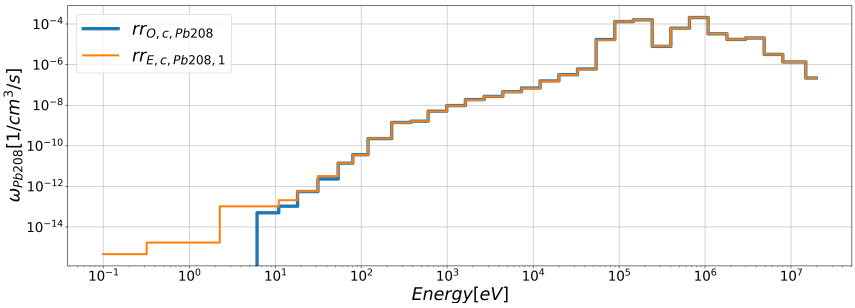

Figure 5.129: Reaction rate for Pb208 capture (RR micro).

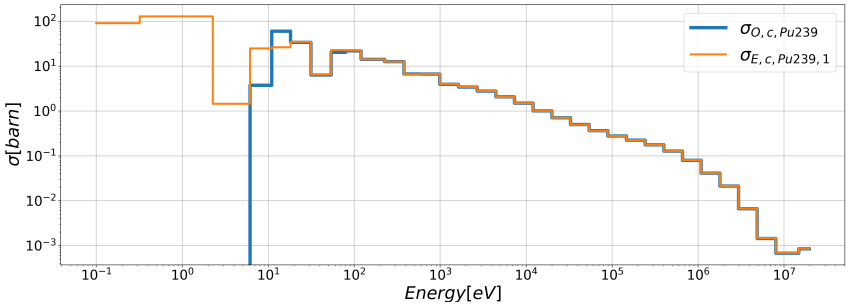

Figure 5.130: Cross-section for Pu239 capture (XS micro).

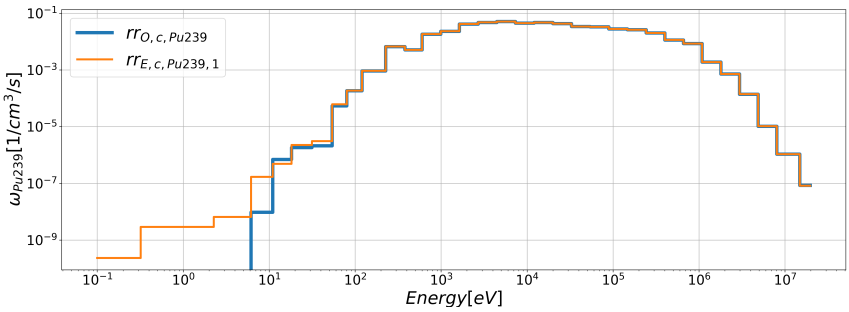

Figure 5.131: Reaction rate for Pu239 capture (RR micro).

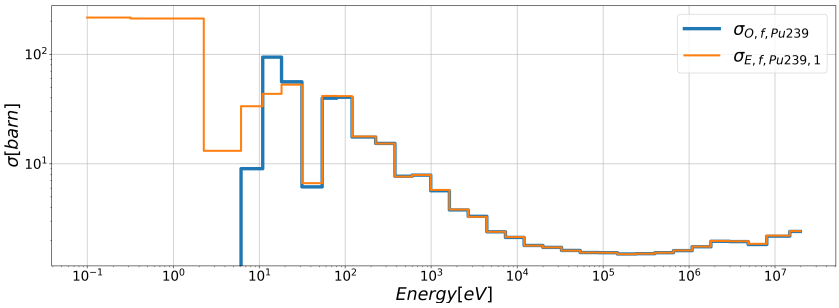

Figure 5.132: Cross-section for Pu239 fission (XS micro).

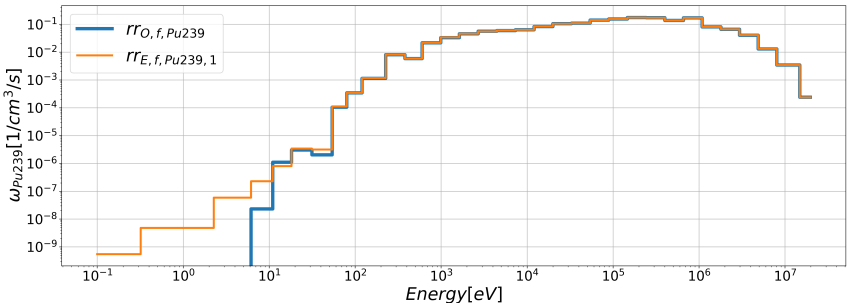

Figure 5.133: Reaction rate for Pu239 fission (RR micro).

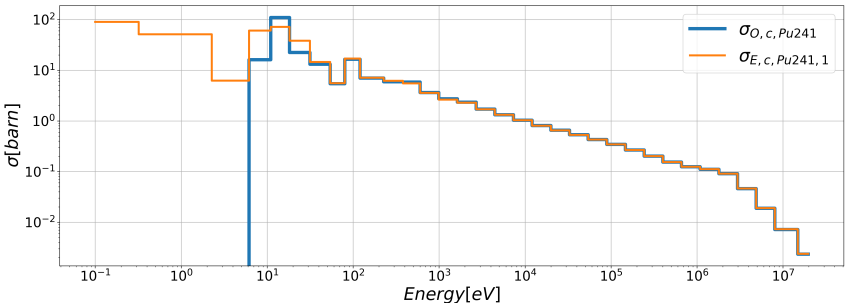

Figure 5.134: Cross-section for Pu241 capture (XS micro).

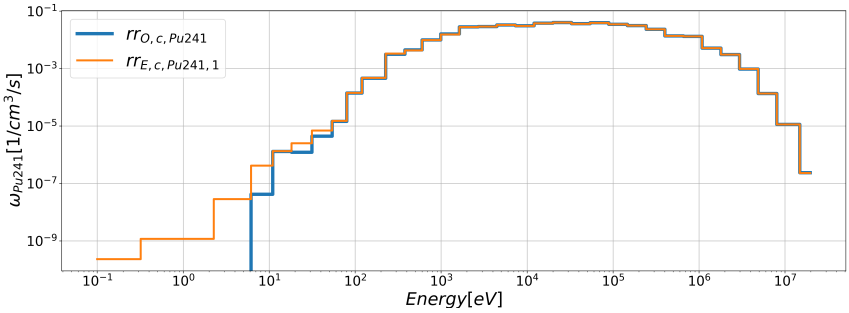

Figure 5.135: Reaction rate for Pu241 capture (RR micro).

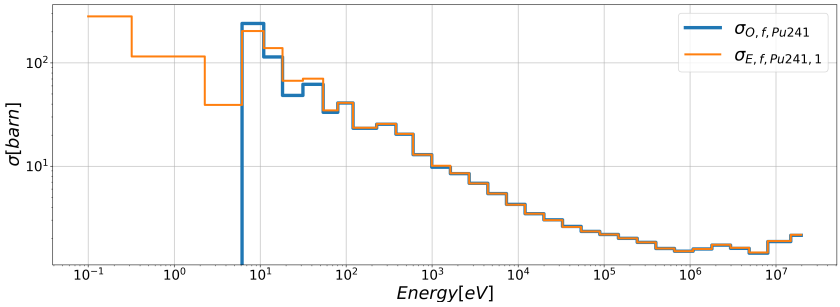

Figure 5.136: Cross-section for Pu241 fission (XS micro).

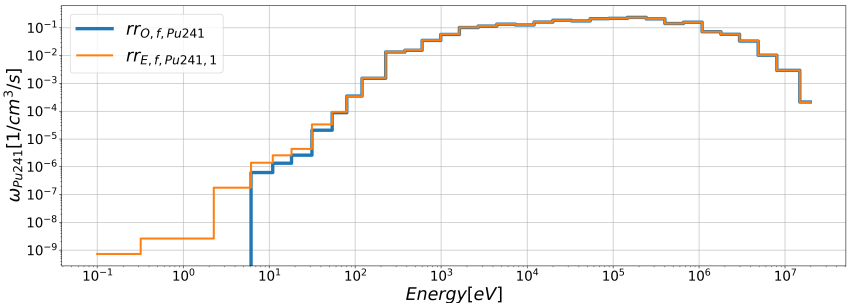

Figure 5.137: Reaction rate for Pu241 fission (RR micro).

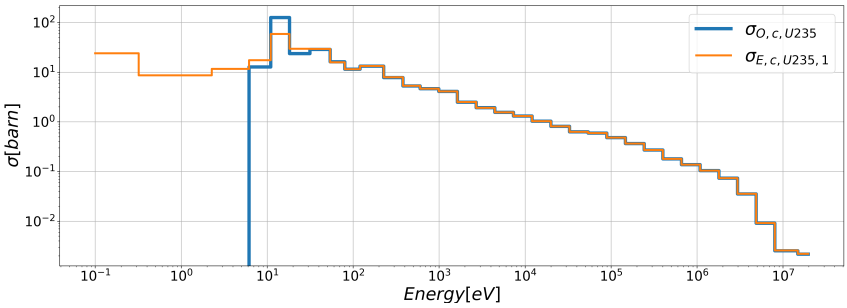

Figure 5.138: Cross-section for U235 capture (XS micro).

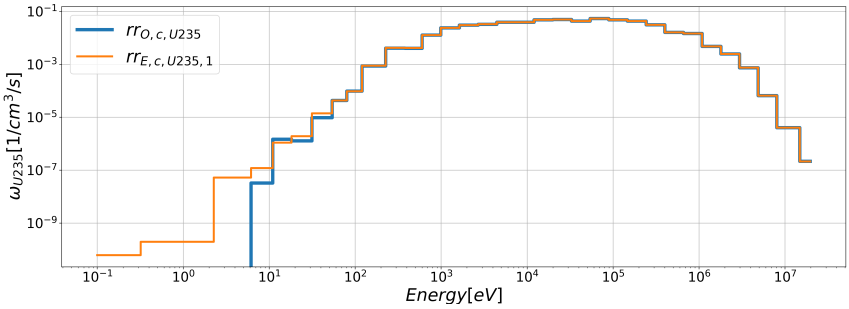

Figure 5.139: Reaction rate for U235 capture (RR micro).

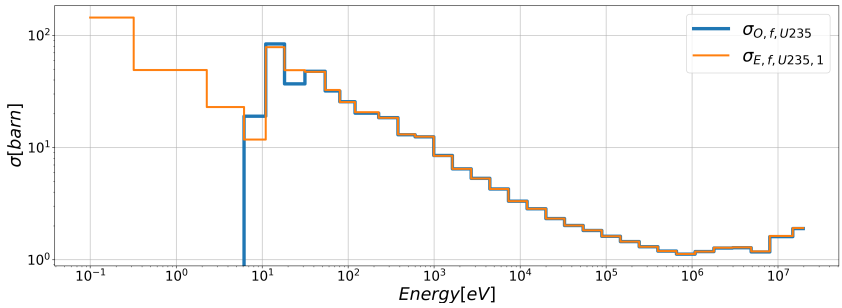

Figure 5.140: Cross-section for U235 fission (XS micro).

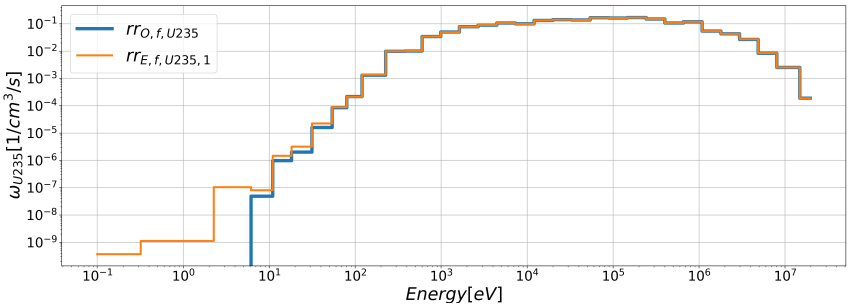

Figure 5.141: Reaction rate for U235 fission (RR micro).

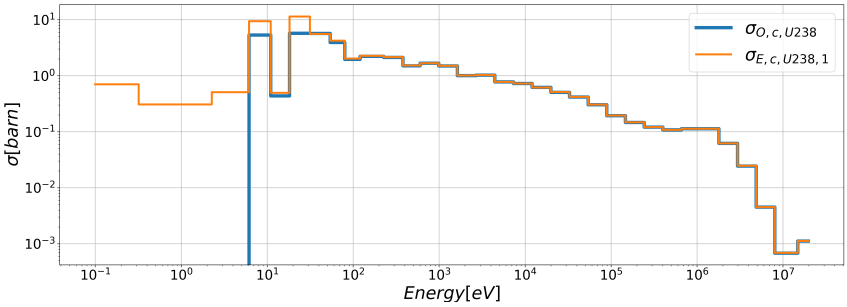

Figure 5.142: Cross-section for U238 capture (XS micro).

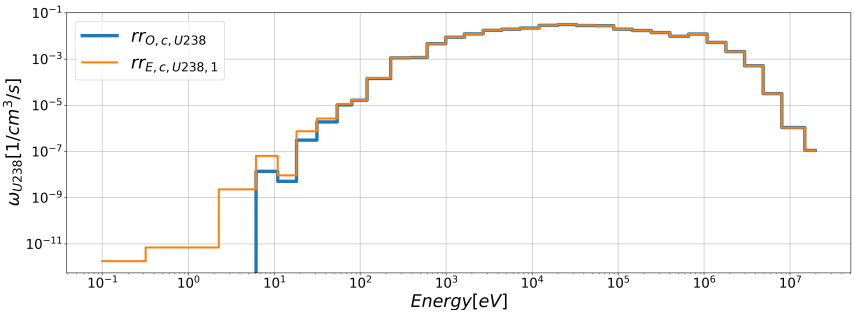

Figure 5.143: Reaction rate for U238 capture (RR micro).

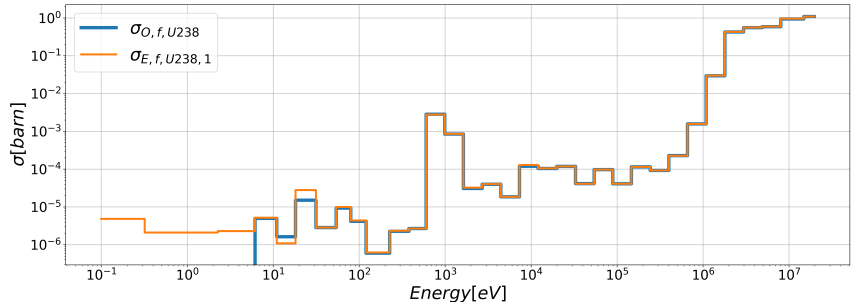

Figure 5.144: Cross-section for U238 fission (XS micro).

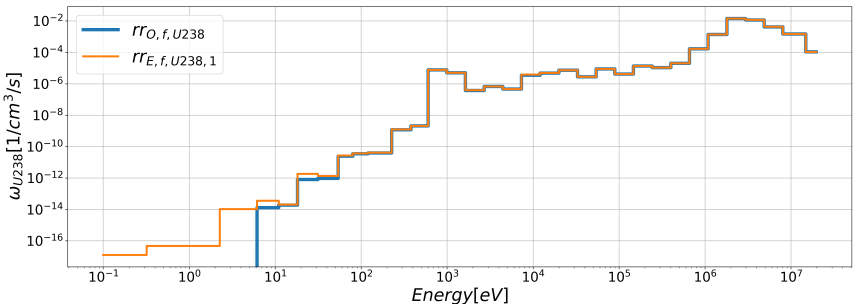

Figure 5.145: Reaction rate for U238 fission (RR micro).

==========

		$\varepsilon_{E/O}$	
		σ_x	rr_x
Fe^{56}	CAT	0.03765	0.03667
Pb^{208}	CAT	0.06845	0.06695
Pu^{239}	FIS	0.01400	0.01543
	CAT	0.01241	0.01386
Pu^{241}	FIS	0.01830	0.01966
	CAT	0.01271	0.01135
U^{235}	FIS	0.01534	0.01669
	CAT	0.01825	0.01962
U^{238}	FIS	0.04315	0.04446
	CAT	0.02444	0.02573

Table 5.24: Root Mean Square of microscopic cross section and reaction rate far each isotopes.

The RMS values for macroscopic cross sections are generally around **1-7%**, are very close between cross sections and reaction rates.

The higher error is again the microscopic cross section of capture of Pb^{208}.

We have previously derived the normalization approach, which now allows us to quantify the **weight of each isotope** with respect to the infinite multiplication factor k_{inf} and reactivity.

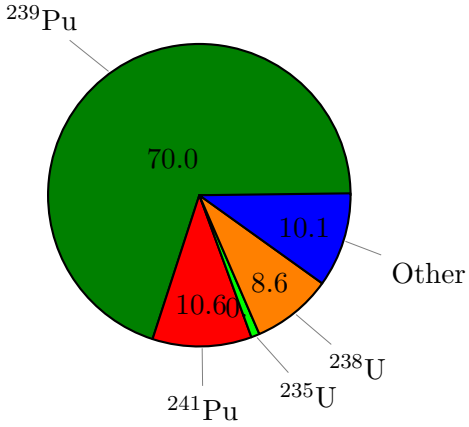

Figure 5.146: Weight of fissionable isotopes with respect to k_{inf}.

The pie chart highlights that ^{239}**Pu** is the most influential isotope on k_{inf}, both due to its high contribution to fission and its relevance in fast-spectrum reactors like ALFRED.

To analyze the detailed behavior, the group-wise differences in macroscopic fission

reaction rates between ECCO and OpenMC for ^{239}Pu are reported in Figure 5.147. The difference is defined as:

$$\Delta rr_{^{239}\mathrm{Pu},g} = rr_{^{239}\mathrm{Pu},g,E} - rr_{^{239}\mathrm{Pu},g,O}, \tag{5.12}$$

where g is the energy group index.

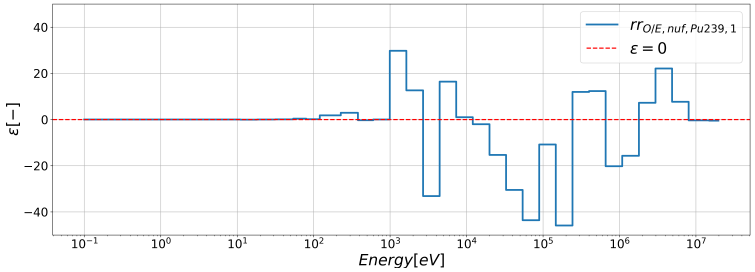

Figure 5.147: Group-wise Δk comparison for ^{239}Pu.

The plot shows both positive and negative differences, indicating **compensation effects** across energy groups, where discrepancies in certain ranges are balanced by opposite deviations in others, preserving the overall consistency in reactivity calculations.

The integrated difference across all groups is summarized below:

^{239}Pu	$S_{E/O}$
Δrr	-91

Table 5.25: Integrated difference Δrr between ECCO and OpenMC for ^{239}Pu.

Here, $\Delta rr = \sum_g \Delta rr_{^{239}\mathrm{Pu},g}$ quantifies the total difference in macroscopic fission reaction rates for ^{239}Pu between the two codes.

Moving forward, we now compute the isotope weight with respect to the reactivity, ρ

The chart demonstrates that ^{238}**U** becomes significantly more important when considering ρ, due to its role in resonance absorption and scattering, making it a key isotope for assessing the impact of fine-group structures compared to coarse-group libraries.

To highlight this, Figure 5.149 presents the group-wise Δk for ^{238}U:

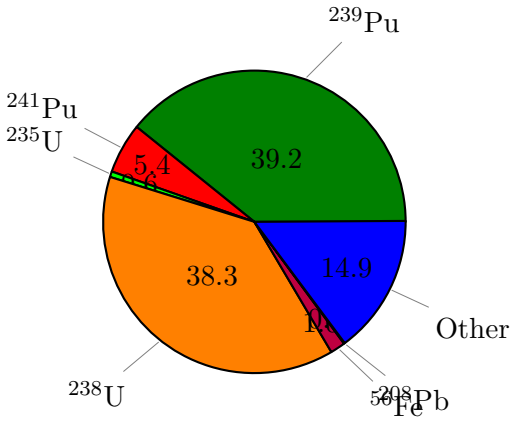

Figure 5.148: Weight of isotopes with respect to ρ.

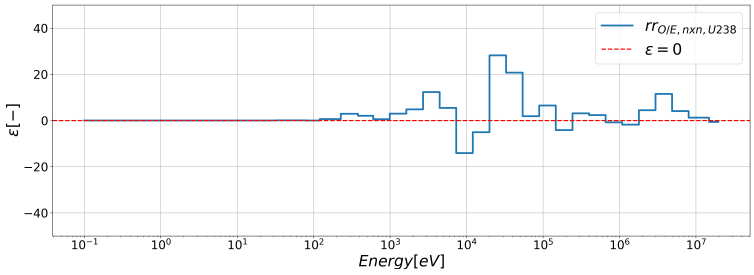

Figure 5.149: Group-wise Δk comparison for ^{238}U.

where the difference is defined as:

$$\Delta rr_{^{238}\mathrm{U},g} = rr_{^{238}\mathrm{U},g,E} - rr_{^{238}\mathrm{U},g,O}. \tag{5.13}$$

The figure shows both positive and negative contributions across energy groups, indicating compensation effects similar to the ^{239}Pu case. It is also observed that discrepancies are reduced in subsequent refinement steps, confirming that using fine-group structures significantly improves the consistency of cross-section treatment for key isotopes like ^{238}U, which is critical in fast-spectrum reactor analyses.

^{238}U	$S_{E/O}$ [pcm]
Δrr	90

Table 5.26: Integrated difference Δrr between ECCO and OpenMC for ^{238}U.

172G analysis In the end there is this analsys of assembly on 172G discretization.

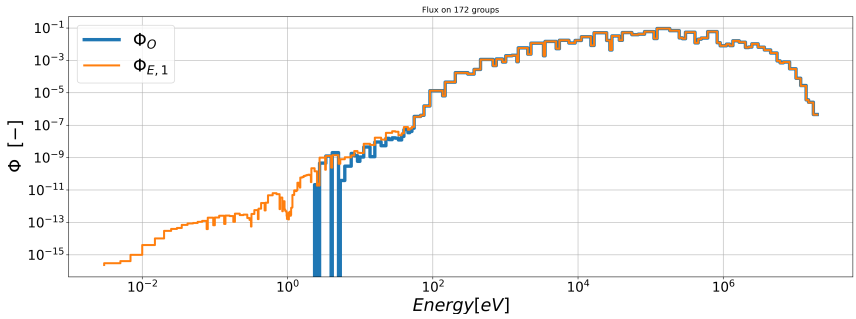

Figure 5.150: Flux on 172 groups of heterogeneous pin.

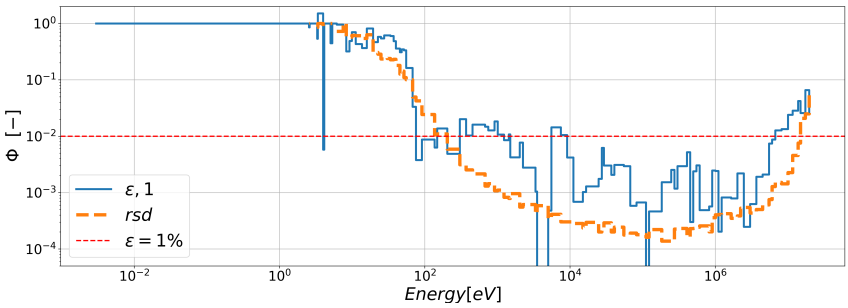

Figure 5.151: Comparison of the flux on 172 groups of heterogeneous pins.

$$RMS_{E/O} = 0.04454 \tag{5.14}$$

Here find the highest error on the flux, as expeted more complexivity, more approximation could be translated into a higher error. ———————————————-

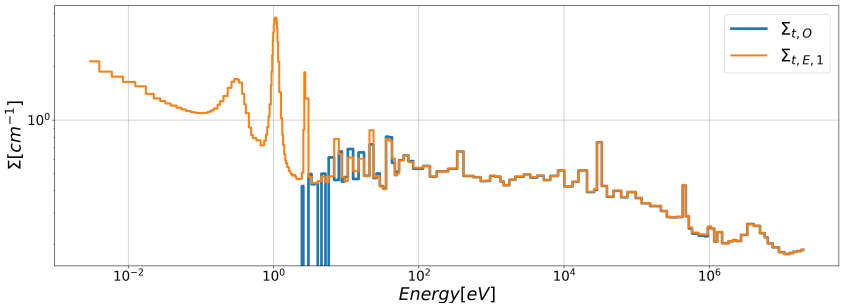

Figure 5.152: Cross-section for total reactions (XS).

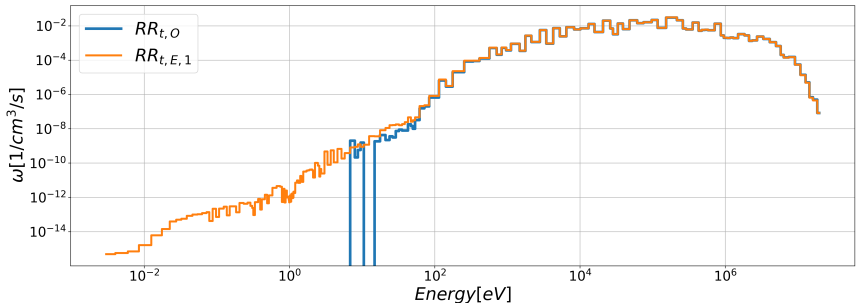

Figure 5.153: Reaction rate for total reactions (RR).

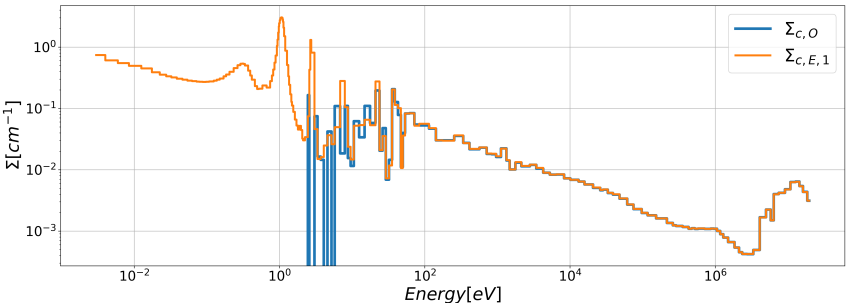

Figure 5.154: Cross-section for capture reactions (XS).

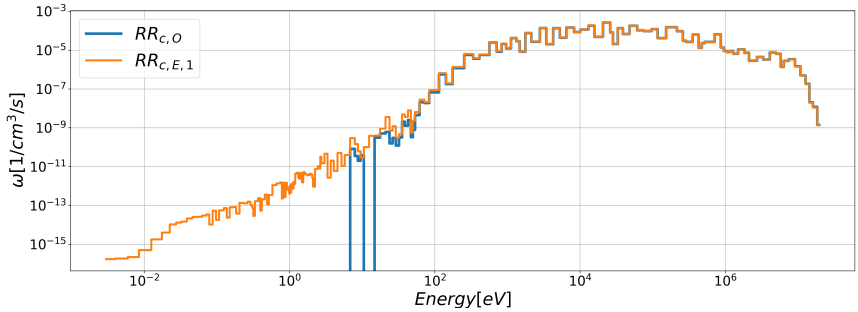

Figure 5.155: Reaction rate for capture reactions (RR).

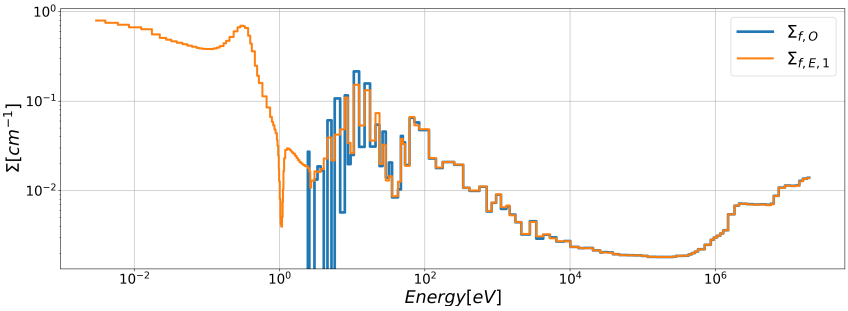

Figure 5.156: Cross-section for fission reactions (XS).

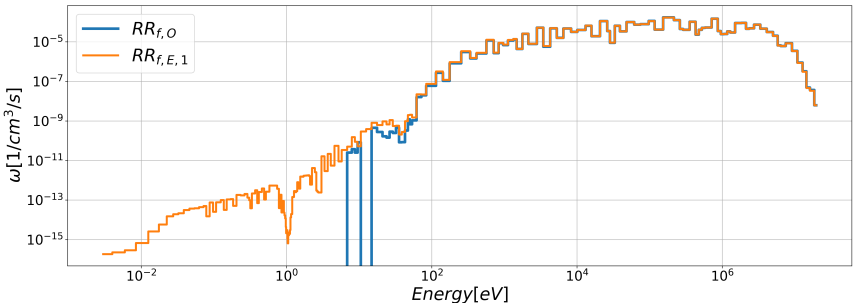

Figure 5.157: Reaction rate for fission reactions (RR).

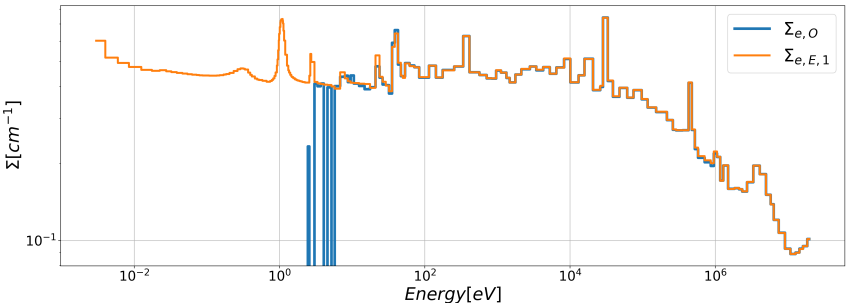

Figure 5.158: Cross-section for elastic reactions (XS).

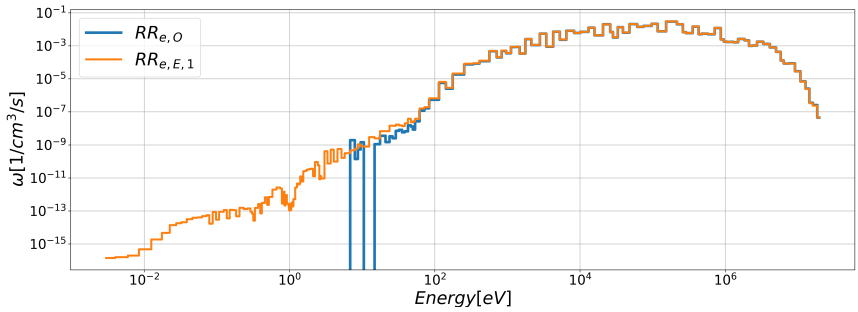

Figure 5.159: Reaction rate for elastic reactions (RR).

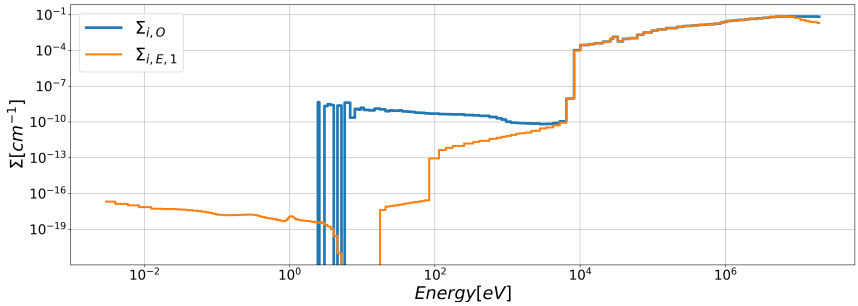

Figure 5.160: Cross-section for inelastic reactions (XS).

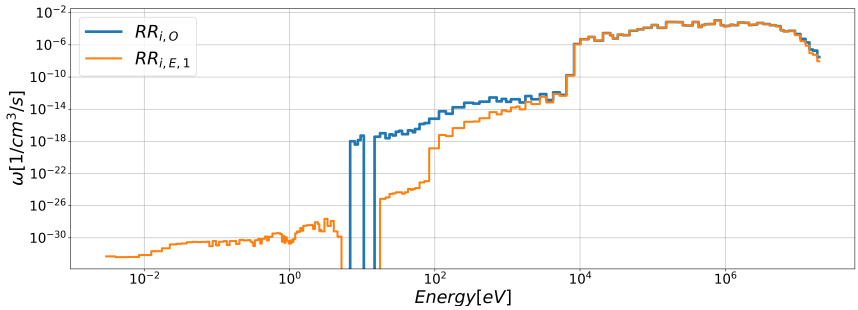

Figure 5.161: Reaction rate for inelastic reactions (RR).

Evaluation of root mean square to summarise the previus plots:

$RMS_{E/O}$		
	Σ_x	RR_x
TOTAL	0.01943	0.02510
CAPTURE	0.02784	0.01656
FISSION	0.01124	0.03333
ELASTIC	0.01892	0.0262
INELASTIC	-	-

Table 5.27: Root Mean Square of $Sigma_x$ RR_x of each reaction rate on 172 G

The error on the macroscopic parameters are between the 1 and 3 %, is sligth higer but in general these quantities has not a difference of order of magnitude for the RMS.

Let's move on the last microscopic analysis of cross section and reaction rates.

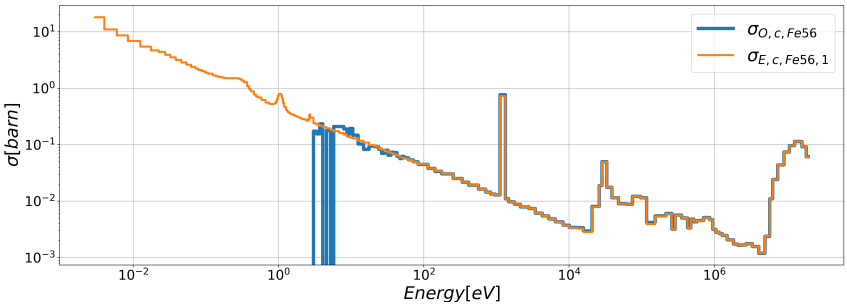

Figure 5.162: Cross-section for Fe56 capture (XS micro).

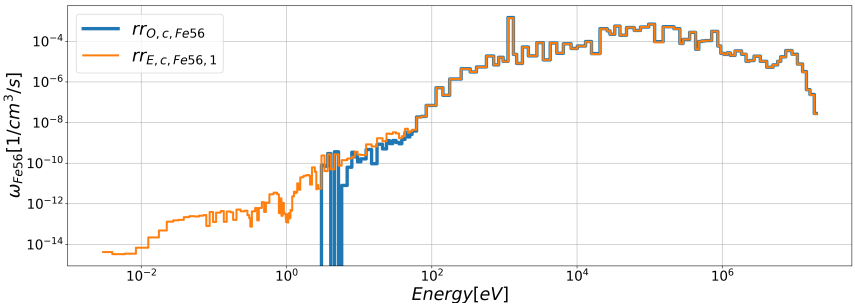

Figure 5.163: Reaction rate for Fe56 capture (RR micro).

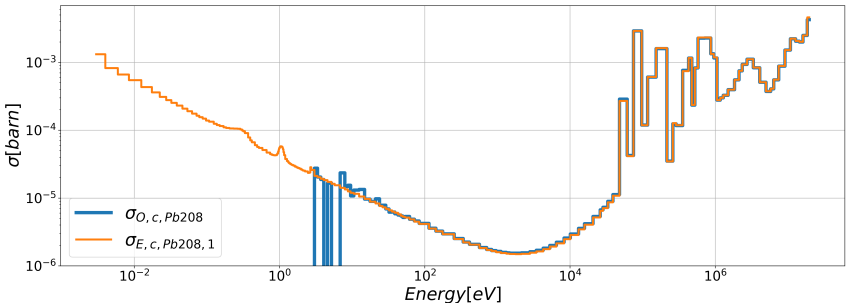

Figure 5.164: Cross-section for Pb208 capture (XS micro).

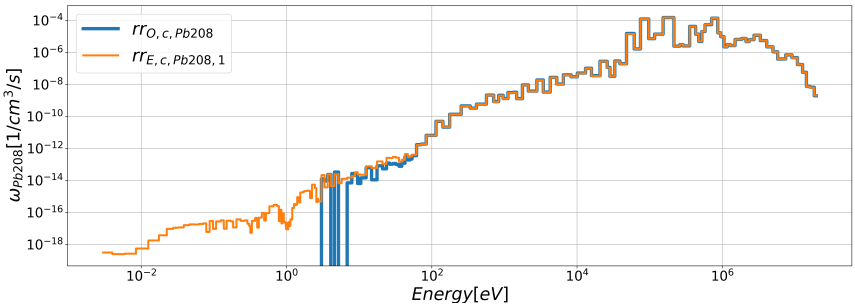

Figure 5.165: Reaction rate for Pb208 capture (RR micro).

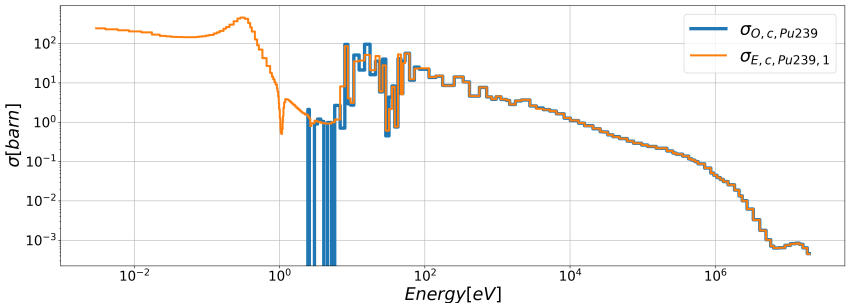

Figure 5.166: Cross-section for Pu239 capture (XS micro).

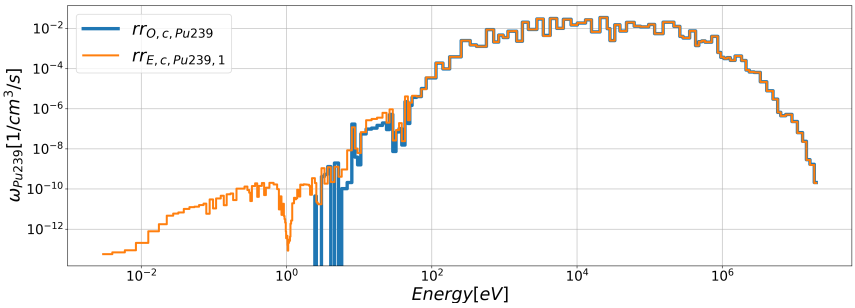

Figure 5.167: Reaction rate for Pu239 capture (RR micro).

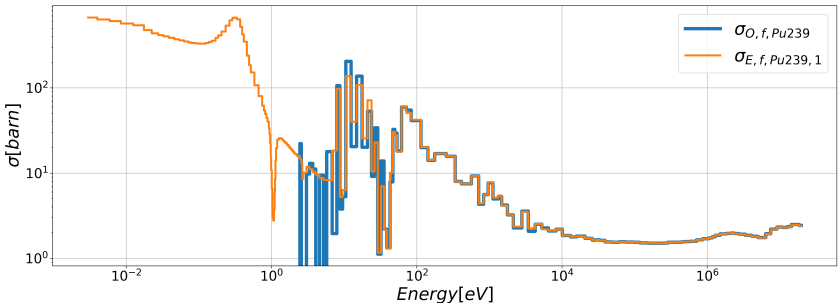

Figure 5.168: Cross-section for Pu239 fission (XS micro).

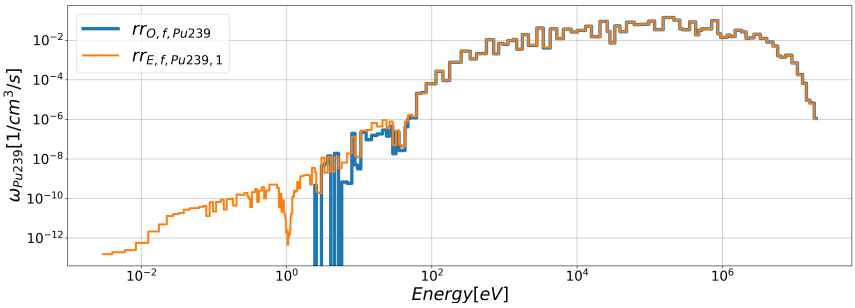

Figure 5.169: Reaction rate for Pu239 fission (RR micro).

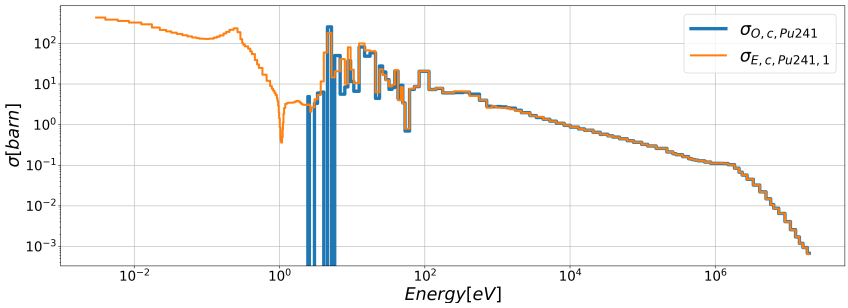

Figure 5.170: Cross-section for Pu241 capture (XS micro).

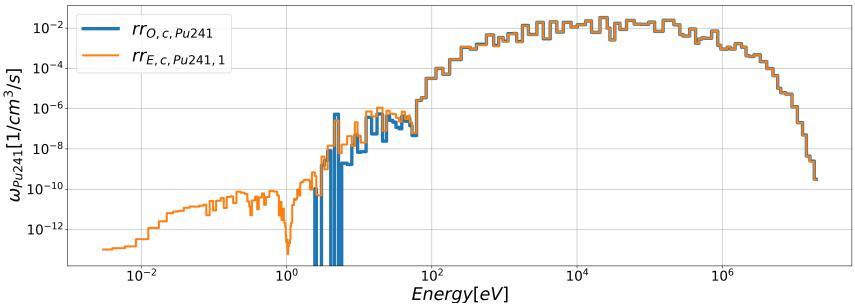

Figure 5.171: Reaction rate for Pu241 capture (RR micro).

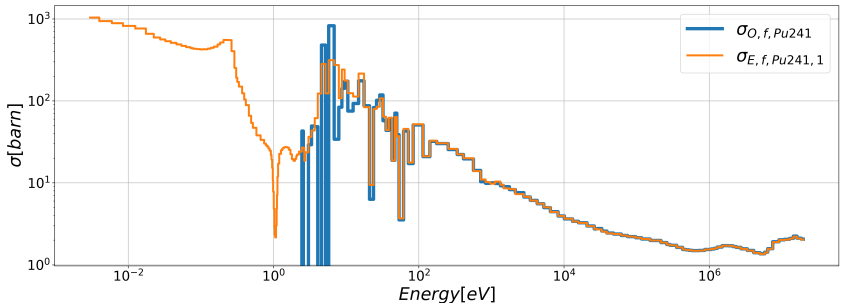

Figure 5.172: Cross-section for Pu241 fission (XS micro).

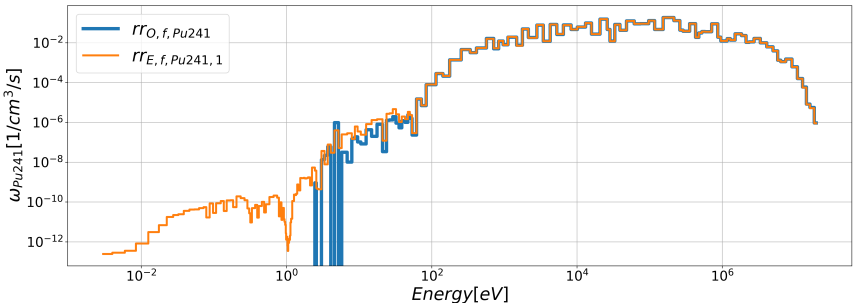

Figure 5.173: Reaction rate for Pu241 fission (RR micro).

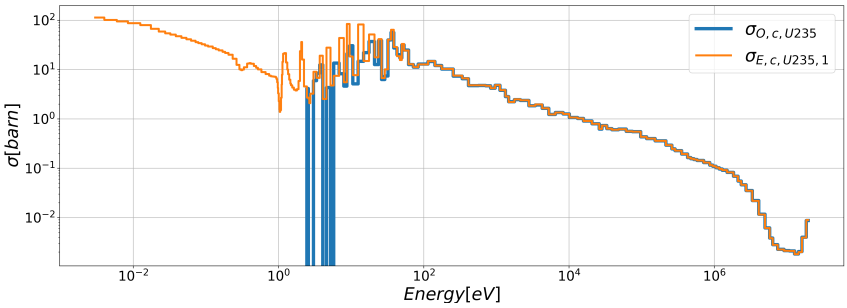

Figure 5.174: Cross-section for U235 capture (XS micro).

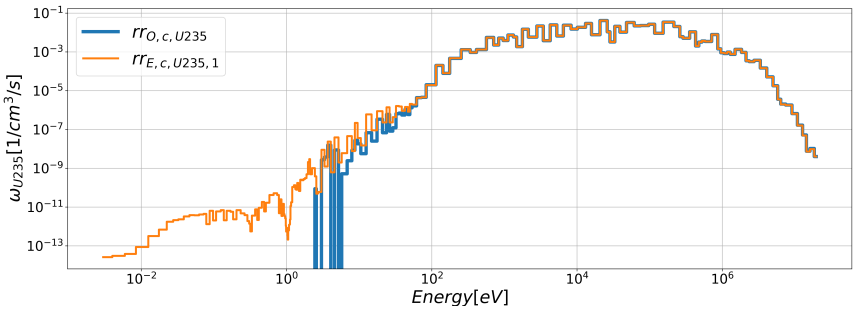

Figure 5.175: Reaction rate for U235 capture (RR micro).

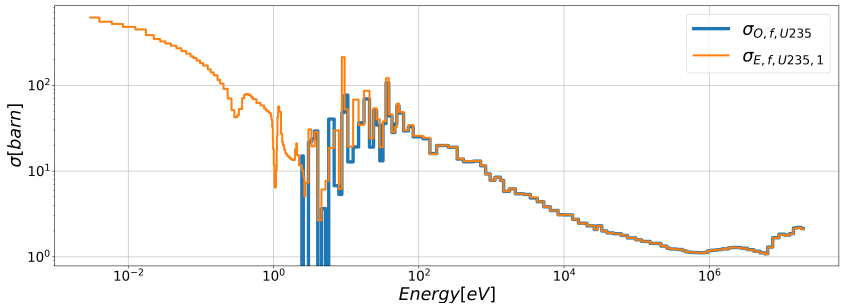

Figure 5.176: Cross-section for U235 fission (XS micro).

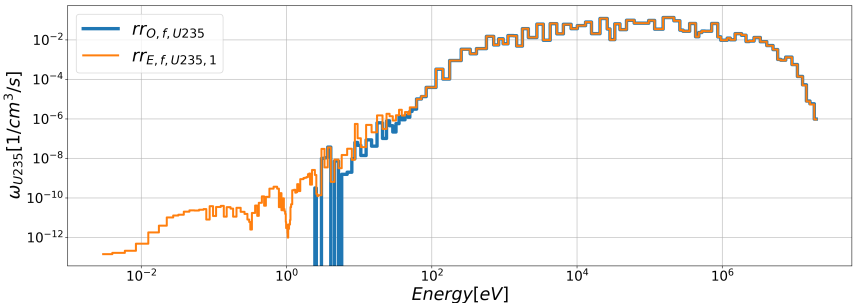

Figure 5.177: Reaction rate for U235 fission (RR micro).

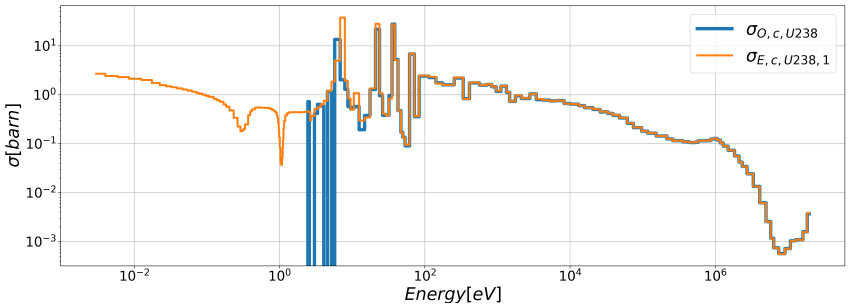

Figure 5.178: Cross-section for U238 capture (XS micro).

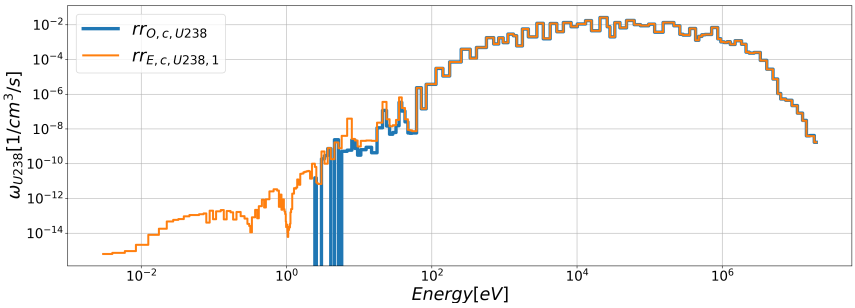

Figure 5.179: Reaction rate for U238 capture (RR micro).

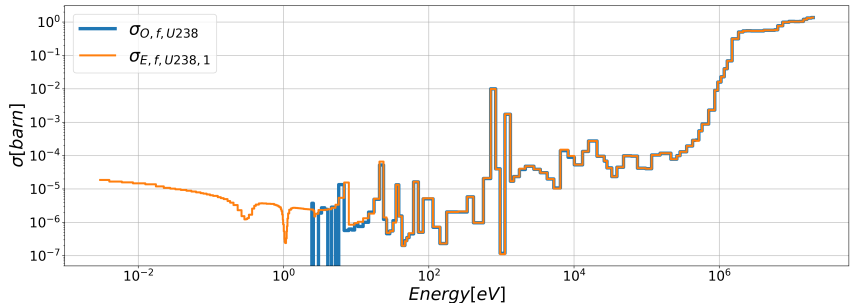

Figure 5.180: Cross-section for U238 fission (XS micro).

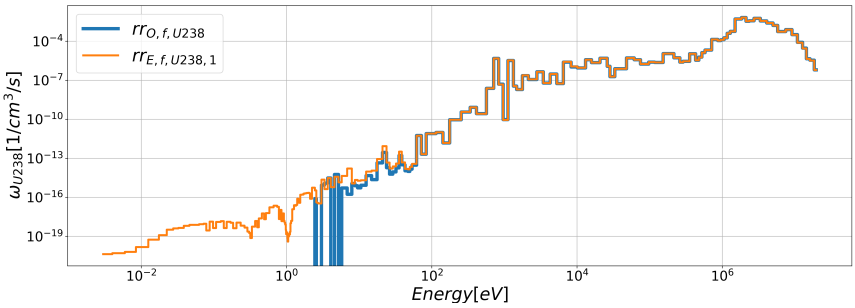

Figure 5.181: Reaction rate for U238 fission (RR micro).

		$\varepsilon_{E/O}$	
		σ_x	rr_x
Fe^{56}	CAT	0.04071	0.07716
Pb^{208}	CAT	0.0901	0.12281
Pu^{239}	FIS	0.01420	0.01949
	CAT	0.00483	0.03413
Pu^{241}	FIS	0.00335	0.03073
	CAT	0.04966	0.08325
U^{235}	FIS	0.00155	0.02835
	CAT	0.00251	0.03267
U^{238}	FIS	0.01389	0.02353
	CAT	0.02360	0.01253

Table 5.28: Root Mean Square of microscopic cross section and reaction rate far each isotopes.

Generally has the same behaviour of heterogeneous pin on 172G, indeed the highest error is on Pb^{208} on capture reaction.

We have just seen how to derive normalisation, and now we can understand its utility, and start with the possibility to understand the weight of each isotope on the k and reactivity:

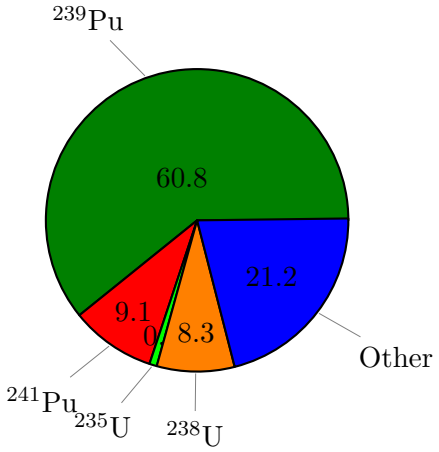

The plot is a comparison of the most important nuclide in term of difference between the calculation ^{239}Pu, and also in term of important of the k.

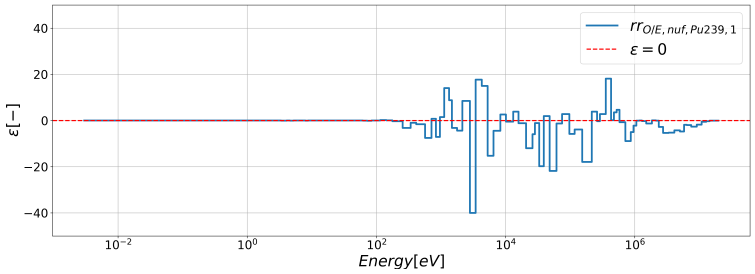

Figure 5.182: Comparison of Δk of ^{239}Pu

Where $\Delta rr_{^{239}Pu} = rr_{^{239}Pu,g,E} - rr_{^{239}Pu,g,O}$ is the difference between ECCO and OpenMC of the macroscopic reaction rate of group **g**.

The plots show the delta k in each groups for the nuclide ^{239}Pu and it shows positive and negative ϵ, that can be associeted to compensation effect.

^{239}Pu	$S_{E/O}$
Δrr	-117

Where $\Delta rr = \sum_g(\Delta rr_{^{239}Pu})$ is the sum of the difference between ECCO and OpenMC for each groups.

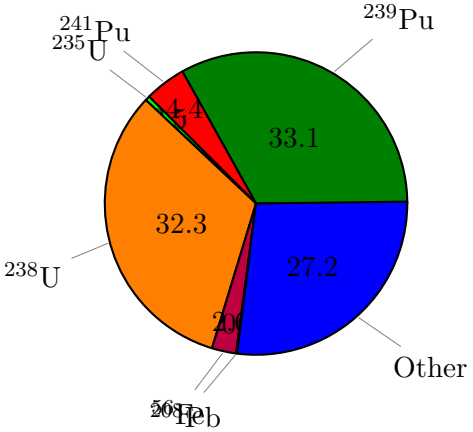

The nuclide ^{238}U was selected because it significantly highlights the transition from a coarse library to a fine one.

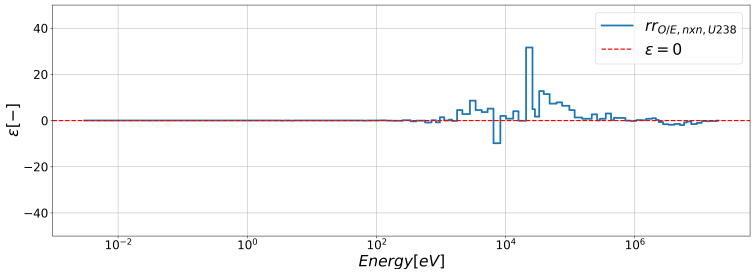

Figure 5.183: Comparison of Δk of ^{238}U

Where $\Delta rr_{^{238}U} = rr_{^{238}U,g,E} - rr_{^{238}U,g,O}$ is the difference between ECCO and OpenMC of the macroscopic reaction rate of group **g**.

The plots show the delta k in each groups for the nuclide ^{238}U and it shows positive and negative ϵ. It possible to notice errors on the 3th step are lower.

^{238}U	$S_{E/O}$ [pcm]
Δrr	118

Table 5.29: Integrated difference Δrr between ECCO and OpenMC for ^{238}U.

Chapter 6

Conclusion

In this work, the capability of the **ECCO** code to compute the **condensed and homogenized cross sections** of an **LFR (ALFRED) reactor** was verified through benchmarking against **OpenMC** Monte Carlo calculations. The analyses were conducted progressively on three configurations: **homogeneous pin**, **heterogeneous pin**, and **heterogeneous assembly**.

For the **homogeneous pin**:

- The setup analysis confirmed that the methods employed provide consistent outputs, justifying the use of the `p1 consistent` option in ECCO.
- The adoption of the **1968 library** for the treatment of resonant isotopes proved beneficial, resulting in a reduction of the error on k_{inf} of several hundreds of pcm.
- The normalization analyses highlighted that the isotopes contributing the most to k and to the reactivity are ^{239}**Pu** and ^{238}**U**.

In the **heterogeneous cases**:

- The previous results were confirmed also in this scenario, showing that the average errors in the **macroscopic cross sections** calculated by ECCO compared to those from OpenMC are in the order of **1–3%** (approximately 10^3 pcm).
- Additional analyses on **microscopic cross sections and reaction rates** highlighted that for certain isotopes and reactions, discrepancies can reach up to **10%**.
- The representation of the assembly from 2 to 7 regions demonstrated a closer match to the Monte Carlo reference values.

The following table summarizes the results across the three configurations:

It can be observed that the **heterogeneous assembly** configuration yields the k value closest to the reference; however, this agreement might be due to compensation effects, as indicated by the normalization analyses.

As reiterated throughout this thesis, this work represents the **first step of V&V campaign performed at Newcleo concerning the ECCO code** for its future use in the design of LFR reactors. The aim of this V&V activity is to generate homogenized

Table 6.1: Comparison of k_{inf} between ECCO and OpenMC with deviations

k_{inf}	ECCO	OpenMC		Δk
Pin-Homo	1.35267	1.35480	± 0.00011	213 pcm
Pin-Hete	1.35315	1.35581	± 0.00015	266 pcm
Asse-Hete	1.28584	1.28690	± 0.00013	106 pcm

and condensed pin and assembly cross sections to accelerate partial or full-core reactor calculations during the design phase.

Future Work

The results obtained open different paths for future development:

- **Extending the analysis to inactive regions of the reactor**(e.g. control rods, reflector ,etc.), to assess ECCO's predictive capability under non-multiplicative conditions.
- **Assessing the acceptability of the discrepancies through perturbative studies**, to determine whether the differences with OpenMC are acceptable for design purposes.
- **Further investigating the homogeneous pin phase**, to identify the causes of the residual discrepancies between ECCO and OpenMC, with the goal of pinpointing sources of error and potentially improving the cross section treatment, particularly for the **microscopic cross sections and reaction rates** where discrepancies up to **10%** were observed.

This work, therefore, provides a solid foundation for the deployment of ECCO in new-cleo's workflows, enabling fast and reliable preparation of cross sections for LFR design calculations, while highlighting areas for improvement to further refine the accuracy of macroscopic and microscopic nuclear data predictions.

Appendix A

Transport cross section

The formula of the transport cross section is the following:

$$\Sigma_{tr} = \Sigma_t - \mu\Sigma_{s,0} = \Sigma_t - \Sigma_{s,1} \tag{A.1}$$

where Σ_t is the total cross section, μ average angle of scattering, $\Sigma_{s,0}$ is the moment of scattering of order 0, $\Sigma_{s,1}$ is the moment of scattering of order 1.

In Ecco there are a lots of option and in base of them, the output change an example is :

- PN_MOMENT 0 $\rightarrow \Sigma^{g*}_{tot} = \Sigma^{g}_{tr}$;
- PN_MOMENT n, with n>0 $\rightarrow \Sigma^{g*}_{tot} = \Sigma^{g}_{t1}$;
- add at the end P0_TOTAL $\rightarrow \Sigma^{g*}_{tot} = \Sigma^{g}_{tot}$.

where Σ^{g*}_{tot} is the value in the output file of ECCO. Oblusly the first idea to have as output the Transport cross section is the PN_MOMENT 0, but it is not the correct one if we are in 1G analisys because: with **extended transport approximation**

$$\sum_{g'} \Sigma_{sl,g'\rightarrow g}\phi_{g'} \approx \sum_{g'} \Sigma_{sl,g\rightarrow g'}\phi_{g'} \tag{25}$$

thus

$$\Sigma_{tr,g} = \Sigma_{t1,g} - \sum_{g'} \Sigma_{sl,g\rightarrow g'} \tag{26}$$

but the up-scattering in 1g is 0, so:

$$\Sigma_{tr,g} = \Sigma_{t1,g} \tag{26}$$

Appendix B

Cross- section: Inelastic

As mentioned in the results understanding, there is a discrepancy between the inelasticity of ECCO and OpenMC. Plots of the work on microscopic sections of some isotopes rpoducted from the simulations and those taken from JANIS will be shown below.

Fe56:

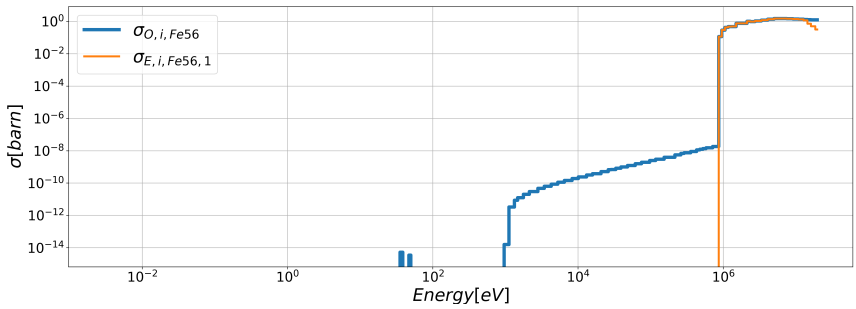

Figure B.1: microscopic Inelastic cross section microscopi of Fe56 of ECCO and OpenMC

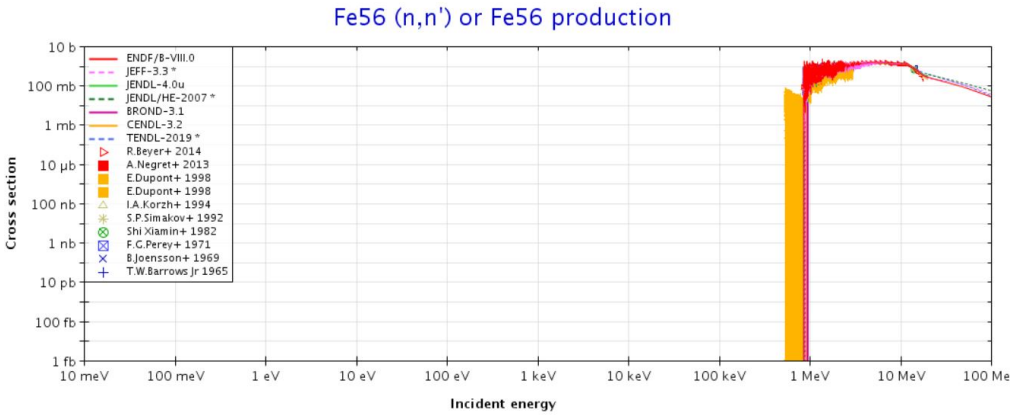

Figure B.2: microscopic n,n' cross section microscopic of Fe56 by JANIS [22]

Pu239:

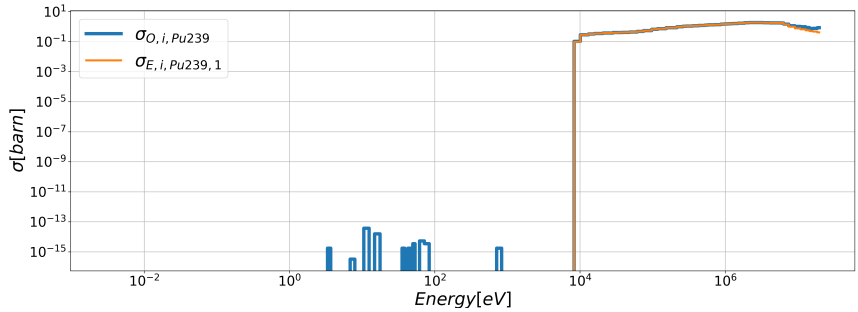

Figure B.3: microscopic Inelastic cross section microscopi of Pu239 of ECCO and OpenMC

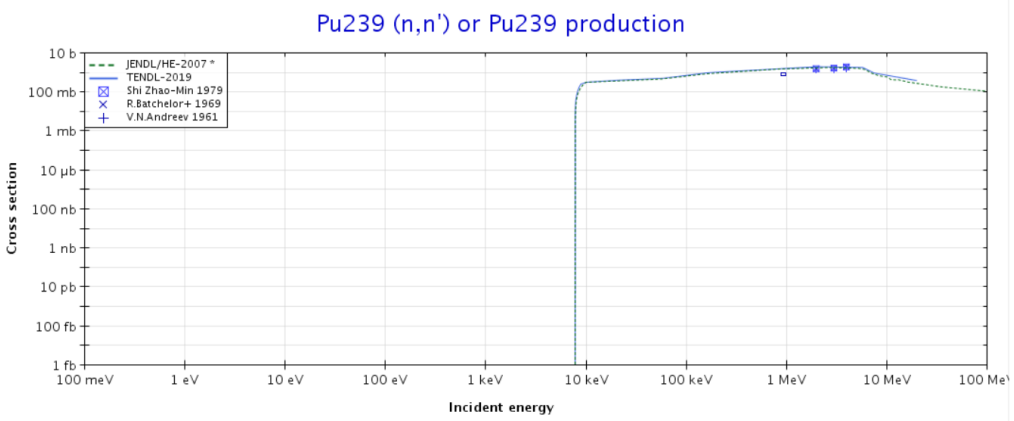

Figure B.4: microscopic n,n' cross section microscopi of Pu239 by JANIS [22]

U238:

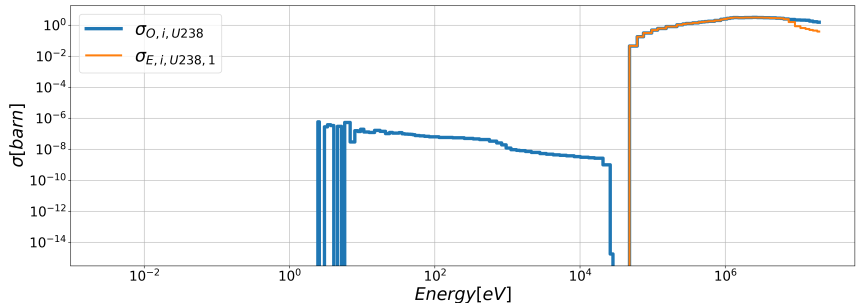

Figure B.5: microscopic Inelastic cross section microscopi of U238 of ECCO and OpenMC

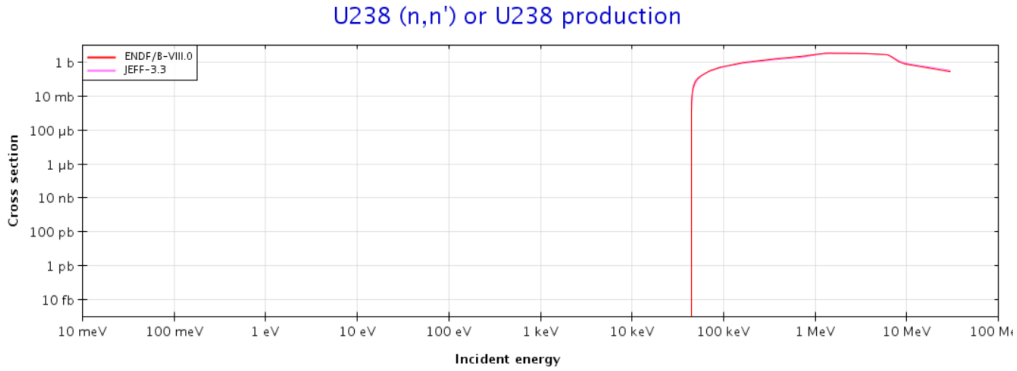

Figure B.6: microscopic n,n' cross section microscopi of U238 by JANIS [22]

U235:

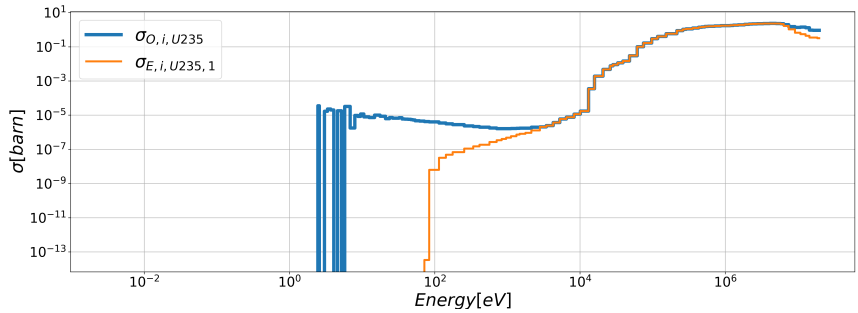

Figure B.7: microscopic Inelastic cross section microscopi of U235 of ECCO and OpenMC

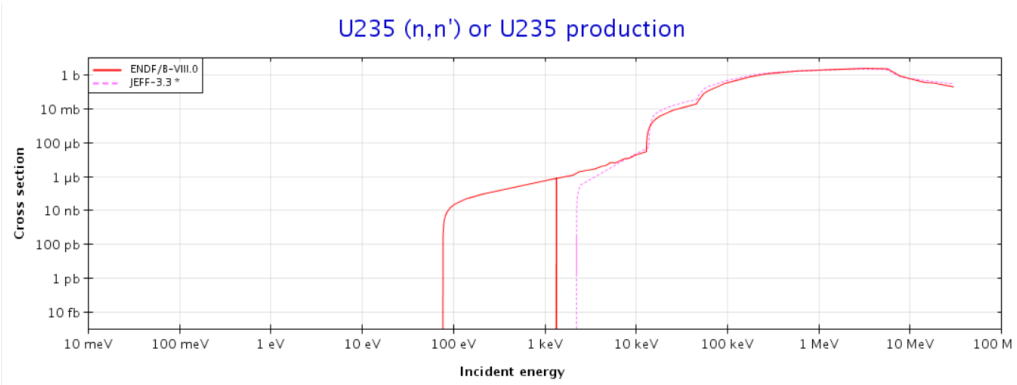

Figure B.8: microscopic n,n' cross section microscopi of U235 by JANIS [22]

The analysis was done for all the various nuclides that were indicated in the tables during the thesis, and the same phenomenon was found: ECCO described these the reaction more accurately than OpenMC. Checking on the forum, the problem is related to the tally that evaluates the particular reaction and not the code.

Bibliography

[1] Jack P.C. Kleijnen *Verification and validation of simulation models* .

[2] Roberto Ponciroli, Antonio Cammi, Alessandro Della Bona, Stefano Lorenzi, Lelio Luzzi.
Development of the ALFRED reactor full power mode control system.

[3] G. Rimpault, D. Honde, J. M. Rieunier.
ERANOS: manuel des methodes.
Technical Report NT-SPRC-LEPh-93-252, CEA, 1993.

[4] G. Rimpault et al.
SchÃ©ma de calcul de rÃ©fÃ©rence du formulaire ERANOS et orientations pour le schÃ©ma de calcul de projet.
Technical Report NT-SPRC-LEPh-96-220, CEA, 1996.

[5] G. I. Bell, S. Glasstone.
Nuclear reactor theory.
Krieger Publishing Company, 1979.

[6] Antonio Galia.
A Dynamic Homogenization Method for Nuclear Reactor Core Calculations.

[7] Giacomo Grasso et al.
EGPRS Lead-cooled Fast Reactor (LFR) Benchmark.
Benchmark under the guidance of the Expert Group on Physics of Reactor Systems (EGPRS).

[8] Pietro Ravetto.
A revisitation of space asymptotic theory in neutron transport.

[9] Alain HÃ¨bert
Applied Reactor Physics

[10] G. RIMPAULT R. JACQMIN A. BERNARD
Rapport Technique

[11] G. RIMPAULT - D. HONDE - J.M. RIEUNIER
ERANOS : MANUEL DES METHODES Transferts Internes de DonnÃ©es NuclÃ©aires

[12] https://docs.openmc.org/en/stable/
The OpenMC Monte Carlo Code

[13] K. Aoto, P. Dufour, Y. Hongyi, et al.,
âA summary of sodium-cooled fast reactor development,â Progress in Nuclear Energy

[14] M. Frignani, A. Alemberti, and M. Tarantino,

âAlfred: A revised concept to improve pool related thermal-hydraulics,â Nuclear Engineering and Design

[15] G. Grasso, M. Sarotto, F. Lodi, and D. M. Castelluccio,
âAn improved design for the alfred core,â in International Congress on Advances in Nuclear Power Plants (ICAPP 2019)

[16] A. Alemberti, M. Caramello, M. Frignani, et al.,
âAlfred reactor coolant system design,â Nuclear Engineering and Design

[17] G. I. I. Forum, Gif 2023 annual report, 2023

[18] Stephen M. Goldberg and Robert Rosner
Nuclear Reactors:Generation to Generation

[19] U. D. N. E. R. A. Committee and the Generation IV International Forum
A technology roadmap for generation iv nuclear energy systems

[20] G. Grasso, C. Petrovich, D. Mattioli
The core design of alfred, a demonstrator for the european lead-cooled reactors

[21] C. F. Smith and L. Cinotti
Chapter 6 - lead-cooled fast reactors (lfrs),n Handbook of Generation IV Nuclear Reactors (Second Edition)

[22] https://www.oecd-nea.org/jcms/$pl_3$9910/*janis*